UNIVERSITY OF ALBERTA

THERMAL WELL TESTING
FOR
NON-DIPPING AND DIPPING RESERVOIRS

BY

JAMES JIAPING SHENG

A THESIS

SUBMITTED TO THE FACULTY OF GRADUATE STUDIES AND RESEARCH IN

PARTIAL FULFILLMENT OF THE REQUIREMENTS FOR DEGREE OF

MASTER OF SCIENCE

IN

PETROLEUM ENGINEERING

DEPARTMENT OF MINING, METALLURGICAL AND

PETROLEUM ENGINEERING

EDMONTON, ALBERTA

FALL 1992

ISBN 0-315-77269-7

UNIVERSITY OF ALBERTA

RELEASE FORM

NAME OF AUTHOR: James Jiaping Sheng

TITLE OF THESIS: Thermal Well Testing for Non-Dipping and Dipping Reservoirs

DEGREE FOR WHICH THESIS WAS PRESENTED: Master of Science

YEAR THIS DEGREE WAS GRANTED: Fall 1992

(SIGNED) James Sheng

PERMANENT ADDRESS:

SHENGJIA VILLAGE
DAOSHI TOWN, DANYANG
JIANGSU PROVINCE
P. R. CHINA

DATED: Oct. 5, 1992

THE UNIVERSITY OF ALBERTA

FACULTY OF GRADUATE STUDIES AND RESEARCH

The undersigned certify that they have read, and recommend to the Faculty of Graduate Studies and Research for acceptance, a thesis entitled THERMAL WELL TESTING FOR NON-DIPPING AND DIPPING RESERVOIRS submitted by JAMES JIAPING SHENG in partial fulfillment of the requirements for the degree of MASTER OF SCIENCE in PETROLEUM ENGINEERING.

Prof. A. K. Ambastha (Supervisor)

Prof. W. S. Tortike

Prof. D. R. Schmitt

Date: Oct 5, 92

ABSTRACT

Thermal well testing offers an inexpensive method to obtain an estimation of flow capacity and swept volume in thermal recovery. To evaluate the accuracy and applicability of the thermal well testing method in the estimation of flow capacity and swept volume for steam injection in non-dipping and dipping reservoirs, a thermal numerical simulator is used to simulate the pressure falloff testing. Different gridblock models are designed in this study. Results of this study show that the swept volume and skin factor can be reasonably estimated from pressure falloff tests. However, the estimated permeability from falloff tests is 30% to 40% higher than the effective permeability at the volume-weighted average steam saturation behind the zero steam saturation front. The estimated permeability may reflect the effective permeability of a high steam saturation zone around the injection well. The effects of gravity, dip, permeability anisotropy and irregular shapes of swept zones are investigated. These factors do not affect the estimated results significantly. The real gas analysis is also conducted.

Results of 3D models show that the estimation of flow capacity and swept volume depends on the vertical positions where pressure data are measured. This finding should be important to guide thermal well testing interpretation.

The applicability of the *Stanislav et al.* approach is limited by its application conditions in practical well tests. The modified approach is proposed to expand the applicability by removing these conditions.

ACKNOWLEDGEMENTS

The author wishes to express his sincere gratitude and appreciation to Professor A. K. Ambastha for his guidance and support throughout this study. Financial support for this work and my graduate studies was provided by the Alberta Oil Sands Technology and Research Authority (AOSTRA), for which I am very thankful. I also wish to acknowledge the use of the In Situ Combustion and Steam Reservoir Simulator (ISCOM) developed by the Computer Modelling Group of Calgary, Alberta. Finally, I would like to thank my parents, Jifa and Soying, and my grandmother for their understanding and support during my graduate studies abroad.

TABLE OF CONTENTS

page

List of Tables ix

List of Figures x

Nomenclature xv

Chapter 1 Introduction 1

Chapter 2 Review of Literature 3

2.1 Theoretical Fundamentals of Thermal Well Testing 3

2.2 Methods of Analysis 5

2.2.1 Drawdown Analysis and Buildup Analysis 5

2.2.2 Liquid Well Testing Analysis and Gas Well Testing Analysis 7

2.2.3 Multi-dimensional Models to Include Gravity Effects 8

2.3 Estimation of Formation Permeability and Skin Factor 9

2.4 Estimation of Swept Volumes 10

2.4.1 Deviation Time Method 11

2.4.2 Intersection Time Method 12

2.4.3 Type Curve Matching Method 13

2.4.4 Pseudosteady State Method 13

2.5 Application in Non-Dipping and Dipping Reservoirs 16

2.6 Thermal Well Testing Method with Inclusion of Steam-Condensation Effect 16

Chapter 3 Statement of the Problem 18

Chapter 4 Methodology of Steam Injection Falloff Testing 20

4.1 Liquid Well Testing Analysis 20

4.1.1 Formulation 20

4.1.2 Identification of Flow Regions 23

4.1.3 Estimation of the Average Pressure and the Average Temperature 24

4.1.4 Wellbore Radius 25

4.2 Gas Well Testing Analysis 25

4.2.1 Pressure Squared Method 26

4.2.2 Pseudo-pressure Function Method 26

Chapter 5 Simulation Study of Thermal Well Testing in Non-Dipping and Dipping Reservoirs 28

5.1 Simulator 28

5.2 Reservoir and Fluid Model 29

5.2.1 Reservoir and Fluid Properties 29

5.2.2 Reservoir Gridblock Sizes 29

5.2.3 Well Directions for Dipping Reservoirs 37

5.3 Simulation Results and Discussion 37

5.3.1 Determination of the Method to Identify the Swept Zone 40

5.3.2 Validity of the Estimation of k, s and V_s 43

5.3.3 Further Analysis of the Pressure Derivative Curve 53

5.3.4 Gravity Segregation of Steam 54

5.3.5 Real Gas Analysis 57

5.3.6 Effect of Dip 63

5.3.7 Effect of Shapes of Swept Zones 66

5.3.8 Effect of Permeability Anisotropy 68

5.3.9 Results of Ideal Gas Analysis 71

Chapter 6 Discussion About the Stanislav *et al.* Approach 73

6.1 The *Stanislav et al.* Approach 73

6.2 Examples of Application and Discussion 77

6.3 Further Discussion 84

6.4 The Modified *Stanislav et al.* Approach 85

6.4.1 The Modified *Stanislav et al.* Approach 85

6.4.2 Example of Application 87

Chapter 7 Conclusions and Recommendations 91

7.1 Conclusions 91

7.2 Recommendations 92

References 94

Appendix A Derivation of Formula in Real Gas Analysis 100

Appendix B Program for the Calculation of Pseudo-pressure Function 104

Appendix C An Example of Input and Output Data for Appendix B (Run 1) 108

Appendix D Figures for Analysis of the Simulated
Thermal Well Testing Data 110

LIST OF TABLES

		Page
Table 5.1	Reservoir and Fluid Parameters Used in Simulation	30
Table 5.2	Viscosity-Temperature Relationship for Reservoir Fluids	30
Table 5.3	Gridblock Sizes for Test Runs	32
Table 5.4	Gridblock Sizes Used in This Study	36
Table 5.5	Simulated Falloff Test Results and Conditions	41
Table 5.6	Block and Effective Properties for Run 1 (Radial Model)	42
Table 5.7	Effect of the Locations of Pressure Gauge	56
Table 5.8	Comparison of Results from Three Analysis Methods (Run 1)	57
Table 5.9	Effect of Dip	63
Table 5.10	Effect of Permeability Anisotropy	69
Table 6.1	Comparison of Results from Three Well Testing Approaches	90

LIST OF FIGURES

Page

Figure 5.1 Water/Oil Relative Permeability Curve 31

Figure 5.2 Gas/Oil Relative Permeability Curve 31

Figure 5.3 Semilog Pressure Derivative Data for Test Run 1 33

Figure 5.4 Semilog Pressure Derivative Data for Test Run 2 33

Figure 5.5 Semilog Pressure Derivative Data for Test Run 3 34

Figure 5.6 Semilog Pressure Derivative Data for Test Run 4 34

Figure 5.7 3D Schematic Model of a Dipping Reservoir for a Vertical Well 38

Figure 5.8 3D Schematic Model of a Dipping Reservoir for an Inclined Well 39

Figure 5.9 Total Mobility and Steam Saturation Distribution for Run 2 ($\Delta t = 0$) .. 44

Figure 5.10 Total Mobility and Steam Saturation Distribution for Run 2 (Δt = 10 hours) 45

Figure 5.11 Semilog Pressure Derivative Data for Run 1 46

Figure 5.12 Semilog Straight Line for Run 1 46

Figure 5.13 Cartesian Straight Line for Run 1 47

Figure 5.14 Semilog Pressure Derivative Data for Run 2 49

Figure 5.15 Semilog Straight Line for Run 2 50

Figure 5.16 Cartesian Straight Line for Run 2 50

Figure 5.17 Semilog Pressure Squared Derivatives for Run 1 59

Figure 5.18 Semilog Straight Line of p_{ws}^2 vs. Δt for Run 1 59

Figure 5.19 Cartesian Straight Line of p_{ws}^2 vs. Δt for Run 1 60

Figure 5.20 Semilog Pseudo-pressure Derivatives for Run 1 61

Figure 5.21 Semilog Line of ψ_{ws} vs. Δt for Run 1 62

Figure 5.22 Cartesian Line of ψ_{ws} vs. Δt for Run 1 62

Figure 5.23 Shapes of Swept Zones for Run 3 and Runs 6 through 9 65

Figure 5.24 Total Mobility and Steam Saturation Distribution for Run 3 (J = 8) ... 67

Figure 5.25 Effect of Permeability Anisotropy on the Shapes of Swept Zones 70

Figure 6.1 Plot of $\Delta p - \gamma/2\ln(\Delta t)$ vs. $\Delta t^{1/2}$ of *Stanislav et al.*'s Data (1989) 78

Figure 6.2 Plot of $\Delta p - 2\beta\gamma\delta^{1/2}\Delta t^{1/2}$ vs. Δt of *Stanislav et al.*'s Data (1989) ... 79

Figure 6.3 Plot of $\Delta p - \gamma/2\ln(\Delta t)$ vs. $\Delta t^{1/2}$ of Falloff Data from Run 1 80

Figure 6.4 Plot of $\Delta p - 2\beta\gamma\delta^{1/2}\Delta t^{1/2}$ vs. Δt of Falloff Data from Run 1 81

Figure 6.5 Plot of $\Delta p - \gamma/2\ln(\Delta t)$ vs. $\Delta t^{1/2}$ of Falloff Data from Run 2 82

Figure 6.6 Plot of $\Delta p - 2\beta\gamma\delta^{1/2}\Delta t^{1/2}$ vs. Δt of Falloff Data from Run 2 83

Figure 6.7 Semilog Pressure Function Derivatives for Run 2 89

Figure 6.8 Semilog Graph of $\Delta p - C_G\Delta t^{1/2}$ vs. Δt for Run 2 89

Figure 6.9 Cartesian Graph of $\Delta p - C_G\Delta t^{1/2}$ vs. Δt for Run 2 90

Figure D.1 Pressure Falloff Data for Run 1 111

Figure D.2 Pressure Falloff Data for Run 2 111

Figure D.3 Pressure Falloff Data for Run 3 (K=1) 112

Figure D.4 Semilog Pressure Derivatives for Run 3 (K=1) 112

Figure D.5 Semilog Straight Line for Run 3 (K=1) 113

Figure D.6 Cartesian Straight Line for Run 3 (K=1) 113

Figure D.7 Pressure Falloff Data for Run 3 (K=2) 114

Figure D.8 Semilog Pressure Derivatives for Run 3 (K=2) 114

Figure D.9 Semilog Straight Line for Run 3 (K=2) 115

Figure D.10 Cartesian Straight Line for Run 3 (K=2) 115

Figure D.11 Pressure Falloff Data for Run 3 (K=3) 116

Figure D.12 Semilog Pressure Derivatives for Run 3 (K=3) 116

Figure D.13 Semilog Straight Line for Run 3 (K=3) 117

Figure D.14 Cartesian Straight Line for Run 3 (K=3) 117

Figure D.15 Pressure Falloff Data for Run 4 118

Figure D.16 Semilog Pressure Derivative Data for Run 4 118
Figure D.17 Semilog Straight Line for Run 4 119
Figure D.18 Cartesian Straight Line for Run 4 119
Figure D.19 Pressure Falloff Data for Run 5 (K=1) 120
Figure D.20 Semilog Pressure Derivatives for Run 5 (K=1) 120
Figure D.21 Semilog Straight Line for Run 5 (K=1) 121
Figure D.22 Cartesian Straight Line for Run 5 (K=1) 121
Figure D.23 Pressure Falloff Data for Run 5 (K=2) 122
Figure D.24 Semilog Pressure Derivatives for Run 5 (K=2) 122
Figure D.25 Semilog Straight Line for Run 5 (K=2) 123
Figure D.26 Cartesian Straight Line for Run 5 (K=2) 123
Figure D.27 Pressure Falloff Data for Run 5 (K=3) 124
Figure D.28 Semilog Pressure Derivatives for Run 5 (K=3) 124
Figure D.29 Semilog Straight Line for Run 5 (K=3) 125
Figure D.30 Cartesian Straight Line for Run 5 (K=3) 125
Figure D.31 Pressure Falloff Data for Run 5 (K=4) 126
Figure D.32 Semilog Pressure Derivatives for Run 5 (K=4) 126
Figure D.33 Semilog Straight Line for Run 5 (K=4) 127
Figure D.34 Cartesian Straight Line for Run 5 (K=4) 127
Figure D.35 Pressure Falloff Data for Run 6 128
Figure D.36 Semilog Pressure Derivative Data for Run 6 128
Figure D.37 Semilog Straight Line for Run 6 129
Figure D.38 Cartesian Straight Line for Run 6 129
Figure D.39 Pressure Falloff Data for Run 7 130
Figure D.40 Semilog Pressure Derivative Data for Run 7 130
Figure D.41 Semilog Straight Line for Run 7 131
Figure D.42 Cartesian Straight Line for Run 7 131

Figure D.43 Pressure Falloff Data for Run 8 132

Figure D.44 Semilog Pressure Derivative Data for Run 8 132

Figure D.45 Semilog Straight Line for Run 8 133

Figure D.46 Cartesian Straight Line for Run 8 133

Figure D.47 Pressure Falloff Data for Run 9 134

Figure D.48 Semilog Pressure Derivative Data for Run 9 134

Figure D.49 Semilog Straight Line for Run 9 135

Figure D.50 Cartesian Straight Line for Run 9 135

Figure D.51 Pressure Falloff Data for Run 10 136

Figure D.52 Semilog Pressure Derivative Data for Run 10 136

Figure D.53 Semilog Straight Line for Run 10 137

Figure D.54 Cartesian Straight Line for Run 10 137

Figure D.55 Pressure Falloff Data for Run 11 138

Figure D.56 Semilog Pressure Derivative Data for Run 11 138

Figure D.57 Semilog Straight Line for Run 11 139

Figure D.58 Cartesian Straight Line for Run 11 139

Figure D.59 Pressure Falloff Data for Run 1* 140

Figure D.60 Semilog Pressure Derivative Data for Run 1* 140

Figure D.61 Semilog Straight Line for Run 1* 141

Figure D.62 Cartesian Straight Line for Run 1* 141

Figure D.63 Pressure Falloff Data for Run 2* 142

Figure D.64 Semilog Pressure Derivative Data for Run 2* 142

Figure D.65 Semilog Straight Line for Run 2* 143

Figure D.66 Cartesian Straight Line for Run 2* 143

Figure D.67 Pressure Falloff Data for Run 3* 144

Figure D.68 Semilog Pressure Derivative Data for Run 3* 144

Figure D.69 Semilog Straight Line for Run 3* 145

Figure D.70 Cartesian Straight Line for Run 3* 145
Figure D.71 Pressure Falloff Data for Run 6* 146
Figure D.72 Semilog Pressure Derivative Data for Run 6* 146
Figure D.73 Semilog Straight Line for Run 6* 147
Figure D.74 Cartesian Straight Line for Run 6* 147
Figure D.75 Pressure Falloff Data for Run 7* 148
Figure D.76 Semilog Pressure Derivative Data for Run 7* 148
Figure D.77 Semilog Straight Line for Run 7* 149
Figure D.78 Cartesian Straight Line for Run 7* 149
Figure D.79 Pressure Falloff Data for Run 8* 150
Figure D.80 Semilog Pressure Derivative Data for Run 8* 151
Figure D.81 Semilog Straight Line for Run 8* 151
Figure D.82 Cartesian Straight Line for Run 8* 151
Figure D.83 Pressure Falloff Data for Run 9* 152
Figure D.84 Semilog Pressure Derivative Data for Run 9* 152
Figure D.85 Semilog Straight Line for Run 9* 153
Figure D.86 Cartesian Straight Line for Run 9* 153

NOMENCLATURE

A = formation area, ft^2

B = fluid formation volume factor, RB/STB or res ft^3/SCF

C = heat capacity, BTU/lb·°F

C_G = steam condensation constant defined by Eq. 6.22, psi/$hr^{1/2}$

c = isothermal coefficient of compressibility at temperature T, psi^{-1}

f_s = steam quality, fraction

F_ρ = density ratio of water to steam, dimensionless

G = rate of steam condensation defined by Eq. 6.2, ft^3/(hr·ft^3)

h = formation thickness (in the Z direction), ft

I = in I direction

J = in J direction

K = in K direction, or unit of temperature

k = permeability, md

k_e = effective permeability (to steam), md

k_{ec} = calculated (estimated) effective permeability (to steam), md

k_h = thermal conductivity, BTU/(ft·D·°F)

k_{rg} = gas relative permeability, fraction or %

k_{rw} = water relative permeability, fraction or %

k_{row} = oil relative permeability in water/oil system, fraction

k_{rog} = oil relative permeability in gas/oil system, fraction

Lv = latent heat of vaporization, BTU/lb

m = slope of $\Delta p - (\gamma/2)\ln(\Delta t)$ vs. $\Delta t^{1/2}$ defined by Eq. 6.15, psi/$hr^{1/2}$

m' = slope of $\Delta p - C_G(\Delta t)^{1/2}$ vs. $\log(\Delta t)$ defined by Eq. 6.24, psi/cycle

m^* = Cartesian slope of $\Delta p - C_G \Delta t^{1/2}$ vs. Δt defined by Eq. 6.18, psi/hr

M = molar mass, lb/(lb mole), 18.02 for water

m_s = semi-log slope of pressure vs. shut-in time, psi/cycle

m_s' = semi-log slope of pressure squared vs. shut-in time, psia^2/cycle

m_s'' = semi-log slope of pseudopressure vs. shut-in time, psia^2/(cp·cycle)

m_c = Cartesian slope of pressure vs. shut-in time, psi/hr

m_c' = Cartesian slope of pressure squared vs. shut-in time, psia^2/hr

m_c'' = Cartesian slope of pseudopressure vs. shut-in time, psia^2/(cp·hr)

n = number of moles

p = pressure, psia

$\bar{p}$ = average pressure within the swept zone, psia

p_{1hr} = pressure at the shut-in time of 1 hour taken from the semilog straight line, psia

$\Delta p^{(1)}$ = pressure function difference at the shut-in time of 1 hour taken from the straight lines, psi

p_{ws} = wellbore gridblock pressure after shut-in, psia

p_{wfs} = wellbore gridblock pressure at the instant of shut-in, psia

q = flow rate, STB/D

r = radial distance from well, ft

R = universal gas constant, 10.732 psi·ft^3/(lb mole·°R), or unit of temperature

s = wellbore skin factor, dimensionless

S = saturation, fraction or %

$\bar{S}$ = average saturation within the swept zone, fraction or %

t = injection or production time, hours (hr)

Δt = shut-in time, hours (hr)

T = temperature, °R

$\bar{T}$ = average temperature in the swept zone, °F

V = volume, ft^3

V_s = simulation swept bulk volume, ft^3

V_{sc} = calculated swept bulk volume from well testing, ft^3

W = mass, lb

x_f = fracture half-length, ft

z = gas (steam) compressibility factor, fraction

Greek symbols

α = thermal diffusivity of surroundings, ft^2/day

β = steam condensation coefficient defined by Eq. 6.12, dimensionless

β_p = isobaric coefficient of expansion at pressure p, $^oR^{-1}$

δ = defined by Eq. 6.14, hr^{-1}

ϕ = porosity, fraction

γ = defined by Eq. 6.13, psi

ϑ = specific volume, ft^3/lb

λ = mobility, md/cp

$\bar{\lambda}$ = effective mobility, md/cp

μ = viscosity, cp

ρ = density, lb/ft^3

ψ = pseudopressure function $\int_{p_o}^{p} \frac{2p}{\mu z} dp$, $psia^2$/cp

Subscripts

c = Cartesian

D = dimensionless

f = formation

g = gas (steam)

i = initial

L = liquid

o = oil

s = steam

sc = standard conditions

t = total

w = water or wellbore

wfs = at the wellbore and at the instant of shut-in

ws = at the wellbore after shut-in

1hr = at the shut-in time of 1 hour, taken from the semilog straight line

2ϕ = two-phase

CHAPTER 1

INTRODUCTION

Thermal recovery by steamflooding is an important method for producing heavy oil around the world. The determination of the swept volume in a steam displacement process provides an early means to evaluate the project's progress. By determining the volume occupied by steam, and knowing the cumulative volume of steam injected, the heat losses from the injection interval and the ensuing heat efficiencies can be estimated. These parameters dictate the performance efficiency of the displacement project.

In field operations, swept volumes in thermal oil recovery have usually been determined by temperature observation wells and/or coring, usually at considerable expense and subject to great uncertainty due to irregular swept regional shapes. Thermal well testing offers an inexpensive method to obtain an estimate of steam swept volume. It also provides an estimation of flow capacity and skin factor.

The thermal well testing method in steamflooding projects is pressure falloff testing, based on the *Eggenschwiler et al.* theory (1980). This theory applies to a composite reservoir model with two regions having highly contrasting fluid mobilities. The assumptions made in this theory cannot be strictly satisfied in a field steam injection falloff test. This study proposes to evaluate the accuracy and the applicability of the thermal well testing method under real steam injection conditions for non-dipping and dipping reservoirs. The numerical simulator ISCOM 4.0 (*CMG*, 1987) is used to simulate steam injection falloff tests.

The *Eggenschwiler et al.* analysis does not consider the steam-condensation effect induced by heat losses to the surrounding rocks. *Stanislav et al.* (1989) proposed a method of falloff data analysis including the steam-condensation effect. This study is intended to address the applicability of their method in steamflood projects.

Chapter 2 presents the current status of research in thermal well testing. Chapter 3 presents the statement of the problem. Chapter 4 presents the methodology of steam injection falloff testing used in this study. Chapter 5 presents a detailed simulation study of thermal well testing in non-dipping and dipping reservoirs. Investigation is conducted to evaluate the accuracy and applicability of thermal well testing, to compare the accuracy of pressure analysis and real gas analyses, and to study the effects of gravity, irregular shapes of swept zones, dip, and anisotropy in permeability. Chapter 6 presents the discussion about the *Stanislav et al.* approach. The application conditions are presented. A modified approach is also proposed. Finally, Chapter 7 presents conclusions drawn from this study and recommendations for further investigation.

CHAPTER 2

LITERATURE REVIEW

The determination of the swept volume in a thermal oil recovery process is of primary concern. Estimation of the swept volume at intermediate stages of the operation, either in-situ combustion or steam injection, makes the early economic evaluation possible. Thermal well testing offers an inexpensive method to estimate the formation flow capacity and the swept volume. In this literature review, the current status of research in steam injection falloff testing, is presented.

2.1 Theoretical Fundamentals of Thermal Well Testing

Estimation of steam zone properties and swept volume from well test data is based on the theory developed by *Eggenschwiler et al.* (1980). This theory applies to a composite reservoir model with two regions having highly contrasting fluid mobilities. The inner region, adjacent to the wellbore, represents the steam swept zone with an extremely high fluid mobility. The outer region represents the unswept zone, the portion of the reservoir unaffected by steam injection and containing lower mobility fluid. Because of the high contrast in fluid mobilities, the boundary between the inner and outer regions acts as a "no-flow boundary" for a short period of time. Consequently, the computed pressure response exhibits pseudosteady state behavior (i.e., dp/dt = constant). *Eggenschwiler et al*'s numerical results indicate a short duration wellbore storage effect, followed by a semilog straight line whose slope is related to the permeability-thickness of the swept volume. The semilog straight line is then followed by a pseudosteady Cartesian straight line characteristic of the swept volume. Finally, a second semilog straight line appears, characteristic of the permeability-thickness of the unswept region. Their results also indicate that the initial wellbore storage effect dies in a few minutes, and the semilog straight line characteristic of the swept volume occurs almost immediately on shut-in. Further, the pseudosteady period occurs in durations from a fraction of an hour to a few hours.

There are several assumptions implicit in the *Eggenschwiler et al.* model (1980):

(1) The formation is horizontal, of uniform thickness, and homogeneous in each region;

(2) The front is a cylindrical front of infinitesimal thickness in the flow direction and is considered stationary throughout the testing period;

(3) Flow is radial, and gravity and capillarity effects are negligible;

(4) Fluids are of constant viscosity, compressibility and relative permeability within the same regions;

(5) There is no fluid phase shift;

(6) The fluid is treated as a liquid of slight compressibility, rather than as an ideal or real gas.

Eggenschwiler et al. (1980) pointed out that the calculation using the concept of pseudosteady state was a material balance calculation. This means that the pore volume of the swept region determined from the Cartesian graph of pressure versus time is actually independent of the geometry of the swept zone. Of course, the result is also independent of detailed knowledge of the variation of the thickness of the swept zone. They further concluded that the pressure depletion of the high permeability swept zone would happen much faster than fluid could flow from the low permeability unswept region ahead of the front. This would mean that the actual geometrical detail of the shape of the swept region would not be an important parameter for the pressure/time data during the pseudosteady state.

During steam injection process, phase changes take place between steam and water when pressure changes. With the pressure change, the specific volume of each phase changes, but this change is small in comparison with the volume changes caused by phase change (*Grant* and *Sorey*, 1979). Thus, the compressibility of each phase can be ignored. Therefore, the compressibility as a result of the phase change (called two-phase compressibility, $c_{2\phi}$) is almost equal to the total compressibility. *Grant* and *Sorey* (1979) derived the two-phase compressibility of a water-steam mixture.

Based on the *Eggenschwiler et al.* theory (1980) and the concept of two-phase compressibility (*Grant* and *Sorey*, 1979), *Walsh et al.* (1981) presented a detailed procedure for quantitatively interpreting pressure falloff tests during steamflood projects.

2.2 Methods of Analysis

Like non-thermal well tests, the steam falloff test data could be analyzed in drawdown analysis or buildup analysis. Since steam may be treated as liquid or gas, the falloff data could be analyzed by liquid well testing method or gas well testing method. Although the flow is multi-dimensional during steam injection and falloff tests, one-dimensional radial models were used in some simulation studies.

2.2.1 Drawdown Analysis and Buildup Analysis

When the mobility ratio between the injected and in-situ fluids is about unity, injection well testing for liquid-filled systems is analogous to production well testing. Injection is similar to production (but the rate, q, used in equations is negative for injection while it is positive for production), so an injectivity test is effectively the same as a drawdown test. Shutting in an injection well results in a pressure falloff that is analogous to a pressure buildup (*Earlougher*, 1977).

When the unit-mobility-ratio assumption is not satisfied, the similarity between production well testing and injection well testing is not so complete. During a steam falloff test, the front is moving. Theoretically, the buildup method, Horner method (Horner, 1951 or 1967), should not be applied to the moving-front problems because the linear superposition principle does not apply. However, *Kazemi et al.* (1972) developed a mathematical model for pressure falloff tests to investigate the practicability of the falloff testing method. The solution of the mathematical model was obtained by an implicit finite-difference method. They found that the nonlinearity of the moving-front problems was mild enough that the linear superposition was a very good engineering approximation for such problems. Thus, the Horner method can be generally applied, and, in fact, they obtained much better results by using the Horner method than the MDH method (*Miller, Dyes* and *Hutchinson,* 1951 or 1967). *Ramey* and *Cobb* (1971) pointed out the (MDH) method can be used, but only if $\Delta t << t$, which should be satisfied in most situations.

Bixel and *van Poollen* (1967) generated buildup curves from the numerical solution of finite difference equations. They found that the early portions of all curves gave the correct slope for transmissibility in the inner region. *Hazebroek et al.* (1958) discussed falloff tests for water injection wells before fillup. They assumed a significant gas saturation ahead of the oil bank and that the pressure at the leading edge of the oil bank was constant and dominated by the pressure in the gas phase. They concluded that permeability for the zone near the well might be estimated equally well by their method or by the MDH and Horner techniques. *Ziegler* (1990) used the equivalent time developed by *Agarwal* (1980) in the analysis. He found that equivalent time closely approximated the elapsed time since shut-in. *Ambastha* and *Kumar* (1989) also used the equivalent time in their analysis.

Other investigators used the drawdown test method (*Messner* and *Williams*, 1982a and b, *Onyekonwu et al.*, 1984, and *Fassihi*, 1988).

2.2.2 Liquid Well Testing Analysis and Gas Well Testing Analysis

During the steam falloff tests, the fluid of interest, steam, is a condensible gas. If gas characteristics are considered, gas well testing analysis is applied. If average gas properties are used, liquid well testing analysis could be applied.

Messner and *Williams* (1982a) treated injected steam as a liquid. In their further investigation (1982b), they treated injected steam as a gas, used the slopes of the straight lines obtained from a semilog graph of the pressure squared vs. shut-in time and a semilog graph of the pseudo-pressure vs. shut-in time to estimate permeability, assuming that the injection period was of much greater duration than the shut-in period. They concluded from the analysis of their results that an analysis incorporating the real gas pseudo-pressure was unnecessary. The method using pressure vs. shut-in time sufficed for most practical situations.

Onyekonwu et al. (1984) presented the results calculated from the liquid well testing formula for in-situ combustion processes. They pointed out that a similar relationship was obtained from the plot of the square of pressure vs. shut-in time.

Fassihi (1988) also presented the results calculated from the liquid well testing formula. But he pointed out that the effect of non-ideal gas flow on falloff tests was investigated by calculating the real gas pseudo-pressure. The calculated swept volumes and permeabilities were close to the ones calculated assuming ideal gas flow. Thus, the real gas flow did not have any effect on the analysis of his simulated falloff tests. This was because of the narrow pressure drop observed in his tests.

Ziegler (1990) used a pseudo-pressure function to analyze the pressure falloff data. He found that parameter estimates derived from the pressure analysis were generally within 6% of the pseudo-pressure results. In his simulation study, the estimated permeability and swept volume from pressure analysis were closer to the simulator results than those from pseudo-pressure analysis.

To use the liquid well testing formula, some average fluid and rock properties must be determined from average pressure and temperature. There is no unique way of estimating the average reservoir pressure in the swept zone on pressure-transient tests.
Walsh et al. (1981) assumed the early-time flattening of the semilog graph of pressure vs. time to represent the average reservoir pressure in the swept zone. The average temperature was estimated from the average steam saturation pressure. In *Onyekonwu et al.*'s study (1984), the effective mobility was determined by applying the flow resistance concepts. The effective pressure and the effective compressibility were the volume-weighted averages of gridblock pressures and compressibilities, respectively, in the swept zone. *Fassihi* (1988) used the (arithmetic) average of the two pressures at the beginning and end of the semilog straight line for the calculation of fluid properties. In *Ziegler* 's study (1990), pressure-dependent steam properties (T, μ and c_t) were estimated at the initial pressure extrapolated from the Cartesian straight line.

2.2.3 Multi-dimensional Models to Include Gravity Effects

From a one-dimensional, 20x1x1 cell radial model, *Messner* and *Williams* (1982a) found that the calculated swept volume was in close agreement with the simulated swept volume, with a difference of about 10%. In an attempt to learn about the effects of steam override on the pressure transient response, *Messner* and *Williams* (1982b) converted a one-dimensional radial model to a two-dimensional 20x1x5 radial configuration, with each grid cell in the vertical direction having a thickness of 10 ft. They found that the estimated swept volume from the two-dimensional model was smaller than that estimated from the one-dimensional radial model. It seemed that the swept volume would be underestimated, if gravity was included. They pointed out that it was questionable whether the swept volume underestimation was indicative of a real-life phenomenon or a "quirk" exclusively inherent in the simulation method.

Onyekonwu et al. (1984) pointed out that although a one-dimensional radial model was used in their study, the concept should apply in multi-dimensional cases, where gravity override is common.

Fassihi (1988) used the two-dimensional radial model to include gravity effects in his study, with the conclusions that the estimated kh was the effective gas permeability/thickness behind the front, and the estimated swept volume in steam falloff tests was close to the simulated volume.

Issaka and *Ambastha* (1992) found the swept volume was overestimated for horizontal wells, with gravity considered in their 3D model.

2.3 Estimation of Formation Permeability and Skin Factor

The semilog straight lines of the early time well testing data are used to estimate k or kh of the inner region in composite reservoirs (except the *Hazebroek et al.* method, 1958).

Messner and *Williams* (1982a) found that the estimated steam permeability of the inner region was an order of magnitude less than the input absolute permeability, both from the field falloff data and the simulation falloff data. They ascribed this result to the small relative permeability of the steam vapor. They also obtained positive skin values for the well tests.

Onyekonwu et al. (1984) found that the semilog slopes calculated from effective parameters compared favorably with those from the plot of the simulated falloff data during in-situ combustion processes.

Fassihi (1988) and *Ziegler* (1990) pointed out that the estimated permeabilities were in agreement with the effective permeabilities at the average steam saturations. But they did not show how to calculate average steam saturation.

Ambastha and *Kumar* (1989) carried out the pressure falloff analyses for three cyclic steam injection wells in a low-permeability (< 1 md), heavy oil, reservoir with steam-induced vertical fractures. They reported a good estimate of the product kx_f^2 and approximate estimates of k and x_f. They assumed $S_g = 1$ in the swept region, which, they noted, was not true.

Issaka and *Ambastha* (1992) found that steam chamber mobility and skin factor could be reasonably estimated from the well testing data for horizontal wells. In their study, the estimated permeability from well testing was in good agreement with the effective permeability at the average steam saturation. The average steam saturation was volume-weighted saturation behind the zero-saturation front.

2.4 Estimation of Swept Volumes

Since the determination of the swept volume during thermal recovery processes is important, different methods to estimate the swept (or burned) volume from pressure falloff data have been investigated. These include the deviation time, intersection time, type curve matching, and pseudosteady state methods.

2.4.1 Deviation Time Method

When pressure transient data from a falloff test are graphed versus time, the data may indicate an initial semilog straight line, characteristic of fluid mobility in the inner (swept) zone. A deviation from the straight line occurs when the effects of the interface (or front) separating the inner and outer zone are felt. The time at the end of the semilog straight line is used to calculate the front radius, based on some theoretical dimensionless deviation times. *van Poollen* (1964) discussed the concepts of radius of drainage and stabilization time. He (1965) used a deviation time to locate the flood front in an in-situ combustion project. *Kazemi* (1966) also used the deviation time method to calculate the distance to the burning front from pressure falloff data of an in-situ combustion project.

Bixel and *van Poollen* (1967) solved the finite-difference equations derived from the material balance using a digital computer. The ranges of variables studied included dimensionless time from 0.001 to 100 and storage capacity ratio from 0.001 to 1,000. They found the dimensionless deviation time would be 0.25.

Merrill et al. (1974) derived a deviation time by generating a wide range of pressure falloff curves for two-zone, radial, composite reservoirs using a numerical simulator. They found the dimensionless deviation time to lie between 0.13 and 1.39 by running many cases for a two-zone reservoir. The arithmetic average dimensionless deviation time was 0.389. They stated that the range of error with the arithmetic average value of 0.389 would be 0.58 to 1.89. For a three-zone system, the average time of derivation from the first straight-line segment of a plot of dimensionless pressure vs. the logarithm of dimensionless time was 0.485. The error of this estimate would lie with the range of 0.59 to 2.04.

Tang (1982) approximated the dimensionless deviation time to be 0.4 by observing the pressure response from *Eggenschwiler et al.*'s analytical solution (1980). *Ambastha* and *Ramey* (1989) observed the dimensionless deviation time to be 0.18 from their pressure derivative response. Thus, more accurate deviation time is needed to obtain meaningful results from the deviation time method. Furthermore, the deviation method assumes the flood front to be cylindrical. This is often not the case in thermal recovery processes because of gravity effects. Another drawback of the deviation time method is that it is possible for wellbore storage effects to mask the initial semilog straight line, making the method inapplicable.

2.4.2 Intersection Time Method

When pressure falloff data deviate from the initial semilog straight line, it may be possible to observe a second semilog straight line after some transition period, and if the falloff test is run long enough. This second semilog straight line is characteristic of fluid mobility in the outer zone. The time at which the two semilog straight lines intersect can be used to calculate the front radius, based on a theoretical dimensionless intersection time. This method, proposed by *Merrill et al.* (1974), is among the earlier methods used to calculate the front radius. *Merrill et al.* (1974) showed the dimensionless intersection time of the two straight lines is a constant, for mobility ratios close to and less than unity. However, for mobility ratios much greater than unity, the dimensionless intersection time is a function of both the mobility ratio and the specific storage ratio. They presented a correlation of the dimensionless intersection time as a function of the slope ratio, with specific storage ratio as a parameter. The main drawback of the intersection time method in thermal projects is that in most cases, either the falloff test will not be run long enough to see the second semilog straight line, or outer boundary effects will mask the second semilog straight line, as pointed out by *Ambastha* and *Ramey* (1989). In steam injection projects, even if the falloff tests are run long enough, it may be very difficult to see the second straight line because of a long transition between the two semilog straight lines caused by mobility and storativity contrasts.

2.4.3 Type Curve Matching Method

The type curve matching method involves fitting the entire falloff data to a set of theoretical dimensionless type curves computed from a mathematical model. Typically, the type curves are dimensionless functions of pressure or pressure derivative versus time, with mobility and storativity ratios as parameters. *Bixel* and *van Poollen* (1967) proposed a type curve matching method to calculate the distance to the radial discontinuity in a composite reservoir. *Barua* and *Horne* (1987) used automated type curve matching to analyze thermal recovery well tests. *Ambastha* and *Ramey* (1989) presented a type curve matching method for thermal recovery well tests based on the relationship between the dimensionless semilog pressure derivative and the dimensionless time, with mobility and storativity ratios as parameters.

Although some analytical type curve matching methods were published, few applications were found in the literature, probably because of the non-uniqueness problem. *Messner* and *Williams* (1982b) used the type curve matching to analyze the interference testing data for permeability and compressibility estimations. *Ziegler* (1990) used the type curve matching method to estimate permeability and skin factor. Both of them used the standard type curve matching techniques, i.e., the conventional type curves (*Earlougher*, 1977).

2.4.4 Pseudosteady State Method

The pseudosteady state method is derived from the mobility and storativity contrasts between the inner and outer zones of a composite reservoir. The method was proposed by *Eggenschwiler et al.* (1980). They demonstrated the applicability of the pseudosteady state method by analyzing the previously published falloff data from *van Poollen* (1965) and *Kazemi* (1966). The results were in close agreement.

Several investigators have attempted to confirm the existence of the pseudosteady state period. *Walsh et al.* (1980) proposed guidelines for evaluating pressure falloff tests for both steam injection and in-situ combustion wells to determine the swept volumes as well as the heat distribution within the reservoir. Using *Walsh et al.*'s analysis procedure, *Messner* and *Williams* (1982a) analyzed falloff test data from several steamflood projects. Temperature observation wells were included in most of the steamflood projects to aid in the verification of the analysis procedure. In addition, *Messner* and *Williams* (1982a) used a fully implicit thermal simulator to generate falloff data for a comparative analysis. They concluded that in both the field and the simulated cases, the estimated swept volumes appeared reasonable. There was a difference of about 10% between the estimated and the simulated swept volumes from their one-dimensional radial model results. In their further investigation, *Messner* and *Williams* (1982b) treated steam as a gas and used several blocks in the vertical direction to investigate the effect of gravity. Similar results were obtained.

Onyekonwu et al. (1984) simulated pressure falloff tests of in-situ combustion processes in a one-dimensional, radial reservoir. The calculated volumes from falloff test data were in good agreement with the simulated swept volumes. They, however, found that the swept volume included both the burned volume and the high gas saturation zone ahead of the combustion front.

Fassihi (1988) used a numerical simulator to simulate falloff testing of steamflood and in-situ combustion processes in both radial and areal reservoir models. He investigated the effects of such parameters as wellbore grid sizes, non-uniform permeability, layering and oil vaporization, on the swept volume. For steamfloods in relatively homogeneous reservoirs, he compared the calculated swept volumes using the pseudosteady state method with the simulated volumes. The differences between calculated and simulated swept volumes were up to 33%. For very heterogeneous reservoirs, there was a very long transition period that masked the pseudosteady state data. This made it impossible to estimate the swept volume. He also pointed out that the effect of irregular shapes of the swept zones in these tests was not expected to have a significant effect on the simulated swept volume.

Ambastha and *Kumar* (1989) conducted a study to calculate swept volume from field pressure falloff data of steam injection wells in a low-permeability reservoir with steam-induced vertical fractures. They reported that the estimated swept volumes using the pseudosteady state method were unrealistically large. They suggested that the swept volume overestimation may have been caused by short injection time effects on the falloff responses for rectangular swept region.

Ziegler (1990) analyzed the pressure falloff and step-rate injectivity test data during a light-oil steamflood at Buena Vista Hills field, CA. He found that data obtained from tests allowed determination of steam-zone properties and swept volume. Information obtained from an offset temperature observation well and from a heat balance corroborated his pressure analysis results. *Ziegler* (1990) also used a single-layer, radial grid simulation model to evaluate the applicability of the pressure falloff method. In his study, he used pressures and pseudo-pressures vs. shut-in time relationships. The calculated volumes from falloff test data were in good agreement with the simulation volumes. He concluded that falloff testing of steam injection wells was an effective method for evaluating steamflood projects.

Issaka and *Ambastha* (1992) used a 3D model to simulate steam injection falloff testing through a horizontal well. They investigated the effects of wellbore gridblock sizes, injection time, injection rate and isotropy on swept volume estimation. They found that the swept volume might be overestimated by 5% to 60% for horizontal wells. *Issaka* (1991) also pointed out that the irregularities in the shape of the swept volume, caused by increased injection time, affect the occurrence and slope (and consequently, calculated swept volume) of the pseudosteady straight line.

2.5 Application in Non-dipping and Dipping Reservoirs

From the preceding literature review, it appears that the application of the thermal well testing method to determine flow capacity and swept volume in thermal recovery processes, thus far, has only been concentrated to non-dipping reservoirs, and reasonable success has been achieved, especially when gravity effect is not considered. However, some inconsistent results and different viewpoints were presented from the preceding investigations.

There have been a number of studies dealing with steam drive in dipping reservoirs (*Rehkopf*, 1976, *Stokes et al.*, 1978, *Moughamian et al.*, 1982, *Abad*, 1983, *Abad* and *Hensley*, 1984, *Atkinson et al.*, 1989, and *Hong*, 1988, 1990 and 1991). All studies address recovery mechanism, and influence of various reservoir and operating parameters on steam drive performance for dipping reservoirs. However, to the best of our knowledge, the literature does not contain any reference to the application of thermal well testing method to dipping reservoirs.

2.6 Thermal Well Testing Method with Inclusion of Steam Condensation Effect

Recently, *Stanislav et al.* (1989) have investigated the effect of heat losses on the estimation of swept volume based on the pseudosteady state concept. They modified *Eggenschwiler et al.*'s solution (1980) to the composite reservoir model by including a term which accounts for the heat loss from the steam chamber. They carried out a sensitivity study of the solution to the heat loss term. They concluded that under certain conditions, heat loss could have a significant effect on the pressure falloff behavior and dominate the pseudosteady state period. Consequently, they proposed a new analytical procedure for falloff data interpretation, when heat loss effect is significant. To the best of our knowledge, the literature does not contain any papers or comments about the applicability of the new approach.

CHAPTER 3

STATEMENT OF THE PROBLEM

The literature review shows the application of thermal well testing method based on the *Eggenschwiler et al.* theory to non-dipping reservoirs, horizontal wells, and vertically fractured wells. It was expected that the accuracy and applicability of the pseudosteady state method in the estimation of swept volume in all cases should be similar. However, the literature review shows that the preceding investigators presented inconsistent, even opposing results. This stimulated the further investigation of some fundamental concepts and application of thermal well testing in non-dipping reservoirs. Also, it was expected that further investigation of the application of thermal well testing in non-dipping reservoirs would help to understand the application of thermal well testing in dipping reservoirs.

Gravity segregation is one of the prime factors in steamflooding (*Farouq Ali* and *Meldau*, 1990). The effect of gravity segregation on the swept volume is one of interests. For dipping reservoirs, different dip angles will result in different effects of *steam cycling*. Steam cycling is used by *Hong* (1988) to represent the phenomenon of injected steam rising to the top of a reservoir where it condenses because of cooling, and the condensed water falls toward the bottom as a result of gravity. The effect of dip on the estimation of flow capacity and swept volume needs to be investigated for those reservoirs.

Stanislav et al. (1989) presented a mathematical model that describes the effect of heat losses on pressure behavior in falloff testing of steam injection wells. Based on this model, they presented a general solution in the form of type curves (with the heat-loss factor β as a parameter), along with the analytical solutions for the asymptotic cases (β =

0). A new method of falloff data analysis was also proposed. However, no reference has appeared to discuss or apply this new well testing approach. Thus, the main objectives of this study are:

1. to show whether the estimated volume from well testing includes hot water zone or not,
2. to investigate what the flow capacity estimated from well testing represents,
3. to evaluate the accuracy and applicability of the pseudosteady state method in the estimation of swept volumes for non-dipping and dipping reservoirs under steam injection,
4. to compare the accuracy of pressure, pressure squared and pseudo-pressure analyses,
5. to investigate the effects of gravity segregation of steam and irregular shapes of swept zones,
6. to investigate the effect of dip on the swept volume estimation for dipping reservoirs, and
7. to address the applicability of the *Stanislav et al.* well testing approach (1989).

CHAPTER 4

METHODOLOGY OF STEAM INJECTION FALLOFF TESTING

During practical steam injection falloff tests, the shut-in time is much less than the injection time. Thus, the MDH method of analyzing buildup (or falloff) data can be used (*Ramey* and *Cobb*, 1971). Throughout our study, the MDH method is used. In this chapter, the liquid testing analysis and the gas well testing analysis are presented. The methods to evaluate average pressure and temperature are also discussed.

4.1 Liquid Well Testing Analysis

When average steam properties are evaluated, liquid well testing analysis (or pressure analysis) could be applied to steam falloff testing. Liquid well testing analysis is the popular thermal well testing method applied in practice.

4.1.1 Formulation

Based on the theory developed by *Eggenschwiler et al.* (1980), during the early-time period of well tests, and after the end of short-time wellbore storage effect, the infinite-acting radial flow occurs. The plot of pressure vs. shut-in time will yield a semilog straight line related to the flow capacity of the swept region. Using the slope of this semilog straight line, the steam effective permeability and skin factor may be calculated from:

$$k_{ec} = \frac{162.6(q_s)_{sc}B_s\mu_s}{m_s h} \quad , \tag{4.1}$$

$$s = 1.1513\left((\frac{p_{wfs}-p_{1hr}}{m_s}) - \log(\frac{k_{ec}}{\phi \mu_s c_t r_w^2}) + 3.23 \right) \quad , \tag{4.2}$$

where the formation volume factor, B_s, and the viscosity of steam, μ_s, are evaluated at the average pressure and temperature.

Because the high mobility and storativity contrasts exist at the boundary between the inner (swept) region and the outer (unswept) region, the boundary acts as a closed boundary for a short time. Thus, the infinite-acting radial flow is followed by the pseudosteady state flow. The pressure vs. shut-in time will yield a Cartesian straight line characteristic of the swept volume. Using the slope of th. straight line, the swept volume can be calculated from

$$V_{sc} = \frac{(5.615)(q_s)_{sc}B_s}{(24)m_c \phi c_t} \quad , \tag{4.3}$$

where c_t is the total compressibility, which is almost equal to the two-phase compressibility $c_{2\phi}$ based on the volume transformed and heat released due to phase change (*Grant* and *Sorey*, 1979):

$$c_{2\phi} = \frac{\left[(1-\phi)\rho_f C_f + \phi S_w \rho_w C_w\right](\rho_w - \rho_s)}{\phi L_v (\frac{dp_s}{dT})(\rho_w \rho_s)} \quad . \tag{4.4}$$

Using the Clausius-Clapeyron equation to approximate the slope dp_s/dT and using oilfield units, $c_{2\phi}$ is (*Walsh et al.*, 1981):

$$c_{2\phi} = (0.18513)\frac{<\rho C>}{\phi}\left(\frac{\rho_w - \rho_s}{Lv\rho_w\rho_s}\right)^2 (T + 460) \quad , \tag{4.5}$$

where

$$<\rho C> = (1-\phi)\rho_f C_f + \phi S_w \rho_w Cw \quad . \tag{4.6a}$$

The two-phase compressibility $c_{2\phi}$ (Eq. 4.5) developed by *Grant* and *Sorey* (1979) assumes that only water and steam exist. In practical oilfield cases, at least 3 phases (oil, water and steam) exist. If the oil phase is also considered, the term $\phi\rho_o S_o C_o$ may be added into (ρC):

$$(\rho C) = (1-\phi)\rho_f C_f + \phi S_w \rho_w Cw + \phi S_o \rho_o C_o \quad . \tag{4.6b}$$

This implies that the total compressibility for multiphase flow in steam injection processes should be further investigated.

The steam formation volume factor, B_s, is given by

$$B_s = \frac{\vartheta_s}{(\vartheta_s)_{sc}} \quad . \tag{4.7}$$

The steam specific volume, ϑ_s, is calculated from

$$\vartheta_s = \frac{zRT}{pM} \quad . \tag{4.8}$$

Because z -values cannot be obtained directly from the simulation output file in our study, Redlich-Kwong equation of state (*Redlich* and *Kwong*, 1949) is used to obtain z -values, using the technique of successive approximations of real roots (Newton Method). Redlich-Kwong equation of state is also used in the simulator ISCOM 4.0 (*CMG*, 1987). Using the z -values obtained from this method to calculate ϑ_s, it was found that the values of ϑ_s were close to the values from the saturated-steam-property table (*Perry* and *Green,* 1984).

The water density is calculated from (*Amyx et al.*, 1960):

$$\rho_w = \frac{(\rho_w)_{sc}}{[1+\beta_p(T-T_{sc})][1-c(p-p_{sc})]} \quad . \tag{4.9}$$

For T_{sc} = 520 °R, p_{sc} = 14.7 psia, $(\rho_w)_{sc}$ = 62.4 lb/ft^3, and the input data β_p and c are 1.06083x10^{-3} °R^{-1} and 4x10^{-6} psi^{-1}, respectively, Eq. 4.9 becomes

$$\rho_w = \frac{62.4}{[1+1.06083\times10^{-3}(T - 520)][1-4\times10^{-6}(p - 14.7)]} \quad . \tag{4.10}$$

For steam, the flow rate, $(q_s)_{sc}$, is the actual steam injection rate given by

$$(q_s)_{sc} = (q_w f_s)_{sc} (\rho_w)_{sc} (\vartheta_s)_{sc} \quad . \tag{4.11}$$

4.1.2 Identification of Flow Regions

From Eqs. 4.1 and 4.3, the calculated permeability and swept volume are inversely proportional to the slopes of the straight lines. This means that it is very important for the correct straight lines to be chosen. To achieve this purpose, semilog pressure derivative method (*Bourdet et al.*, 1983, and *Bourdet et al.*, 1989) is used to identify the various flow regions. The semilog pressure derivatives are calculated from the falloff data using *Ambastha* 's differentiation algorithm (1991). A log-log graph of the semilog pressure derivatives ($dp_{ws}/dln\ (\Delta t)$) vs. shut-in times is plotted. The semilog pressure derivative graph shows as a unit slope line for wellbore-storage-dominated flow, a constant derivative value for infinite-acting radial flow, and a unit slope line for pseudosteady state flow.

4.1.3 Estimation of the Average Pressure and the Average Temperature

When average fluid and rock properties are calculated, the average pressure and the average temperature must be determined. As pointed out in the literature review, different investigators used different methods to obtain average pressures and temperatures. *Issaka* and *Ambastha* (1992) compared the average pressures from different investigators' methods with the volume-averaged gridblock pressures. They concluded that the average pressure from the *Ziegler* method (1990) was the closest to the volume-weighted average pressure, i.e., pressure obtained by extrapolating the pseudosteady Cartesian straight line to zero time was found to be an accurate estimate of the average pressure. In our study, we found that the average pressures from the *Ziegler* method was almost identical to the volume-weighted average of the gridblock pressures.

This study uses the volume-weighted average of pressures in the swept zone at the instant of shut-in. For the field well tests, the *Ziegler* method is recommended to calculate the average pressure.

The steam saturation temperature corresponding to the saturation pressure may be obtained from published steam property tables or diagrams. In our study, the average temperature is obtained from the average pressure according to the saturated-steam-property functional correlations presented by *Tortike* and *Farouq Ali* (1989). The average temperature calculated in this manner is almost the same as the volume-weighted average of temperatures in the swept zone at the instant of shut-in.

4.1.4 Wellbore Radius

When calculating skin factor, we use the effective well-block radius, equivalent to the radius where the actual flowing pressure equals the numerically calculated well-block pressure (WBP). It is given by *Peaceman* (1983) as follows:

$$r_w = 0.14\,(\Delta x^2 + \Delta y^2)^{1/2}\ . \tag{4.12}$$

When $\Delta x = \Delta y$,

$$r_w = 0.2\,(\Delta x)\ . \tag{4.13}$$

4.2 Gas Well Testing Analysis

Eqs. 4.1 through 4.3 treat steam injection processes as a kind of liquid injection processes. In the typical steam injection process, the injected steam is usually of medium to high quality (i.e., greater than 50%). Thus, the injected fluid can be thought of as being volumetrically dominated by a vapor phase. Furthermore, the well tests are designed to determine the gas-dominated, swept-region properties. These factors suggest that a pressure transient technique designed for gas injection or production may yield better accuracy.

4.2.1 Pressure Squared Method

Starting from Eqs. 4.1 through 4.3, the following pressure squared calculation formula can be derived (Appendix A):

$$k_{ec} = \frac{12085.4\ (q_w f_s)_{sc}\ \bar{z}\,\bar{T}\,\bar{\mu}_s}{m_s' h} \quad , \tag{4.14}$$

$$s = 1.1513\left(\left(\frac{p_{wfs}^2 - p_{1hr}^2}{m_s'}\right) - \log\left(\frac{k_{ec}}{\phi\,\bar{\mu}_s c_t r_w^2}\right) + 3.23 \right) \quad , \tag{4.15}$$

$$V_{sc} = \frac{17.389\ (q_w f_s)_{sc}\,\bar{z}\,\bar{T}}{\phi\, c_t m_c'} \quad , \tag{4.16}$$

where m_s' is the slope of a straight line on a graph of p_{ws}^2 vs. $\log(\Delta t)$ measured in psia^2/cycle, m_c' is the slope of a straight line on a graph of p_{ws}^2 vs. Δt measured in psia^2/hr, q_w is the surface cold water equivalent (CWE) injection rate of steam (STB/D), f_s is the steam quality (fraction). The standard conditions of $p_{sc} = 14.7$ psia and $T_{sc} = 520$ °R are used. The average temperature $\bar{T}$ is the steam saturation temperature corresponding to the average steam saturation pressure. The average steam viscosity and total compressibility are calculated from the average pressure and temperature. The average pressure and temperature are estimated using the same method as for the pressure analysis.

4.2.2 Pseudo-pressure Function Method

The use of the real gas law concept naturally suggests the use of pseudo-pressure function analysis for greater calculation accuracy. Similarly, we have the following equations for pseudopressure function analysis method (Appendix A):

$$k_{ec} = \frac{12085.4\ (q_w f_s)_{sc}\,\overline{T}}{m_s'' h} \quad , \tag{4.17}$$

$$s = 1.1513\left((\frac{\psi_{wfs} - \psi_{1hr}}{m_s''}) - \log(\frac{k_{ec}}{\phi\,\overline{\mu}_s c_t r_w^2}) + 3.23 \right) \quad , \tag{4.18}$$

$$V_{sc} = \frac{17.389\ (q_w f_s)_{sc}\,\overline{T}}{\phi\,\overline{\mu}_s c_t m_c''} \quad , \tag{4.19}$$

where m_s'' is the straight line slope of ψ_{ws} vs. $\log(\Delta t)$ measured in psia^2/(cp·cycle), m_c'' is the straight line slope of ψ_{ws} vs. Δt measured in psia^2/(cp.hr). The pseudo-pressure function is calculated by the computer program (Appendix B). Appendix C is an example of the input and output data for this program. Other conditions are the same as the pressure squared analysis method.

CHAPTER 5

SIMULATION STUDY OF THERMAL WELL TESTING FOR NON-DIPPING AND DIPPING RESERVOIRS

The numerical simulation study is carried out to evaluate the accuracy and applicability of the pseudosteady state method in the estimation of swept volume for non-dipping and dipping reservoirs under steam injection. Attempts are also made to obtain steam effective permeability within the swept zone from the well testing data.

The ISCOM 4.0 (*CMG*, 1987) is used to simulate steam injection falloff testing during the course of steamflood in non-dipping and dipping reservoirs. Steam is injected into reservoir models until appreciable rock volumes are swept. Pressure falloff tests are then simulated by shutting in the injection well and noting the wellbore gridblock pressures as a function of time. The data are analyzed using the methodology described in Chapter 4. The main assumption in the study is that the simulator ISCOM 4.0 accurately depicts the pressure transient responses in the reservoir models.

5.1 Simulator

The numerical simulator ISCOM 4.0 (*CMG*, 1987) is used in this study. It was developed by the Computer Modelling Group in Calgary (CMG). It is a multi-component, four-phase (gas, oil, water and coke phase) model that has been extensively tested. It models flow of mass and energy, heat conduction, heat loss, vaporization/condensation, injection/production, and a general chemical reaction scheme. Gravity and capillary effects can be included. A fully-implicit solution method is employed in this model. The model operates in 1-, 2-, and 3-dimensional Cartesian, cylindrical or curvilinear coordinates, and is capable of simulating a well completion in directions *parallel* to any of the coordinate axes. However, it is very difficult to simulate well completions in the directions inclined to any of the coordinate axes for the cases in dipping reservoirs.

5.2 Reservoir and Fluid Model

The reservoir and fluid data typical of heavy oil reservoirs are used in this study. The effects of gridblock sizes and well directions are also discussed.

5.2.1 Reservoir and Fluid Properties

Table 5.1 gives the reservoir and fluid properties used in this simulation study. Table 5.2 gives the viscosity vs. temperature relationship for the reservoir fluids (water, oil and steam). The heavy oil is assumed to be a single-component dead oil with a gravity of 15.4 °API [0.962 g/cm^3]. The water-oil and gas-oil relative permeabilities used in simulation are shown in Figures 5.1 and 5.2, respectively. The saturation end points are temperature-independent in this study.

5.2.2 Reservoir Gridblock Sizes

The reservoir model used in this study is of a formation area of 146,589 ft^2 and of formation thickness of 40 ft. The reservoir volume is 5,863,560 ft^3. The gridblock sizes are different for different gridblock models. For all models, one injection well is located in the center of the reservoir.

TABLE 5.1 - RESERVOIR AND FLUID PARAMETERS USED IN SIMULATION

Initial reservoir pressure, psia	700
Initial reservoir temperature, °F	93
Porosity, fraction	0.35
Initial water saturation, % PV	51
Initial oil saturation, % PV	49
Horizontal absolute permeability, md	700
Vertical absolute permeability, md	70
Pore compressibility, $psi^{-1} \times 10^{-6}$	300
Water compressibility, $psi^{-1} \times 10^{-6}$	4.0
Oil compressibility, $psi^{-1} \times 10^{-6}$	7.3
Formation thickness, ft	40
Formation volumetric heat capacity, BTU/(ft^3·°F)	35
Formation thermal conductivity, BTU/(ft·D·°F)	24
Oil density at the initial conditions, °API	15.4 (0.962 g/cm^3)
Oil viscosity at the initial reservoir conditions, cp	2094
Steam injection pressure, psi	1326.2
Injected steam temperature, °F	580
Injected steam quality, fractional vapor mass	0.80

TABLE 5.2 - VISCOSITY-TEMPERATURE RELATIONSHIP FOR RESERVOIR FLUIDS

Temperature, °F	Water, cp	Oil, cp	Steam, cp
90	0.7714	2401	0.009726
100	0.6846	1377	0.009916
200	0.3081	47.04	0.011833
300	0.1820	8.494	0.013771
400	0.1486	3.960	0.015729
500	0.1265	2.501	0.017705
600	0.1265	2.500	0.019695

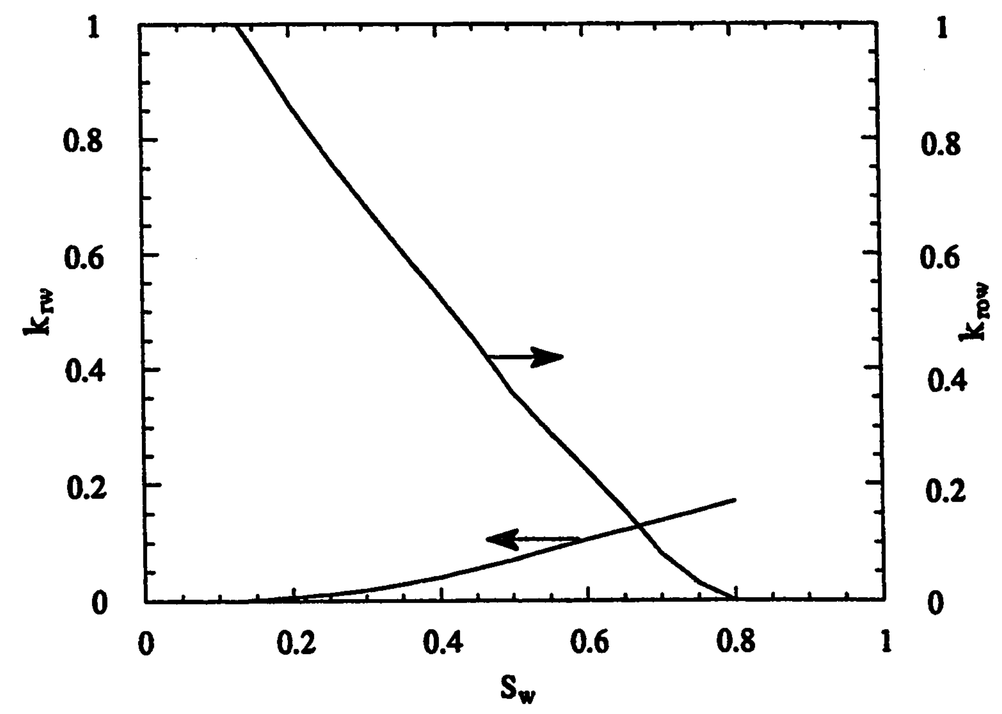

Fig. 5.1 - Water/oil relative permeability curve.

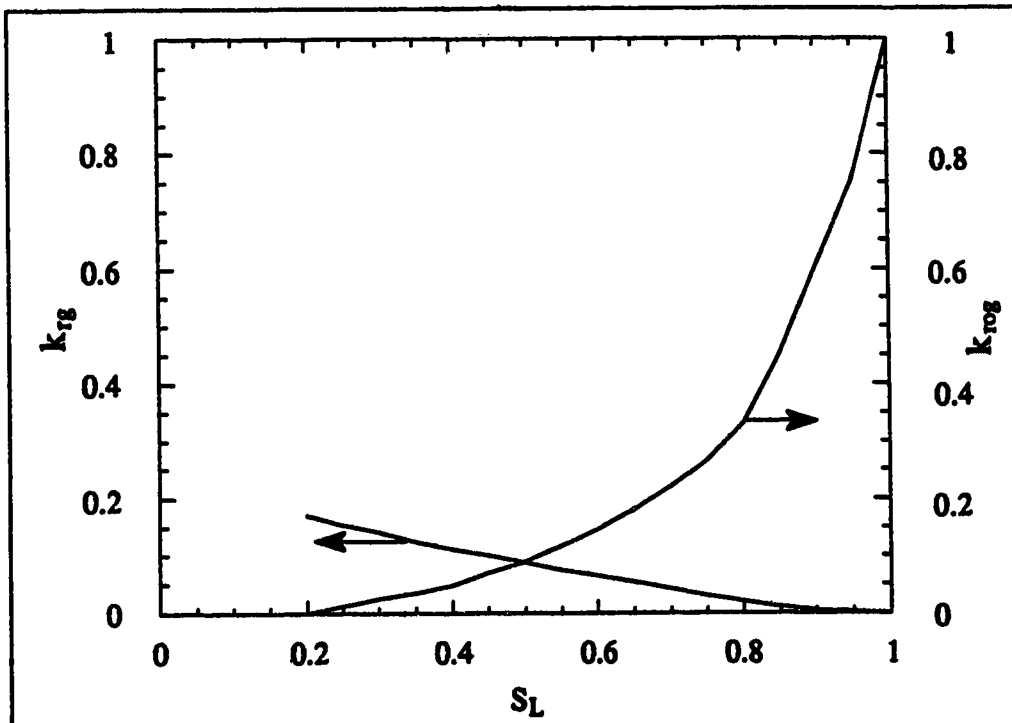

Fig. 5.2 - Gas/oil relative permeability curve.

5.2.2.1 Effects of Gridblock Sizes and Wellbore Gridblock Sizes

To determine reservoir gridblock sizes, the effect of gridblock sizes and wellbore gridblock sizes must be first investigated. Table 5.3 shows the gridblock sizes and wellbore gridblock sizes for Test Runs 1 through 4, the corresponding semilog slope graphs are plotted in Figures 5.3 through 5.6. In all cases, a fully-penetrating well is considered. Because of the flow symmetry, only one quarter of the reservoir is simulated. Table 5.3 and Figures 5.3 through 5.6 show that wellbore gridblock sizes and the gridblock sizes near the wellbore gridblock influence wellbore storage effect. For Test Runs 1 and 2, though the wellbore blocks are small enough, the infinite-acting radial flow regime is still masked by wellbore storage. For Test Run 2, though wellbore block sizes are reduced to 2 x 2 ft from 3 x 3 ft of Test Run 1, wellbore storage effect has not been reduced. Test Run 3 shows that a refinement of vertical wellbore blocks does not help to reduce the wellbore storage effect or to identify the flow regimes. With smaller gridblocks around the wellbore gridblock, Test Run 4 successfully shows the flow regimes, though the wellbore block sizes are the same as Test Run 1. These test runs show that the gridblocks around wellbore must also be refined to reduce wellbore storage effect, so that flow regimes can be identified.

TABLE 5.3 - GRIDBLOCK SIZES FOR TEST RUNS

Test Run No.	dip (degree)	No. of grid blocks	Wellbore Block Sizes (ft x ft)	Gridblock Sizes(ft) I	J	K
1	0	4x3x2	3 x 3	250,50,15,3	100,15,3	2x60
2	0	4x3x2	2 x 2	250,50,15,2	100,15,2	2x60
3	0	4x3x8	3 x 3	250,50,15,3	100,15,3	8x15
4	0	4x4x2	3 x 3	300,10,5,3	100,10,5,3	2x60

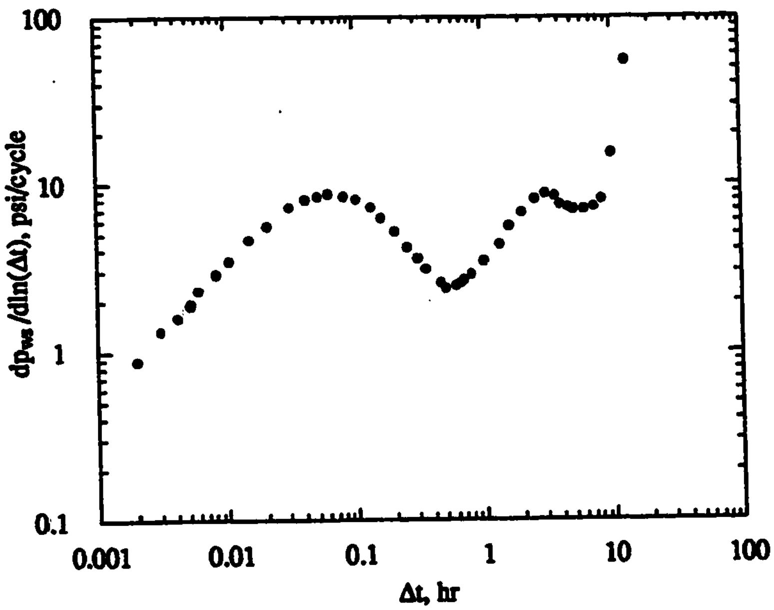

Fig. 5.3 - Semilog pressure derivative data for Test Run 1.

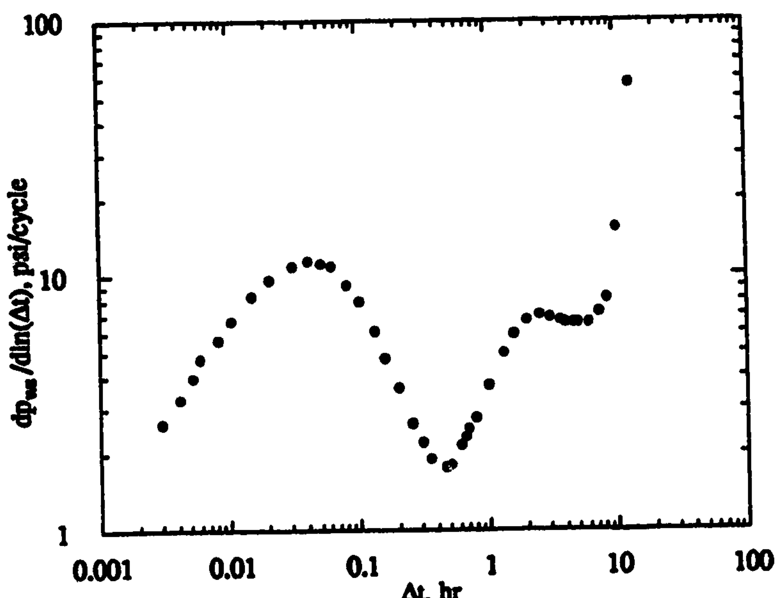

Fig. 5.4 - Semilog pressure derivative data for Test Run 2.

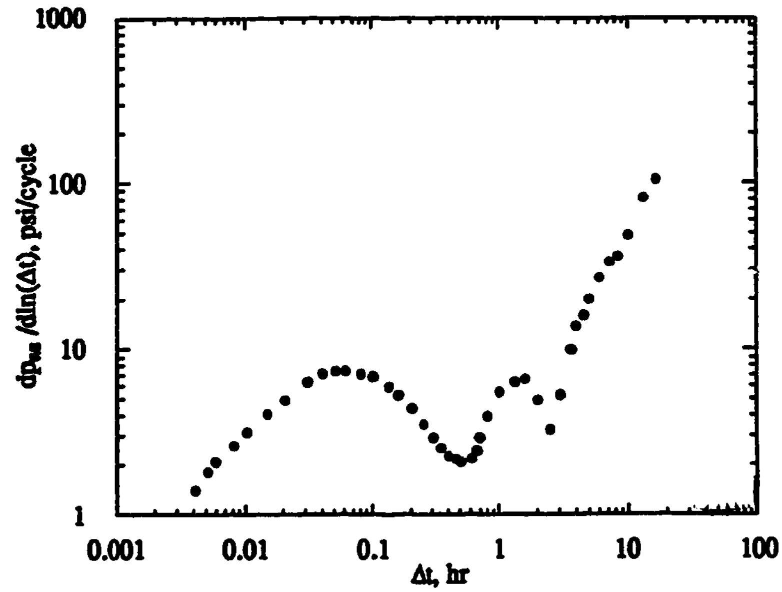

Fig. 5.5 - Semilog pressure derivative data for Test Run 3.

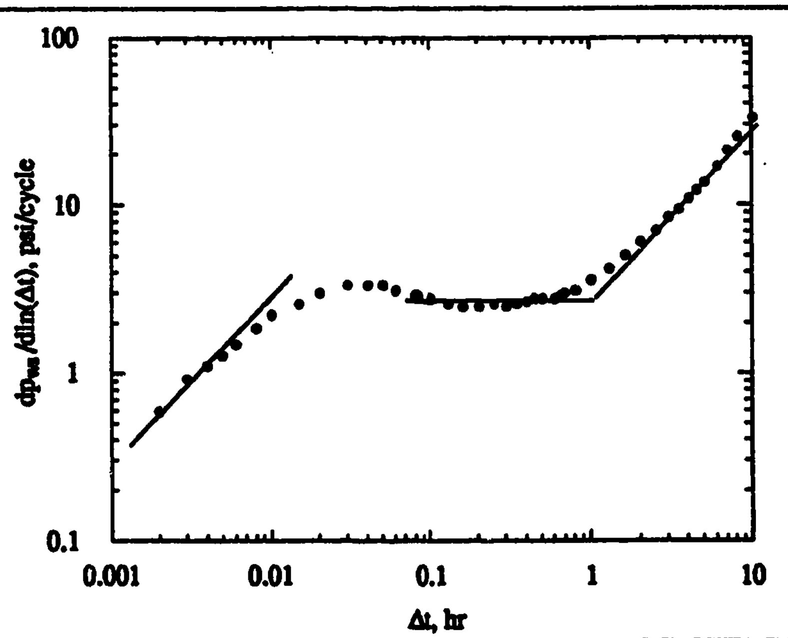

Fig. 5.6 - Semilog pressure derivative data for Test Run 4.

5.2.2.2 Determination of Gridblock Sizes for Different Models

From Section 5.2.2.1, the gridblocks around wellbore must be refined. To obtain more accurate estimates for simulated swept volumes, the gridblocks around the front should also be refined. To consider the effects of gravity, vertical gridblocks need to be refined. But we are restricted by the maximum number of vertical gridblocks and the maximum number of total gridblocks, which are 8 and 380, respectively, in the ISCOM accessible to us. For our reservoir model, the gridblock sizes used for different models are shown in Table 5.4.

Except *Fassihi* (1988), and *Issaka* and *Ambastha* (1992), other investigators published the results obtained from radial models. Starting from the radial and areal models, 3D models are used in this study. With the radial and areal models, we could compare our results with other investigators' results, and check whether our results are dependent upon gridblocks or models. With 2D models converted into 3D models, gravity effects could be investigated.

With the flow symmetry of non-dipping reservoirs around the well, 3D model I is used to simulate one quarter of the reservoir to reduce the number of gridblocks required. 3D model II is used to simulate one-half of the dipping reservoir because of the flow symmetry in the J direction. Since more steam would go up along the dipping plane, the well is shifted one block down in 3D model II, compared with 3D model I. The models using 7x7x1 and 7x7x4 gridblocks are used in Runs 4 and 5, respectively, to study the effect of gravity.

TABLE 5.4 - GRIDBLOCK SIZES USED IN THIS STUDY

Model	Gridblocks IxJxK	Well Location (I,J)	Gridblock Sizes(ft) I	J	K	Used in Runs
Radial Model	37x1x1	(1,1)	See Table 5.6	2π	40	1, 1*
Areal Model	8x8x1	(8,8)	140,10,10,10,10,10,5,3	130,10,10,10,10,10,5,3	40	2, 2*
	7x7x1	(7,7)	150,10,10,10,10,5,3	140,10,10,10,10,5,3	40	4
3D Model I	8x8x3	(8,8)	140,10,10,10,10,10,5,3	130,10,10,10,10,10,5,3	13.3,13.3,13.3	3, 3*, 10, 11
	7x7x4	(7,7)	150,10,10,10,10,5,3	140,10,10,10,10,5,3	10,10,10,10	5
3D Model II	15x8x3	(7,8)	140,10,10,10,10,5,3,5 10,10,10,10,10,10,140	130,10,10,10,10,10,5,3	13.3,13.3,13.3	6 - 9, 6* - 9*

5.2.3 Well Directions for Dipping Reservoirs

For a non-dipping reservoir, the vertical well direction is parallel to the Z coordinate axis. For a dipping reservoir, the well direction is inclined to the coordinate axes. Two approaches to deal with the well directions in dipping reservoirs have been published. The first one is that the well direction is vertical as shown in Figure 5.7 (for a vertical well). The second is that the well direction is perpendicular to the bedding plane (dipping plane) as shown in Figure 5.8 (for an inclined well).

Moughamian et al. (1982) employed the first approach. A highly implicit steamflood simulator (*Coats*, 1976) was used in their study. The dip in their model was 53°. *Hong* (1988, 1990 and 1991) employed the second approach of representing wells as per Figure 5.8. The dip was up to 45°. He used the simulator ISCOM (*Rubin* and *Buchanan*, 1985) in 1988, which was developed by the Computer Modelling Group (CMG) of Calgary, Canada. In 1990 and 1991, he used Chevron Oil Field Research Company's Steam Injection Simulator SIS3 (*Aziz et al.*, 1987). The simulator ISCOM 4.0 (*Anon.*, 1987) is used in our study, which was also developed by CMG.

Depending on the drilling practices, either an inclined or a vertical well may occur in a dipping reservoir. However, it does not appear feasible to specify a vertical well in a dipping reservoir in ISCOM 4.0. Hence, the second approach (Figure 5.8) of specifying wells in dipping reservoirs is used throughout in this study.

5.3 Simulation Results and Discussion

Using the obtained radial model, areal model and the 3D models, eighteen simulation runs are analyzed in this study. The first eleven runs are analyzed to determine the method to identify the swept zone, to evaluate the accuracy of the thermal well testing, and to

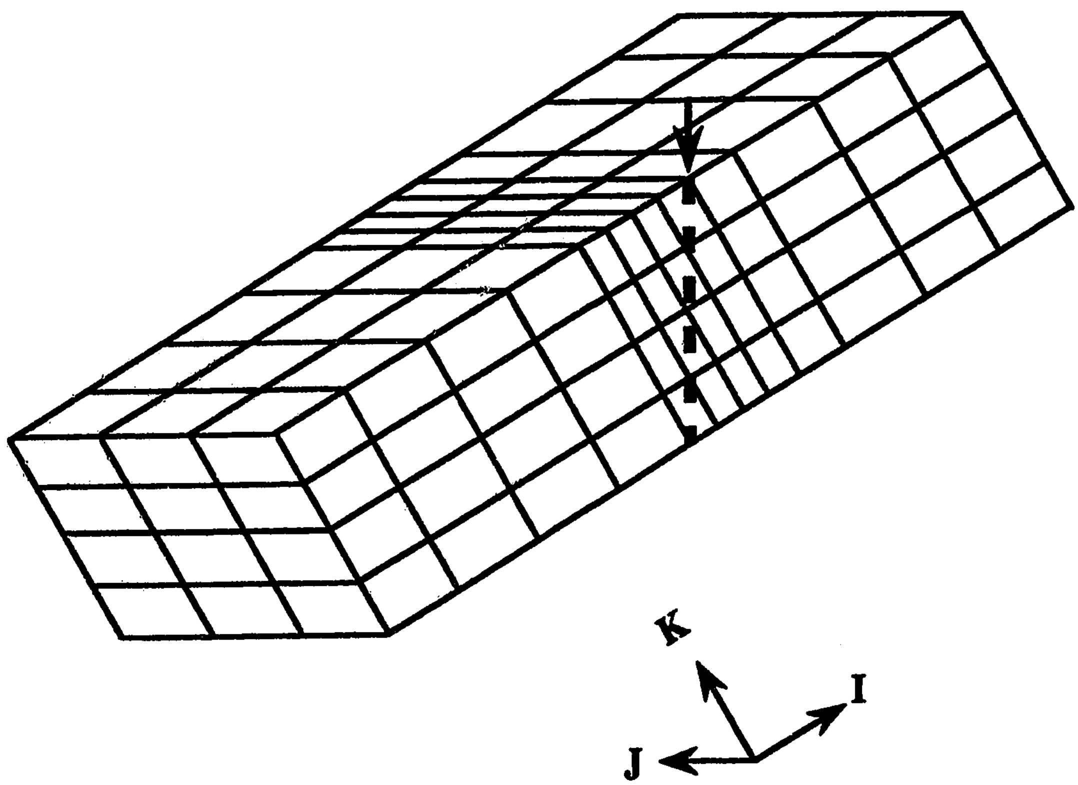

Fig. 5.7 - 3D Schematic model of a dipping reservoir for a vertical well.

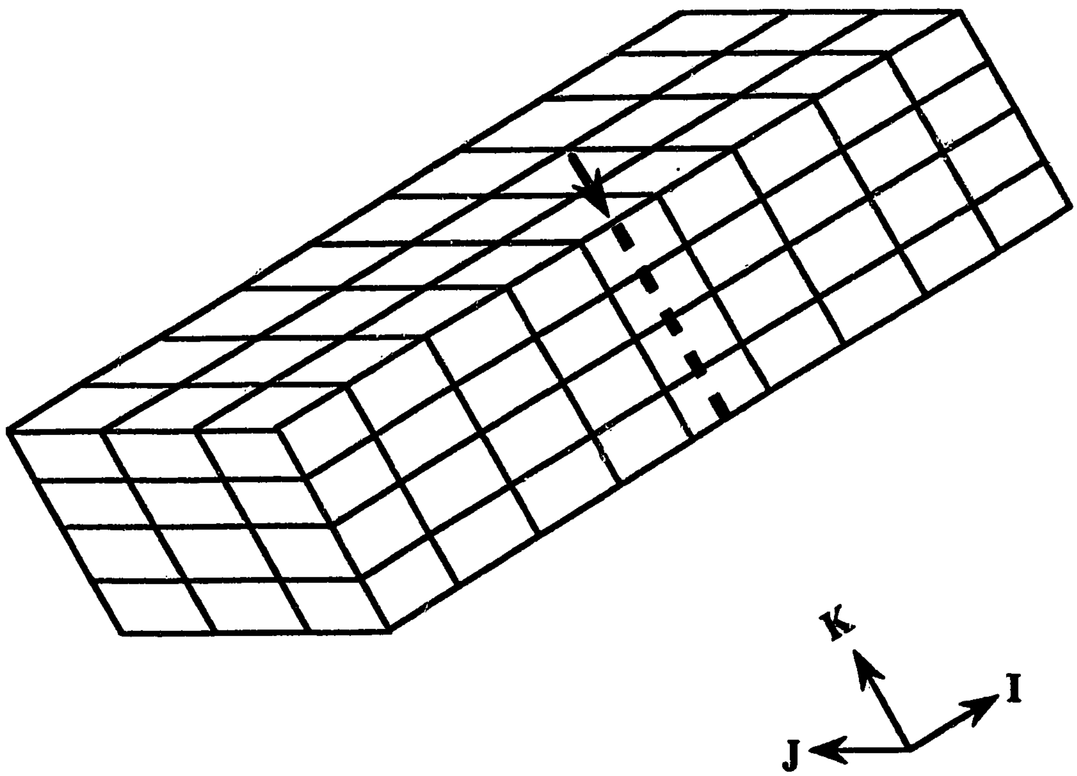

Fig. 5.8 - 3D Schematic model of a dipping reservoir for an inclined well.

investigate the effects of gravity segregation, the shape of swept zone and dip. The investigation of the effect of anisotropy in permeability is carried out to confirm the effects of gravity and shapes of swept zones. The application in dipping reservoirs is investigated by studying the effect of dip angle. Real gas analysis is carried out to seek the possibility for a more quantitative accuracy than from the liquid analysis. The other seven ideal gas cases are analyzed to further verify the validity of thermal well testing. The simulated falloff test results and conditions are shown in Table 5.5. The figures of calculation for each run are attached in Appendix D.

5.3.1 Determination of the Method to Identify the Swept Zone

During steam injection processes, three zones are formed: steam zone, hot water zone and cold oil zone. Two fronts are formed: steam front and hot water front. The question is whether the calculated volume from falloff tests includes the volume of hot water zone. Table 5.6 shows the block and effective properties for Run 1. In this run, the radial model was used, steam injection rate was constant at 500 STB/D cold water equivalent (CWE) with 80% steam quality, and the duration of injection was 30 days. From Column (7), the total mobility contrast in this run is at block 28, which corresponds to zero steam saturation front (see Column (5)). The ratio of the total mobilities between block 28 and block 29 is about 8.0. The hot water zone is at block 29. At the hot water front between block 29 and block 30, the total mobility ratio is about 16. The mobility contrast at the steam front should be high enough, so that it would behave like a closed boundary. In other words, the pressure responses will first reflect the effect of this front. Hence, the swept volume deduced from pressure falloff analysis should include only the volume of steam zone.

TABLE 5.5 - SIMULATED FALLOFF TEST RESULTS AND CONDITIONS

(1) Run No.	(2) Dip (degree)	(3) q_w (STB/D)	(4) t (days)	(5) $\overline{p}$ (psia)	(6) $\overline{T}$ (°F)	(7) $\overline{S}_g$ (%)	(8) k_e at $\overline{S}_g$ (md)	(9) k_{ec} (md)	(10) k_{ec}/k_e	(11) s	(12) V_s (ft^3)	(13) V_{sc} (ft^3)	(14) V_{sc}/V_s	(15) Gridblocks
1	0	500	30	1072.1	553.0	50.28	62.1	80.2	1.29	0.85	265904	278582	1.05	37x1x1
2	0	500	30	990.6	543.4	45.86	52.6	81.1	1.54	0.45	217960	241658	1.11	8x8x1
3	0	500	30	980.0	542.1	48.54	58.9	80.5	1.37	0.22	211021	261912	1.24	8x8x3
4	0	500	30	961.6	540.0	51.50	64.1	80.4	1.25	0.38	185960	230010	1.24	7x7x1
5	0	500	30	972.5	541.2	50.20	61.9	85.1	1.37	0.44	204760	220894	1.08	7x7x4
6	15	500	30	984.4	542.8	48.76	59.3	81.7	1.38	0.45	210488	258551	1.23	15x8x3
7	30	500	30	984.0	542.6	47.90	57.8	83.4	1.44	0.50	211821	263330	1.24	15x8x3
8	45	500	30	981.0	542.2	48.06	58.1	80.9	1.39	0.48	210488	259604	1.23	15x8x3
9	90	500	30	978.1	541.9	48.91	59.6	79.4	1.33	0.48	201960	231863	1.15	15x8x3
10	0	500	30	972.0	541.1	50.71	62.8	81.4	1.30	0.45	196622	241845	1.23	8x8x3
11	0	500	30	991.5	543.5	49.26	50.9	68.1	1.34	0.46	204622	254069	1.24	8x8x3
1*	0	500	30	1095.3	555.6	53.73	67.9	84.2	1.24	1.14	254468	209678	0.82	37x1x1
2*	0	500	30	998.9	544.5	48.47	58.8	83.8	1.43	0.52	217960	191573	0.88	8x8x1
3*	0	500	30	987.3	543.0	51.13	63.5	85.3	1.34	0.68	211021	207217	0.98	8x8x1
6*	15	500	30	990.2	543.4	51.72	64.5	85.3	1.32	0.60	209155	211504	1.01	15x8x3
7*	30	500	30	993.0	543.7	50.17	61.9	86.4	1.40	0.62	214488	215674	1.01	15x8x3
8*	45	500	30	990.0	543.3	50.00	61.6	85.4	1.39	0.62	215421	215501	1.00	15x8x3
9*	90	500	30	984.1	542.6	51.27	63.7	83.2	1.31	0.51	201960	188941	0.94	15x8x3

TABLE 5.6 - BLOCK AND EFFECTIVE PROPERTIES FOR RUN 1 (RADIAL MODEL)

(1) BLOCK NO.	(2) r, ft	(3) p, psia	(4) T, °F	(5) S_g, %	(6) λ_s, md/cp	(7) λ_t, md/cp	(8) $\overline{S_g}$, %	(9) $\overline{\lambda_s}$, md/cp
1	2	1102.1	556.6	62.11	4346	4408	62.11	4346
2	4	1092.4	555.5	61.94	4333	4395	61.98	4343
3	6	1087.8	555.0	61.70	4310	4372	61.83	4338
4	8	1084.8	554.7	61.37	4277	4339	61.63	4333
5	10	1082.5	554.4	61.03	4244	4306	61.41	4327
6	12	1080.7	554.2	60.63	4203	4266	61.17	4321
7	14	1079.2	554.0	60.22	4160	4224	60.92	4314
8	16	1077.9	553.9	59.90	4130	4195	60.68	4308
9	18	1076.7	553.7	59.67	4112	4179	60.47	4302
10	20	1075.7	553.6	59.41	4091	4160	60.27	4297
11	22	1074.8	553.5	59.08	4064	4135	60.06	4291
12	24	1074.0	553.4	58.59	4024	4098	59.83	4286
13	26	1073.2	553.3	57.81	3961	4037	59.53	4280
14	28	1072.5	553.2	56.63	3864	3944	59.13	4272
15	30	1071.9	553.2	55.00	3731	3813	58.60	4263
16	32	1071.2	553.1	53.04	3555	3641	57.92	4252
17	34	1070.7	553.0	50.96	3370	3458	57.13	4237
18	36	1070.1	552.9	48.97	3184	3276	56.25	4221
19	37	1069.7	552.9	47.97	3087	3181	55.81	4212
20	38	1069.4	552.8	46.88	2981	3077	55.34	4203
21	39	1069.1	552.8	45.69	2866	2964	54.85	4193
22	40	1068.9	552.8	44.35	2751	2851	54.34	4181
23	41	1068.6	552.8	42.88	2641	2744	53.78	4169
24	42	1068.3	552.8	41.38	2529	2636	53.20	4156
25	43	1068.1	552.7	38.89	2417	2527	52.59	4142
26	44	1067.8	552.7	38.41	2296	2409	51.95	4127
27	45	1067.5	552.7	36.62	2149	2265	51.28	4111
28	46	1067.3	452.6	28.13	1412	1587	50.28	4077
29	51	1066.6	353.4	0.0	0.0	202		
30	56	1065.3	169.6	0.0	0.0	12.5		
31	61	1048.6	113.9	0.0	0.0	2.8		
32	71	955.3	96.5	0.0	0.0	74.1		
33	81	951.2	94.3	0.0	0.0	82.4		
34	101	946.6	94.0	0.0	0.0	82.0		
35	121	941.8	94.0	0.0	0.0	81.7		
36	161	936.6	93.9	0.0	0.0	81.5		
37	216.01	932.3	93.9	0.0	0.0	81.3		

The results of the areal model also supported this viewpoint. Figure 5.9 shows total mobility and steam saturation distribution for Run 2, in which the areal model was used. The injection rate and duration were the same as Run 1.

Figure 5.9 shows that the total mobility ratio is greater than 6 at the steam front. The high mobility contrast exists at the steam front. Therefore, the calculated swept volume from falloff test analysis should represent the volume of steam zone.

Figure 5.10 is the total mobility and steam saturation distribution at a shut-in time of 10 hours, which corresponds to a time after the end of the pseudosteady state in Run 2. Comparing Figure 5.9 with Figure 5.10, we could see that the total mobility and steam saturation distribution remain almost unchanged during the well test.

5.3.2 Validity of the Estimation of k, s and V_s

The results of the radial model (Run 1) and the areal model (Run 2) are analyzed to discuss the validity of the estimation of k, s and V_s from thermal falloff testing.

Figures 5.11 through 5.13 show the semilog derivative data, semilog straight line and the Cartesian straight line for Run 1, respectively. From Figure 5.11, we could easily identify the flow regimes. Infinite-acting flow lasts from $\Delta t = 0.005$ to 0.7 hours, pseudosteady state from $\Delta t = 1.3$ to 7 hours. The dotted line will be discussed in Section 5.3.3. From Figure 5.12, the slope of the semilog straight line is 10.71 psi/cycle, and the pressure at the shut-in time of 1 hour is 1068.1 psia. From Figure 5.13, the slope of the Cartesian straight line is 4.0693 psi/hr.

Using the slope of the semilog straight line and Eq. 4.1, the calculated effective permeability to steam is 80.2 md. However, the volume-weighted average steam saturation within the swept zone is 0.5028. The corresponding effective permeability to steam is 62.1 md. Thus, the ratio of the estimated permeability from the pressure falloff data to the

J \ I=	2	3	4	5	6	7	8
8	268.2	35.61 2207	51.70 3551	58.81 4151	61.25 4371	62.39 4483	62.46 4480
7	238.7	31.71 1895	50.30 3427	5[illegible].98 4085	60.67 4312	61.98 4443	62.39 4483
6	56.3	437.6	43.07 2780	53.44 3706	58.86 4155	60.67 4312	61.25 4371
5	25.0	140.0	18.51 897.6	45.56 2974	53.46 3708	58.00 4087	58.83 4153
4	74.8	20.8	108.0	18.84 916.5	43.19 2788	50.39 3435	51.79 3559
3	89.0	67.0	20.8	142.3	443.3	32.57 1964	36.33 2263
J=2	84.4	89.0	74.5	24.7	59.3	249.9	283.0

Steam front — Hot water front

Sg (%) λ_t (md/cp)

Fig. 5.9 - Total mobility and steam saturation distribution for Run 2 ($\Delta t = 0$).

	I= 2	3	4	5	6	7	8
8	276.3	36.64 2294	52.10 3601	59.19 4200	61.65 4438	62.95 4573	63.29 4608
7	244.4	30.16 1782	50.67 3474	58.34 4133	61.07 4378	62.48 4524	62.95 4573
6	56.3	437.6	43.32 2809	53.79 3706	59.24 4155	61.08 4312	61.65 4438
5	23.2	140.7	19.84 976.7	45.88 2974	53.81 3756	58.36 4135	59.18 4201
4	72.1	19.9	180.1	20.17 996.7	43.41 2815	50.76 3482	52.19 3609
3	88.4	64.3	19.9	143.2	442.8	30.89 1841	37.29 2346
J=2	83.9	88.4	71.8	22.9	60.3	255.8	291.1

Steam front — Hot water front

S_g (%)
λ_t (md/c[illegible])

Fig. 5.10 - Total mobility and steam saturation distribution for Run 2 (Δt = 10 hours).

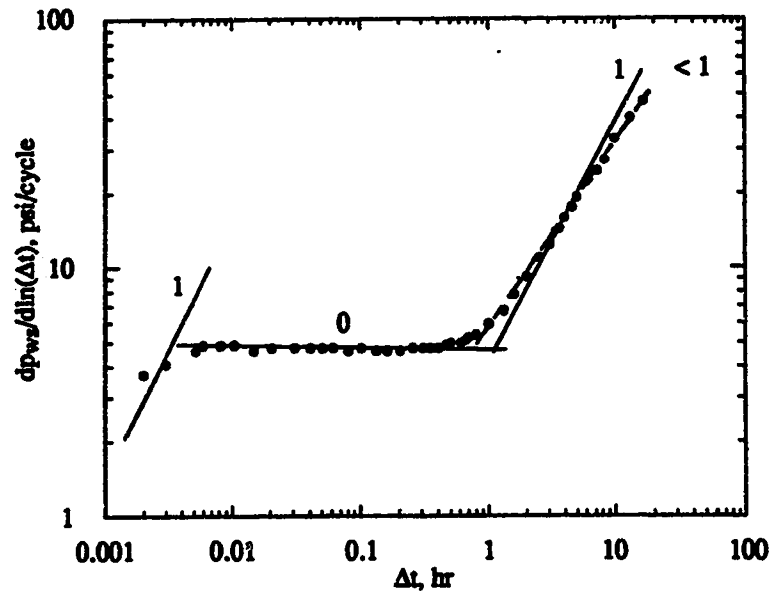

Fig. 5.11 - Semilog pressure derivative data for Run 1.

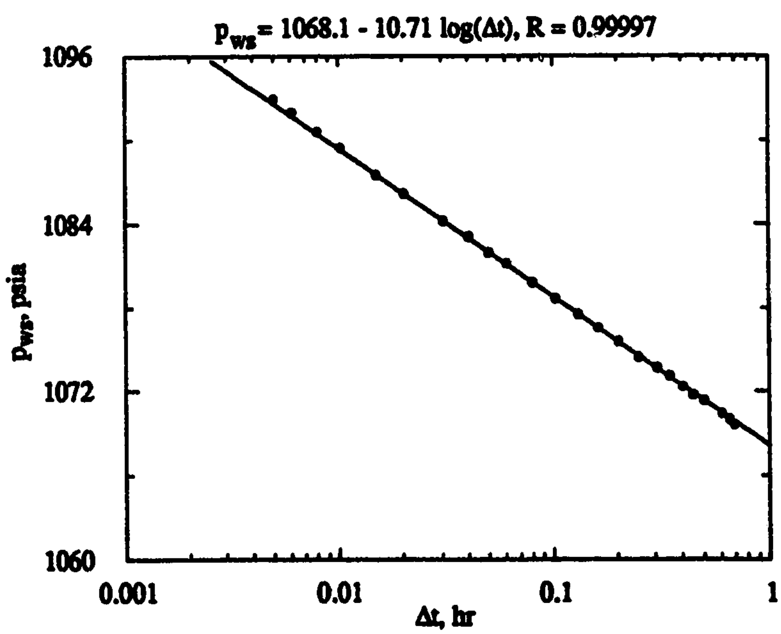

Fig. 5.12 - Semilog straight line for Run 1.

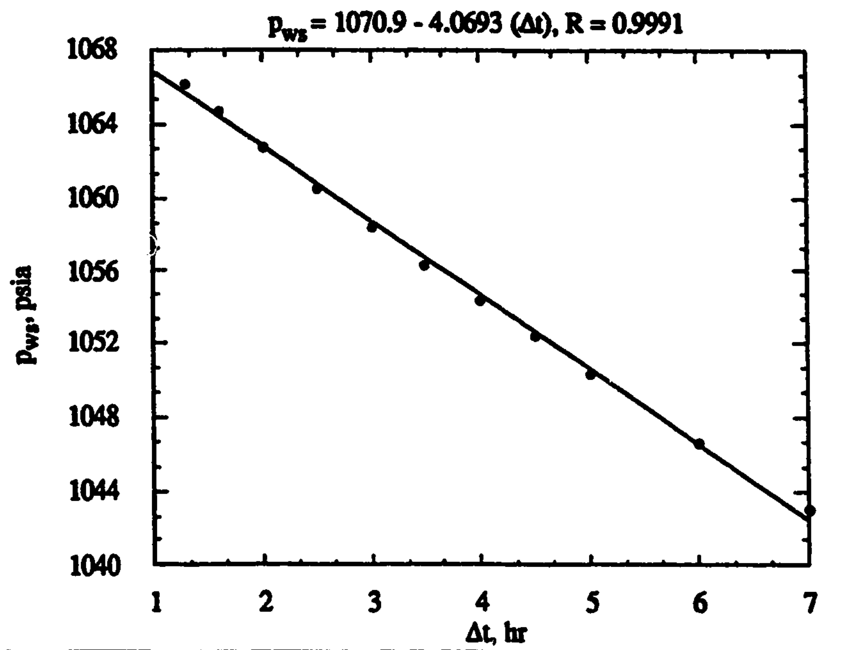

Fig. 5.13 - Cartesian straight line for Run 1.

permeability at the average steam saturation is 1.29. Using the wellbore pressure at the shut-in time of 1 hour and Eq. 4.2, the estimated skin factor is 0.85, which compares favorably with the input skin of zero.

Using the slope of Cartesian straight line of 4.0693 psi/hr (Figure 5.13), the estimated volume is 278,582 ft^3. Compared with the simulation swept volume, 265,904 ft^3, the ratio of the estimated volume to the simulation volume is 1.05.

Although the estimated swept volume represents the simulation swept volume within engineering accuracy, the estimated permeability from well testing does not represent the permeability of steam at the volume-weighted average steam saturation. This result suggests that the permeability at the volume-weighted average saturation is not the effective permeability within the swept zone. This could be explained by a special case, in which steam relative permeability is a linear function of steam saturation, and viscosity is constant. The case of Run 1 is similar to such a case (see the relative permeability curve in

Figure 5.2 and the pressure distribution in Column (3) of Table 5.6, where small pressure changes mean that viscosity is almost constant within the steam zone). In such a case, calculation of effective permeability from volume-weighted average saturation is equivalent to calculation of effective mobility from volume-weighted mobilities. The volume-weighted average mobility within the swept zone for Run 1 is 3,304 md/cp. However, according to the flow resistance concept, the effective steam mobility $\overline{\lambda}_s$ in the steam zone should be calculated from the following formula (*Onyekonwu et al.*, 1984):

$$\overline{\lambda}_s = \frac{\ln(r_N/r_w)}{\sum_{i=1}^{N} \left((\lambda_s^{-1})_i \ln(r_i/r_{i-1}) \right)} \quad , \tag{5.1}$$

where N = total number of grid blocks in the steam zone, and $r_o = r_w$. The calculated effective steam mobility $\overline{\lambda}_s$ from Eq. 5.1 is 4,077 md/cp (see Column (9) of Table 5.6). This mobility of 4,077 md/cp should be the real effective mobility within the steam swept zone, and thus the volume-weighted average mobility of 3,304 md/cp is not the effective steam mobility within the steam swept zone. If the viscosity of 0.01881 cp at the average pressure within the steam zone is used, the mobility of 3,304 md/cp is equivalent to the permeability of 62.1 md, which is equal to the effective permeability at the volume-weighted average steam saturation. Thus, the permeability at the volume-weighted average steam saturation is not the effective permeability. The effective permeability will be 76.7 md corresponding to the effective mobility of 4077 md/cp. The ratio of the estimated permeability of 80.2 md from well testing data to this effective permeability of 76.7 md is 1.05. The two permeabilities seem to be comparable.

However, the estimated permeability of 80.2 md from well testing data is equivalent to an effective mobility of 4,264 md/cp, with the viscosity of 0.01881 cp used. This mobility corresponds to the effective mobility within the zone of the radial distance of 30 ft, or at block 15 (see Table 5.6). This zone is a high steam saturation zone, with steam saturations greater than 55% in this run. The values of the saturation for different runs could be different, but this phenomenon was found to be common. Therefore, the permeability estimated from well testing data reflects the effective permeability of a high steam saturation zone some distance around the injection well. This viewpoint could be further verified using the results of Run 2.

Figures 5.14 through 5.16 show the semilog pressure derivative data, the semilog straight line and the Cartesian straight line for Run 2, respectively. The slope of the semilog straight line is 11.371 psi/cycle. The slope of the Cartesian straight line is 4.5116 psi/hr. The pressure at shut-in time of 1 hour is 986 psia. The dotted line and the points A through F will be discussed in Section 5.3.3.

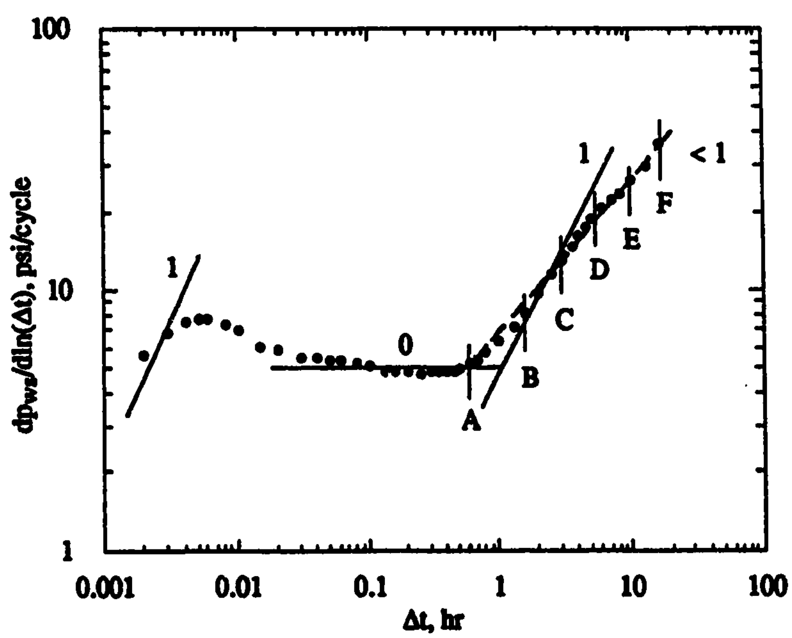

Fig. 5.14 - Semilog pressure derivative data for Run 2.

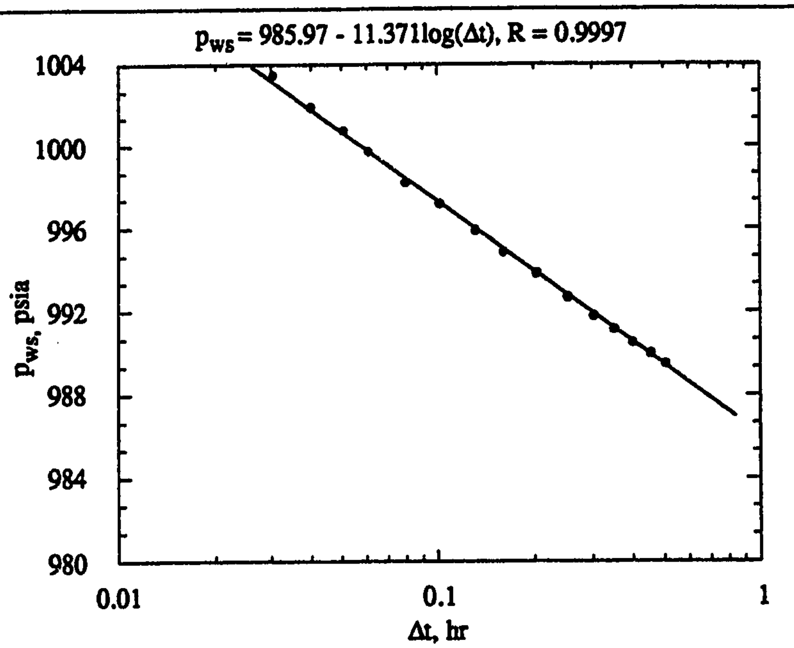

Fig. 5.15 - Semilog straight line for Run 2.

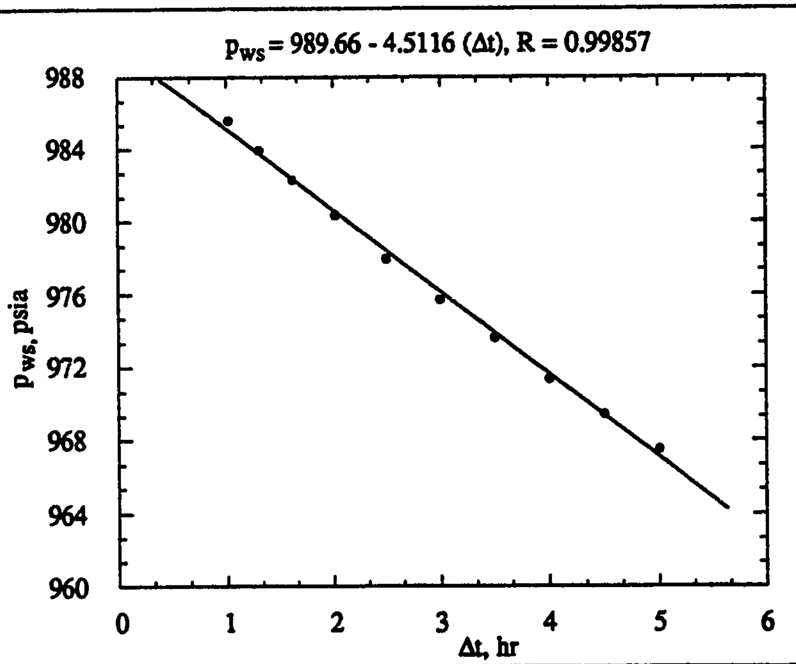

Fig. 5.16 - Cartesian straight line for Run 2.

Because no formula to calculate effective mobility in an areal model exists, the mobility is not for comparison. The permeability is estimated to be 81.1 md from the pressure falloff data. The volume-weighted average steam saturation is 0.4586, which corresponds to the permeability of 52.6 md. The ratio of the estimated permeability to the permeability at the average steam saturation is 1.54. The estimated skin factor is 0.45. The ratio of the estimated volume of 241,658 ft^3 to the simulation volume of 217,960 ft^3 is 1.11 (see Table 5.5). The skin factor and the swept volume are favorably estimated. The permeability is overestimated.

Further investigation of the steam distribution (Figure 5.9) leads us to find that the calculated permeability from well tests would not reflect the permeability at the volume-weighted average saturation. In Figure 5.9, if we do not consider the steam saturations at Blocks (4, 5) and (5, 4), 0.1851 and 0.1884, respectively, which are relatively small, the average saturation for the swept zone will be 0.5054. The corresponding permeability is 62.5 md. Thus, the ratio of the calculated permeability of 81.1 md to the permeability of 62.5 md at the average steam saturation is changed to 1.30, 24% closer to 1.0. This example illustrates that few blocks of small saturations along the steam front could result in a small volume-weighted average saturation. Consequently, the permeability at the average saturation would be much less than that calculated from falloff well testing data. Actually, the pressure responses during the infinite-acting flow should reflect the flow before the effects of the front are felt. In other words, the infinite-acting flow would end before the effects of blocks of relatively very small steam saturations along the front are felt. Hence, the permeability calculated from well testing could not simply be compared with the permeability corresponding to the volume-weighted average steam saturation.

Figure 5.9 shows that the steam saturations decrease gradually from the wellbore block to the steam front, and the saturations decrease faster along the steam front. This phenomenon also happens in other runs. Further investigation of the steam distributions of other runs leads us to find that the high steam saturations around injection wells in each case are almost the same from 0.625 at the wellbore block to 0.58 at a distance from the well. The permeabilities from 74.6 md to 82.6 md corresponding to this range of saturations can be compared with the calculated permeabilities from well tests (see Column (9) of Table 5.5), which are about 80 md in every run. Thus, it is reasonable that the calculated permeability from well tests should reflect the permeability of a high steam saturation zone around the well.

It is expected that the comparison of the permeability from well testing with that at the average steam saturation would be more favorable, if the steam swept zone is very large. In such a case, the contribution of a few blocks of small steam saturations along the front will be insignificant, with a large area of high steam saturations behind the front.

From the results of two models, we could conclude that the estimated permeability of steam from pressure falloff tests is larger than the permeability at the volume-weighted average steam saturation behind the steam front for small swept volumes. The estimated permeability may reflect the effective permeability of a high steam saturation zone around the injection well. The estimated skin factor compares favorably with the input data of zero. The estimated swept volume is approximately close to the swept volume behind the steam front.

The discussion in this section suggests that because of high steam saturation gradients in the swept zone, the estimated permeability from a well test does not represent the effective permeability at the volume-weighted average steam saturation. Also, steam saturation gradients could affect the accuracy of the estimation of swept volumes. Therefore, more research is required to investigate the effect of saturation gradients (or mobility gradients) on the estimation of flow capacity and swept volumes.

5.3.3 Further Analysis of the Pressure Derivative Curve

Figure 5.14 shows the semilog pressure derivative data for Run 2. A conceptual explanation of the observed pressure derivative behavior follows. At the end of the infinite-acting radial flow regime (point A), the inner boundary between the steam zone and the hot water zone begins to effect. From A to B, there is a transition period. From B to C, the derivative data fall on the unit-slope line showing the inner boundary effect. Because the boundary is not a closed one, the regime from B to C lasts only for a short period of time. The flow in the hot water zone is shown from D to E. Because of the small hot water zone (about 10 ft in this run) and the effects of the inner boundary and the outer boundary between the hot water zone and the cold oil zone, the pressure derivative data from D to E does not exhibit a constant semilog pressure derivative representing the infinite-acting radial flow in the hot water zone. The data from E to F may be contributed by the effects of the outer boundary of the hot water zone and the cold oil zone.

The above analysis further supports the viewpoint in Section 5.3.1 that the swept volume deduced from pressure falloff analysis should include only the volume of steam zone.

It is also found that almost all the derivative data from A to F fall on one single straight line (shown in the dotted line) whose slope is less than one. This phenomenon is also found in Run 1 (shown in the dotted line in Fig. 5.11) and other runs. It may be caused by a small hot water zone and the low mobility contrasts at the boundaries, or other thermal effects in thermal well testing. A detailed investigation into this phenomenon may be warranted, especially if falloff tests conducted in the field also exhibit similar pressure derivative characteristics.

5.3.4 Gravity Segregation of Steam

An important feature of the steamflood process is the gravity segregation of steam. A 3D model is used for the study of the effect of gravity. In this section, two sets of results from areal models and 3D models are analyzed.

5.3.4.1 Effect of Location of Pressure Gauge

The areal model (Run 2) is first refined into 3 blocks in the vertical direction to obtain the 3D model I (Run 3). The pressure data at three different vertical blocks are different. These different pressure data are analyzed to estimate flow capacity and swept volumes. The results of Run 3 calculated from the pressure data at three vertical well blocks are shown in Table 5.7. Table 5.7 shows that the results calculated from the pressure data at different vertical blocks are different.

To investigate how the estimated permeabilities and volumes vary with the altitudes at which the pressure data are measured (the locations of pressure gauge, in practical well tests), another set of Runs 4 and 5 was tried. The gridblocks 7x7x1 in Run 4 are refined to 4 blocks in the vertical direction to obtain 7x7x4 gridblocks for Run 5. The results of Run 5 are shown in Table 5.7. It also shows that the results calculated from four different vertical blocks are different.

Investigation of the results of Runs 3 and 5 in Table 5.7 leads us to find that the permeabilities calculated from the pressure data at lower blocks are larger than those from the pressure data at the upper blocks, and the volumes calculated from the pressure data at the middle blocks (K = 2 in Run 3 and K = 3 in Run 5) are larger than any other volumes calculated from other blocks.

To confirm whether this result is typical in well tests, other cases were investigated including different gridblock models, different injection rates and times, and different reservoir parameters. It was found that although this result did not appear in every case, it did appear in most cases. Attempts were made to discover the reasons for this behavior. However, we were restricted by the available number of gridblocks in ISCOM 4.0. Fortunately, if a reservoir is not very thick like the cases of Runs 3 and 5, the estimated permeabilities and volumes from the pressure data at different altitudes are not too different. However, if a reservoir is very thick, it is expected that there may be significant differences. For comparison, we will use the results calculated from the pressure data at the middle vertical wellblock (K = 2).

This finding is important. If this result is typical of thermal well testing, the vertical location of pressure gauge in a well must be considered to interpret well testing data. Also, it is expected that locations of observation wells in interference well tests would affect the well testing interpretation. Therefore, this behavior is worthy of further investigation.

5.3.4.2 Effect of Gravity on the Estimation of Swept Volumes

When *Messner* and *Williams* (1982b) investigated the gravity segregation of steam, they converted a one-dimensional radial model 20x1x1 into a two-dimensional model 20x1x5, with each gridblock cell in the vertical direction having a thickness of 10 ft. In their numerical simulation study, the one-dimensional radial model gave a favorable volume estimation. However, they found that the estimated swept volume from the vertically refined model was smaller than that from the one-dimensional radial model. It seemed that the inclusion of gravity effect would lead to an underestimation of swept volumes. Therefore, they raised a question: "Is this underestimation indicative of a real-life phenomenon or a quirk exclusively inherent in the simulation model?"

TABLE 5.7 - EFFECT OF THE LOCATIONS OF PRESSURE GAUGE

Run No.	Gridblocks IxJxK	Pressure data from	k_e at $\overline{S_g}$ md	m_s psi/cycle	k_{ec} md	k_{ec}/k_e	s	V_s ft^3	m_c psi/hr	V_{sc} ft^3	$\frac{V_{sc}}{V_s}$
2	8x8x1	K = 1	52.6	11.371	81.1	1.54	0.45	217960	4.5116	241658	1.11
3	8x8x3	K = 3	58.9	12.335	75.4	1.28	0.26	211021	4.3782	248823	1.18
		K = 2		11.559	80.5	1.37	0.22		4.1594	261912	1.24
		K = 1		11.189	83.2	1.41	0.35		4.3770	248891	1.18
4	7x7x1	K = 1	64.1	11.803	80.4	1.25	0.38	185960	4.6833	230010	1.24
5	7x7x4	K = 4	61.9	12.977	72.3	1.17	0.38	204760	4.9755	214958	1.05
		K = 3		11.791	80.0	1.29	0.48		4.7819	223661	1.09
		K = 2		11.033	85.1	1.37	0.44		4.8418	220894	1.08
		K = 1		10.845	86.5	1.40	0.29		4.8584	220139	1.08

Comparing the results of Run 3 with those of Run 2 (see Table 5.7), we can see that the estimated swept volumes from the 3D model (Run 3) are larger than the estimated volume from the areal model (Run 2). However, when the 7x7x4 3D gridblock model (Run 5) is used, Table 5.7 shows that the estimated swept volume from the 3D model is smaller than that from the corresponding areal model 7x7x1 (Run 4).

From our results, we can see that whether the estimated volume from a vertically refined model is larger or smaller than that from the corresponding areal model depends on the gridblocks used in respective cases. Therefore, different results among models may be caused by the coarseness of gridblocks, and the underestimation phenomenon *Messner* and *Williams* (1982b) found is instead an inherent bias in the numerical model. Thus, it appears that the effect of gravity does not significantly influence the estimation of swept volumes.

5.3.5 Real Gas Analysis

The pressure data of Run 1 are analyzed using real gas well testing methods. Both the pressure squared method and the pseudo-pressure function method are used. The results are compared with those from the pressure analysis in Table 5.8.

TABLE 5.8 - COMPARISON OF RESULTS FROM THERE ANALYSIS METHODS (RUN1)

Analysis Method	k_e at $\overline{S}_g$ md	k_{ec} md	$\frac{k_{ec}}{k_e}$	s	V_s ft^3	V_{sc} ft^3	$\frac{V_{sc}}{V_s}$
p		80.2	1.29	0.85		278582	1.05
p^2	62.1	79.5	1.28	0.87	265904	276311	1.04
ψ_{ws}		78.6	1.27	1.34		273605	1.03

5.3.5.1 Pressure Squared Method

Figures 5.17 through 5.19 show the semilog derivative data, the semilog straight line and the Cartesian straight line of pressure squared data for Run 1, respectively. From Figure 5.17, infinite-acting flow lasts from Δt = 0.005 to 0.7 hours, pseudosteady state flow from Δt = 1.3 to 6 hours. These flow regime durations are close to those of pressure method. From Figures 5.18 and 5.19, m_s', p_{1hr}^2 and m_c' are 23148 psia^2/cycle, 1.1408x10^6 psia^2 and 8796.2 psia^2/hr, respectively. Using these data and Eqs. 4.14 through 4.16, the following results are obtained:

$$k_{ec} = 79.5 \text{ md}, \; k_{ec}/k_e = 1.28$$

$$s = 0.87$$

$$V_{sc} = 276311 \text{ ft}^3, \; V_{sc}/V_s = 1.04.$$

These results are very close to the results calculated from the pressure analysis method (see Table 5.8). The close agreement suggests that although the incorporation of the real gas law allows more accuracy in evaluating reservoir properties, the pressure analysis technique using an average steam formation volume factor probably suffices for most practical situations.

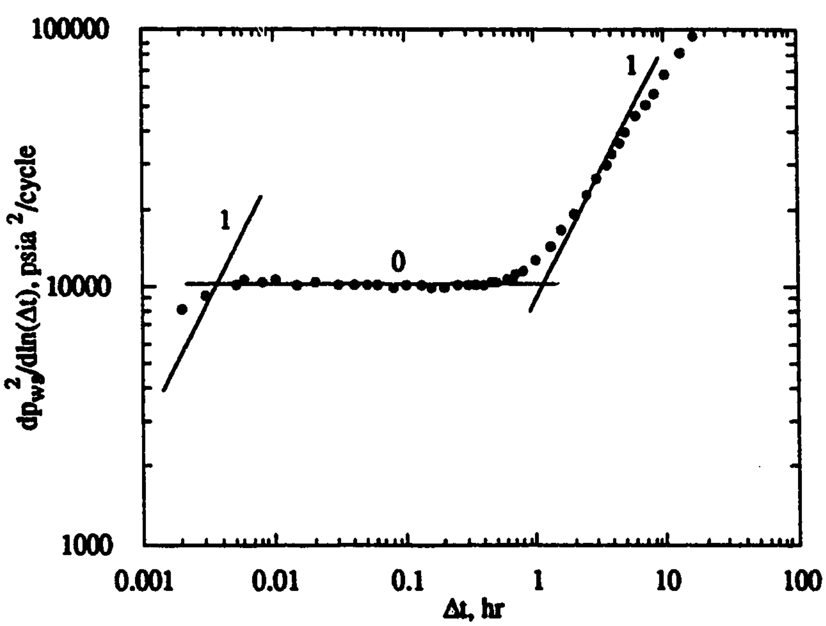

Fig. 5.17 - Semilog pressure squared derivatives for Run 1.

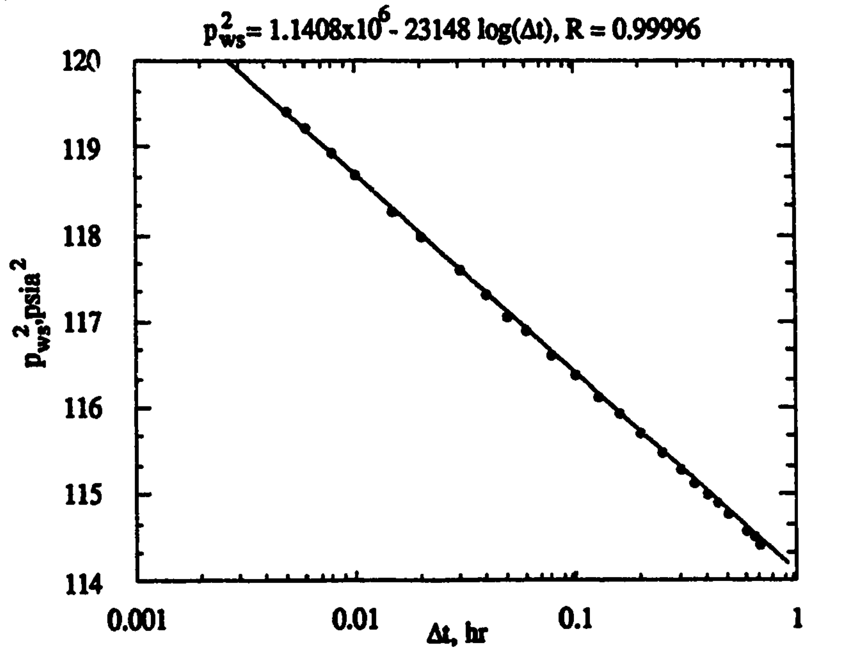

Fig. 5.18 - Semilog straight line of p_{ws}^2 vs. Δt for Run 1.

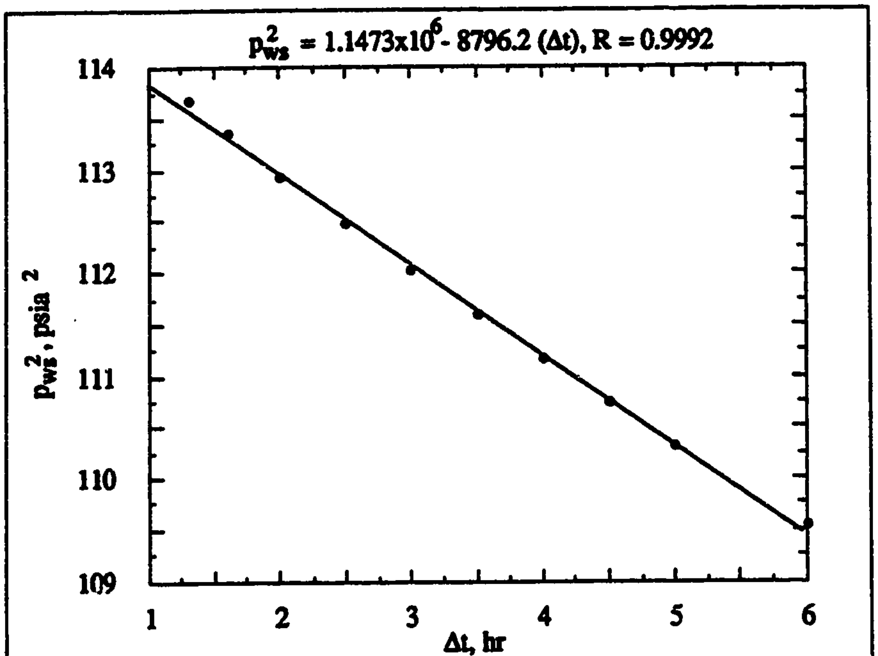

Fig. 5.19 - Cartesian straight line of p_{ws}^2 vs. Δt for Run 1

5.3.5.2 Pseudo-pressure Function Method

Figures 5.20 through 5.22 show the semilog derivative data, the semilog straight line and the Cartesian straight line of pseudo-pressure data for Run 1, respectively. The pseudo-pressure was calculated by the computer program (Appendix B). From Figure 5.20, infinite-acting flow lasts from Δt = 0.005 to 0.7 hours, pseudosteady state flow from Δt = 1.3 to 6 hours. These flow regime durations are close to those of pressure method and pressure squared method. From Figures 5.21 and 5.22, m_s'', Ψ_{1hr}, m_c'' are 1.5571×10^6 psia²/(cp·cycle), 7.16817×10^7 psia²/cp and 5.9062×10^6 psia²/(cp·hr), respectively. Using these data and Eq. 4.17 through 5.19, the following results are obtained:

$$k_{ec} = 78.6 \text{ md}, \ k_{ec}/k_e = 1.27$$

$$s = 1.34$$

$$V_{sc} = 273605 \text{ ft}^3,\ V_{sc}/V_s = 1.03.$$

Again, these results are close to the results from the pressure analysis method and the pressure squared analysis (see Table 5.8).

Table 5.8 shows that the pressure squared analysis and the pseudo-pressure analysis do not substantially improve calculation accuracy. This is because of the relatively small pressure changes common for steam pressure falloff testing. Therefore, the real gas analysis may not be necessary for most steam injection falloff tests.

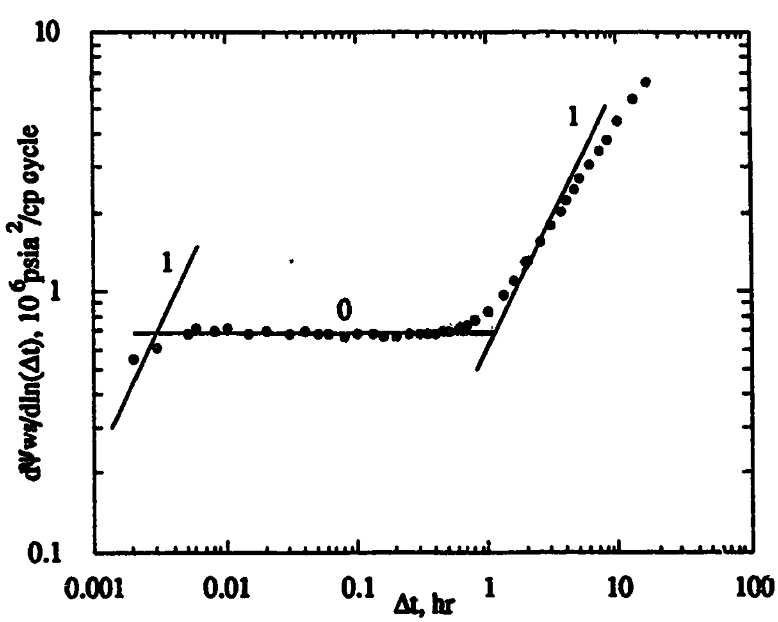

Fig. 5.20 - Semilog pseudopressure derivatives for Run 1.

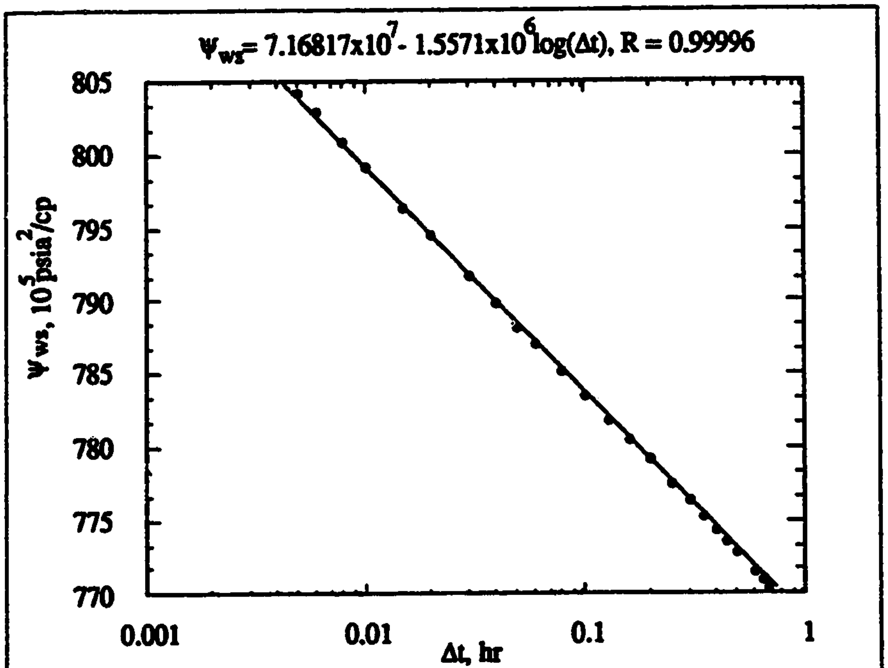

Fig. 5.21 - Semilog line of ψ_{ws} vs. Δt for Run 1.

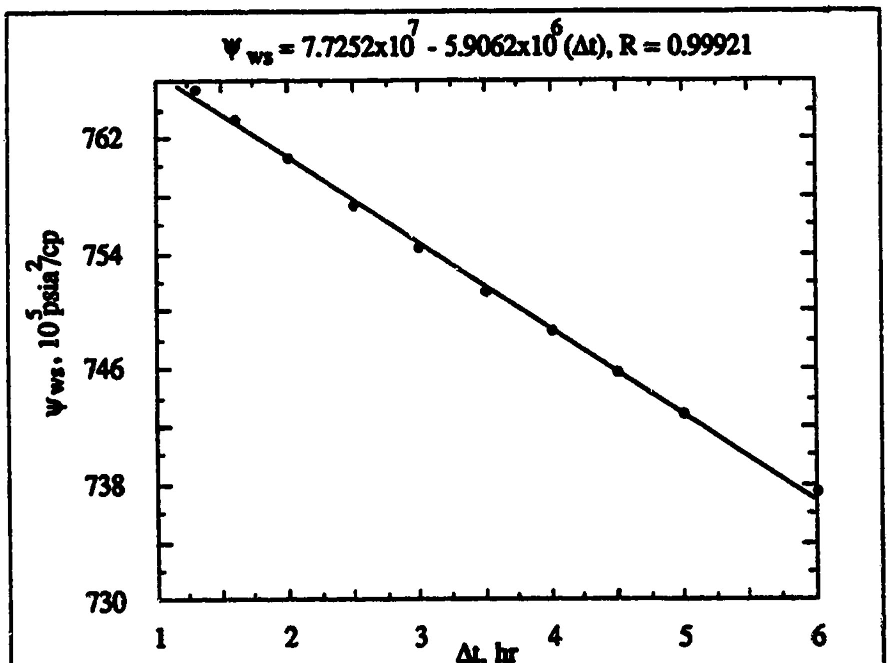

Fig. 5.22 - Cartesian line of ψ_{ws} vs. Δt for Run 1.

5.3.6 Effect of Dip

The effect of dip is investigated to evaluate the accuracy and applicability of thermal well testing in dipping reservoirs. Table 5.9 shows the results of dipping reservoirs of different dipping angles. 3D model I is used in Run 3. 3D model II is used in Runs 6 through 9. In all cases, injection rate is 500 STB/D, and injection duration is 30 days.

TABLE 5.9 - EFFECT OF DIP

Run No.	Dip degree	$\overline{S_g}$ [illegible]	k_e at $\overline{S_g}$ md	k_{ec} md	$\frac{k_{ec}}{k_e}$	s	V_s ft^3	V_{sc} ft^3	$\frac{V_{sc}}{V_s}$
3	0	48.5[illegible]	58.9	80.5	1.37	0.22	211021	261912	1.24
6	15	48.76	59.3	81.7	1.38	0.45	210488	258551	1.23
7	30	47.90	57.8	83.4	1.44	0.50	211821	263330	1.24
8	45	48.06	58.1	80.9	1.39	0.48	210488	259604	1.23
9	90	48.91	59.6	79.4	1.33	0.48	201960	231863	1.15

From Table 5.9, we can see that the calculated permeabilities are all about 40% higher than the permeabilities at volumetric average steam saturations. These results are in agreement with those from non-dipping reservoirs.

Table 5.9 shows us that the estimated permeabilities are very close to each other for different dipping angles. Permeability is calculated from infinite-acting flow data. Whenever infinite-acting flow proceeds, different dipping angles only result in different gravity effect. During steam falloff tests, the flow is dominated by steam phase only. The gravity would not be significant (see Sections 5.3.4.2 and 5.3.8). Therefore, the dipping angles would not affect the estimation of permeability.

Table 5.9 also shows us that the calculated swept volumes and the ratios of the calculated swept volumes to the respective simulation volumes are close to each other. The dipping angles do not affect the estimation of swept volumes either. This is consistent with the principle of material balance, on which our method to estimate swept volumes is based. The principle of material balance is not related to dipping angles.

Although dipping angles do not affect the estimation of flow capacity and swept volumes, they do affect the shapes of swept zones (see Figure 5.23). Due to long injection duration before falloff tests, sufficient time is available for steam to segregate. Because different dipping angles result in different gravity segregation, the shapes of swept zones are different.

In our model, a well will become a horizontal well if the dipping angle is 90^o. The results of Run 9 is also shown in Table 5.9. In this case, the dipping angle is 90^o. The results show that the calculated permeability of 79.4 md is higher than the permeability of 59.6 md at the average steam saturation of 0.4891. The calculated swept volume of 231,863 ft^3 is approximately equal to the simulation swept volume of 201,960 ft^3. This finding is the same as that obtained from non-dipping and dipping reservoirs. Thus, it seems that thermal well testing method is applicable for horizontal wells (see also *Issaka* , 1991).

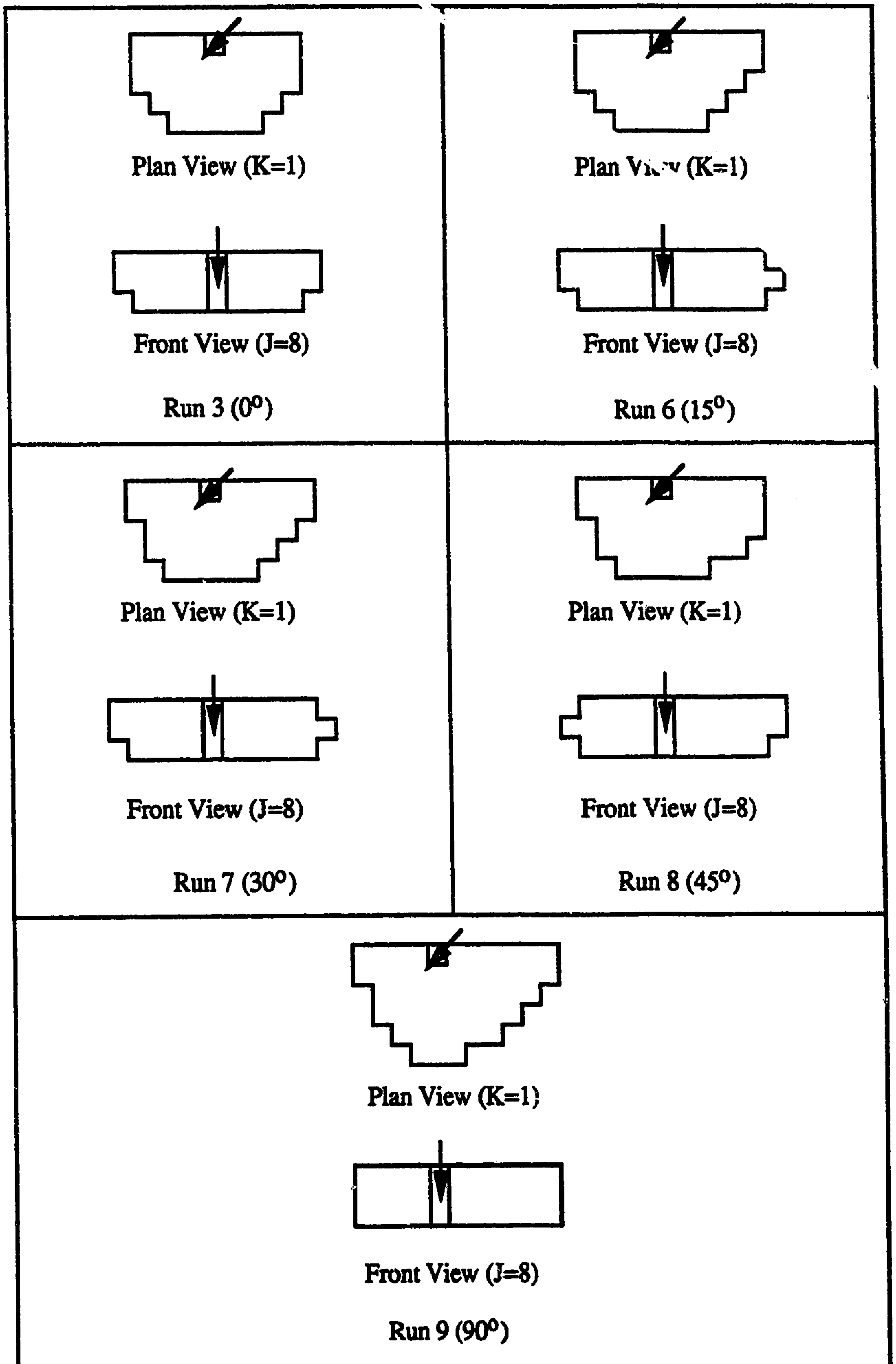

Fig. 5.23 - Shapes of swept zones for Run 3 and Runs 6 through 9.

5.3.7 Effect of Shapes of Swept Zones

Figure 5.23 shows the front locations in Run 3 and Run 6 through 9 at the instant of shut-in. The shapes of swept zones in these runs are quite different. However, Table 5.9 shows that almost the same results for permeability and swept volume estimation are obtained. Therefore, irregular shapes of the swept zones do not have a significant effect on the estimation of flow capacity and swept volume.

The shapes of swept zones do not affect the permeability estimation. This is because the calculated permeability from well tests reflects the flow before pressure response reaches the front. Section 5.3.2 demonstrated that the calculated permeability from a well test reflects the effective permeability within a high steam saturation zone. The high steam saturation distributions for each run are similar. They are not affected by the front shapes. The irregular shapes of swept zones are caused by the mobility difference in all directions. Figure 5.24 shows the vertical steam saturation and total mobility profile at J = 8 for Run 3. It shows that the front at K = 1 is nearer to the well than that at K = 2. It also shows that the steam saturations or the mobilities at K = 1 are lower than those at K = 2. In this way, steam will flow slower at K = 1 than at K = 2. It probably reaches the fronts at almost the same time. Thus, the irregular shapes of swept volumes would not significantly affect the estimation of swept volumes. Another viewpoint is that the calculation using the concept of pseudosteady state is a material balance calculation. This means that the pore volume of the swept region determined from the Cartesian graph of pressure versus time is actually independent of the geometry of the swept zone (*Eggenschwiler et al.*, 1980).

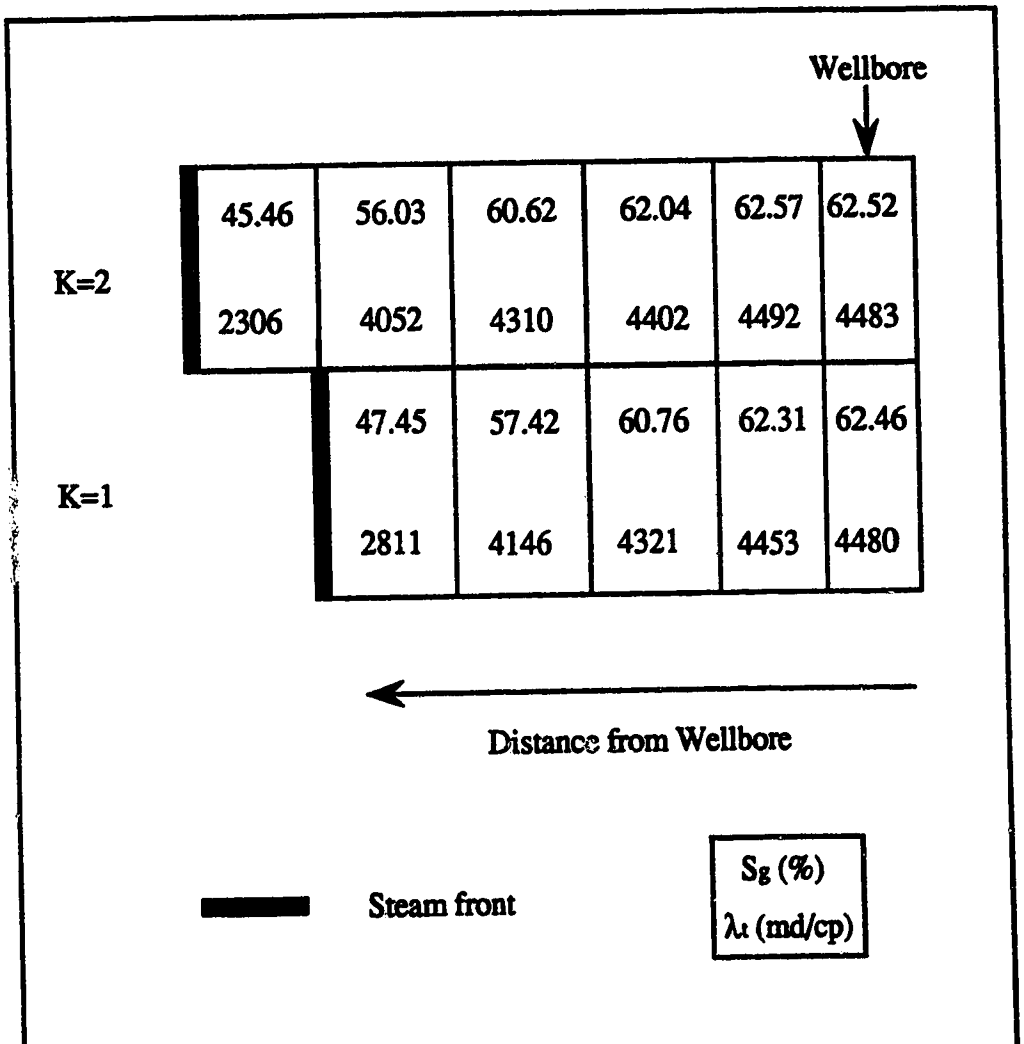

Fig. 5.24 - Total mobility and steam saturation distribution for Run 3 (J = 8).

5.3.8 Effect of Permeability Anisotropy

A higher permeability in one direction can cause more fluid flux in that direction, if all other conditions are the same. It is expected that more steam will move toward the top of the formation showing more obvious gravity effect, if the vertical absolute permeability is higher. Section 5.3.7 showed that the directionally variational permeabilities on the flow plane caused significant irregularity of front shapes of swept zones. This leads us to investigate the effect of anisotropy in permeability. The results of Runs 10 and 11 are compared with those of Run 3. In Runs 10 and 11, all other parameters and simulation conditions are the same as those in Run 3, except that k_K in Run 10 is 700 md, and k_J in Run 11 is 500 md.

Table 5.10 shows the directional permeabilities and results of Runs 3, 10 and 11. The effective absolute permeability is assigned the geometric mean of the permeabilities in the two directions normal to the well in the well model of ISCOM 4.0. In these runs, $\bar{k}$ are the square roots of the products of k_I and k_J, which are 700 md, 700 md and 592 md for Runs 3, 10 and 11, respectively. Although the absolute permeabilities and the effective permeabilities at $\bar{S}_g$ are different, the ratios of the estimated permeabilities from well testing data to the corresponding effective permeabilities are similar. Although there are permeability differences between these runs, the simulation volumes and estimated volumes are similar in each case. The ratios of the estimated volumes to the simulation volumes are almost the same. In any case, the estimated skin can be compares favorably with zero. Therefore, the permeability anisotropy does not affect the validity of estimation of k, s and V_s.

In Run 10, k_K is 700 md, ten times larger than that in Run 3. Compared with Run 3, more steam moves to the formation top, as shown in Figure 5.25. This phenomenon is caused by the higher permeability in the vertical direction k_K, and thus, greater effect of gravity.

TABLE 5.10 - EFFECT OF PERMEABILITY ANISOTROPY

Run No.	Dip	k_I md	k_J md	k_K md	$\bar{k}$ md	$\overline{S}_g$ %	k_e at $\overline{S}_g$ md	k_{ec} md	$\frac{k_{ec}}{k_e}$	s	V_s ft^3	V_{sc} ft^3	$\frac{V_{sc}}{V_s}$
3	0^0	700	700	70	700	48.54	58.9	80.5	1.37	0.22	211021	261912	1.24
10	0^0	700	700	700	700	50.71	62.8	81.4	1.30	0.45	196622	241845	1.23
11	0^0	700	500	70	592	49.26	50.9	68.1	1.34	0.46	204622	254069	1.24

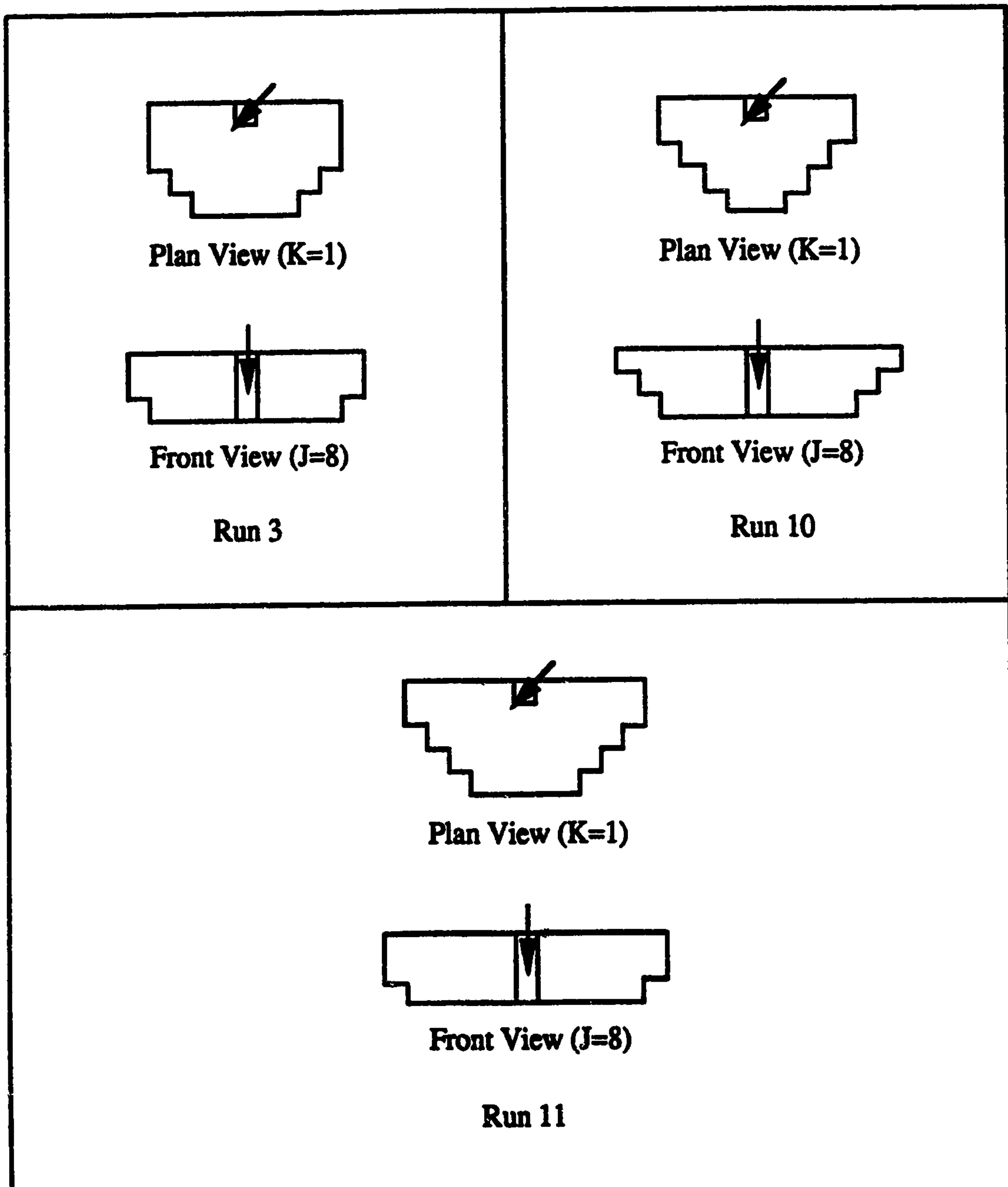

Fig. 5.25 - Effect of permeability anisotropy on the shapes of swept zones.

Therefore, permeability anisotropy, or equivalently, the effect of gravity does not significantly influence the estimation of parameters, such as k, s and Vs.

Figure 5.25 shows the irregular shapes of swept zones for Run 3, 10 and 11 caused by permeability anisotropy. Table 5.10 shows that the similar estimates have been obtained for the three runs. This further supports our conclusion that the irregular front shapes of swept zones do not have a significant effect on the estimation of flow capacity and swept volume (see Section 5.3.7).

5.3.9 Results of Ideal Gas Analysis

To the best of our knowledge, the preceding investigators used the values of some steam properties published in the literature. The published values of steam properties are not necessarily the same as those evaluated in simulators. This may lead to discrepancies in calculations. In our study, the values of steam properties in calculations are taken from the input and output files of the simulator ISCOM 4.0.

Investigation of the calculation Eqs. 4.1, 4.3, 4.5 and 4.7 leads us to find that the specific volume of steam ϑ_s is an important parameter in computing k_e and V_s. Approximately, k_e is directly proportional to ϑ_s, and V_s is inversely proportional to ϑ_s. Since ϑ_s is proportional to steam compressibility factor z (Eq. 4.8), the values of z are very important. This leads us to carry out ideal gas analysis. For an ideal gas, $z = 1$, the results will not be influenced by the possible miscalculation of ϑ_s or z. It was expected that ideal gas analysis would yield more reliable estimation. In our study, we set $z = 1.0$ for Runs 1* through 3* and Runs 6* through 9*. Runs 1* through 3* and Runs 6* through 9* correspond to Runs 1 through 3 and Runs 6 through 9, respectively. The results are shown in Table 5.5. Table 5.5 shows that the ratios of the calculated permeabilities to the effective permeabilities at average saturations in ideal gas cases are close to those in real gas cases. The ratios of the calculated swept volumes to the simulation volumes in ideal gas cases seem to be about 20% lower than those for real gas cases. All the volume ratios for ideal gas cases are close to 1.0, demonstrating more favorable results.

The fact that the results in ideal gas cases are close to the results in real gas cases confirms our results in this study. It also further verifies the validity of the thermal well testing method.

CHAPTER 6

DISCUSSION ABOUT THE *STANISLAV ET AL.* APPROACH

Messner and *Williams* (1982a) conducted an investigation of steam injection well testing. Their test data were analyzed with *Eggenschwiler et al.*'s theory (1979) and *Walsh et al.*'s analytical procedure (1981). In an extension of their study (1982b), a numerical simulation study was performed. They concluded that incorporation of the steam override effect in a numerical simulation model yielded results that suggested pressure falloff testing may lead to an underestimation of the swept pore volume. According to our study (Section 5.3.4.2), their underestimation of the swept pore volume was an inherent bias in the numerical model and was not representative of actual field results.

Messner and *Williams'* underestimation of the swept volume (1982b) may have led *Stanislav et al.* (1987 and 1989) to make studies to improve estimation of a swept volume based on the pseudosteady state concept by considering the effect of heat losses on pressure behavior during the falloff testing period.

6.1 The *Stanislav et al.* Approach

Based on the material balance with the inclusion of the steam-condensation effect, which is induced by heat losses to the surrounding rocks, they derived the general differential equation as follows:

$$\frac{1}{r}\frac{\partial}{\partial r}(r\frac{\partial p}{\partial r}) = \frac{\phi c_t}{0.000264\lambda_t}(\frac{\partial p}{\partial t}) + \frac{(F_\rho - 1)G}{0.000264\lambda_t} \quad . \tag{6.1}$$

The rate of condensation per unit volume, G, is calculated by the *Yortsos* lower-bound expression (1984):

$$G = \frac{2\, k_h\, (T_s - T_i)}{\sqrt{24\pi\, \alpha\, t}\, L_v \rho_w\, h} \quad . \tag{6.2}$$

Using the following dimensionless quantities:

$$p_D = \frac{k\, h\, (p_i - p)}{141.2 qB\mu} \quad , \tag{6.3}$$

$$r_D = \frac{r}{r_w} \quad , \tag{6.4}$$

$$t_D = \frac{0.000264kt}{\phi\mu c_t r_w^2} \quad , \tag{6.5}$$

$$G_D = \frac{h r_w^2 G}{(0.000264)(141.2)qB} \quad , \tag{6.6}$$

Eq. 6.1 can be transformed into a dimensionless form:

$$\frac{1}{r_D}\frac{\partial}{\partial r_D}(r_D \frac{\partial p_D}{\partial r_D}) = \frac{\partial p_D}{\partial t_D} - G_D\,(F_\rho - 1) \quad . \tag{6.7}$$

For Eq. 6.7, the short-time approximation is:

$$p_{wD} = \frac{1}{2}(\ln t_D + 0.81) + 2\beta\sqrt{t_D} + s \quad , \tag{6.8}$$

and the pseudosteady state approximation is:

$$p_{wD} = \frac{1}{2}\ln(\frac{2.24A}{C_A r_w^2}) + 2\pi t_D (r_w^2/A) + 2\beta\sqrt{t_D} + s \quad . \tag{6.9}$$

The dimensional equivalents of Eqs. 6.8 and 6.9 can be written as:

$$\Delta p - (\gamma/2)\ln t = 2\beta\gamma\delta^{1/2} t^{1/2} + (\gamma/2)\ln(\delta + 0.81 + 2s) \quad , \tag{6.10}$$

and

$$\Delta p - 2\beta\gamma\delta^{1/2} t^{1/2} = 2\pi\gamma\delta(r_w^2/A)t + (\gamma/2)\ln(\frac{2.24A}{C_A r_w^2}) + \gamma s \quad , \tag{6.11}$$

respectively, where

$$\beta = 0.1\frac{(F_p - 1)k_h(T_s - T_i)r_w}{L_v\rho_w qB}\sqrt{\frac{k}{\alpha\phi\mu c_t}} \quad , \tag{6.12}$$

$$\gamma = \frac{141.2qB\mu}{kh} \quad , \tag{6.13}$$

$$\delta = \frac{2.64 \times 10^{-4}k}{\phi\mu c_t r_w^2} \quad . \tag{6.14}$$

Based on Eq. 6.10, a plot of $\Delta p - (\gamma/2)\ln t$ vs. $\sqrt{t}$ should yield a straight line with a slope

$$m = 2\beta\gamma\delta^{1/2} \quad . \tag{6.15}$$

From Eq. 6.15, the coefficient β can be readily obtained. The skin factor can be computed from:

$$s = \left[\Delta p^{(1)}/\gamma\right] - 2\beta\delta^{1/2} - (1/2)\ln(\delta + 0.81) \quad , \tag{6.16}$$

where $\Delta p^{(1)}$ is the pressure difference at the test time of 1 hour, determined from the linear plot of $\Delta p - (\gamma/2)\ln t$ vs. $\sqrt{t}$.

In their presented paper (1987), *Stanislav et al.* demonstrated, from Eq. 6.10, the plot of $(p_i - p)$ vs. $\ln(t\, e^{t^{1/2}})$ yielded a straight line having a slope

$$m = \frac{141.2 qB\mu}{kh} \quad , \tag{6.17}$$

which, they thought, could be used to estimate flow capacity of the inner region (swept zone).

However, from the viewpoint of mathematics, from Eq. 6.10, the plot of $(p_i - p)$ vs. $\ln(t\, e^{4\beta\delta^{1/2} t^{1/2}})$ should yield a straight line, instead of the plot of $(p_i - p)$ vs. $\ln(t\, e^{t^{1/2}})$.

From Eq. 6.11, a plot of $(\Delta p - 2\beta\gamma\delta^{1/2} t^{1/2})$ vs. t should yield a straight line with a slope

$$m^* = 2\pi\gamma\delta\,(r_w^2/A) \quad , \tag{6.18}$$

which is equivalent to the following expression:

$$m^* = \frac{(5.615)qB}{(24)Ah\phi c_t} \quad . \tag{6.19}$$

Eq. 6.18 or Eq. 6.19 could be solved for the swept volume.

Before the above approach can be used, γ and δ must be calculated. From Eqs. 6.13 and 6.14, the permeability k must be known. However, k is not known before well tests in practice.

6.2 Examples of Application and Discussion

Three examples are used to discuss the approach described above. The data of Example 1 are taken from *Stanislav et al.*'s example (1989). The data of Examples 2 and 3 are taken from Runs 1 and 2, respectively, in Chapter 5.

Example 1

In this example, *Stanislav et al.*'s data are analyzed using the above approach to find what problems will be met in practical application.

Using *Stanislav et al.*'s data, β can be calculated directly from Eq. 6.12:

$$\beta = (0.1)\frac{(12.6 - 1)(34)(480)(0.6)}{(624.1)(45.2)(21,658)} \times \sqrt{\frac{(150)}{(0.83)(0.25)(0.016)(0.314)}}$$

$$= 0.071.$$

But β estimated from the *Stanislav et al.* approach (i.e., Eq. 6.15) was 0.5 (*Stanislav et al.*, 1989), 70 times larger than 0.071.

Figure 6.1 is the plot of $\Delta p - (\gamma/2)\ln(\Delta t)$ vs. $\Delta t^{1/2}$, where γ is equal to 8.15 psi calculated from Eq. 6.13. From Figure 6.1, we can see that all data points during the entire testing period cover the same straight line. This makes it impossible to identify different flow regimes. If the slope of this straight line is used, the β estimated from Eq. 6.15 is 0.52.

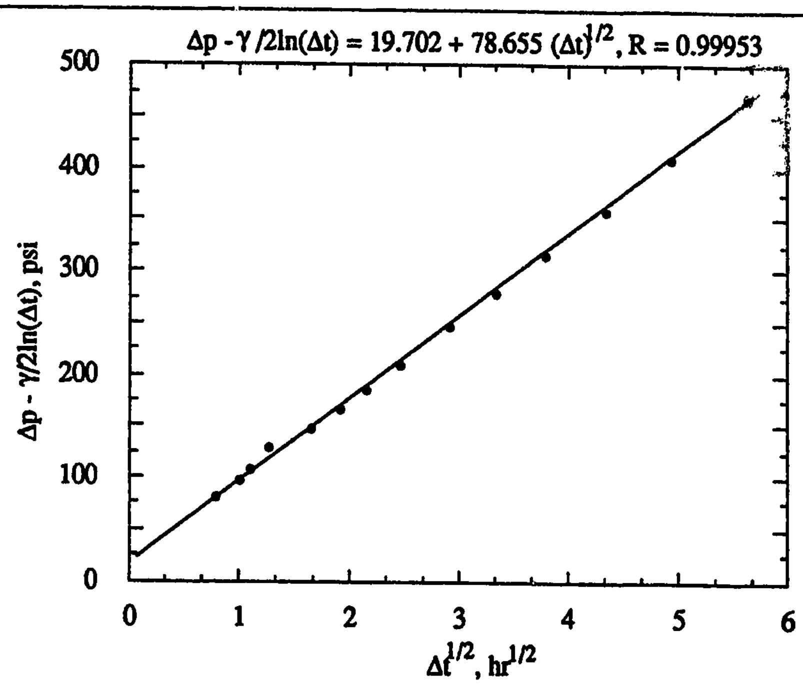

Fig. 6.1 - Plot of $\Delta p - \gamma/2\ln(\Delta t)$ vs. $\Delta t^{1/2}$ of *Stanislav et al.*'s data (1989).

Figure 6.2 is the plot of $\Delta p - 2\beta\gamma\delta^{1/2}\Delta t^{1/2}$ vs. Δt. Except a few data points during the early time period, most data points fall on the same Cartesian straight line showing a long pseudosteady state period. As pointed out in Section 5.3.3, it is not practical to have a long pseudosteady state.

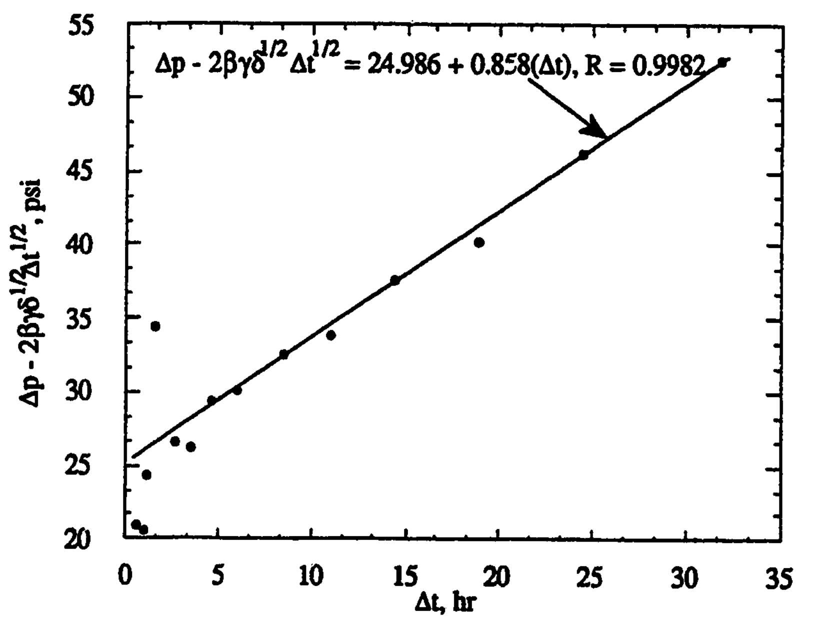

Fig. 6.2 - Plot of $\Delta p - 2\beta\gamma\delta^{1/2}\Delta t^{1/2}$ vs. Δt of *Stanislav et al.*'s data (1989).

Example 2

Figure 6.3 shows the data of Run 1 when the values of γ are equal to 1.06 psi, 9.3 psi and 12.0 psi, calculated from Eq. 6.13 when k is substituted with the absolute permeability of 700 md, the calculated effective permeability of 80.2 md from the semilog analysis of well test data, and the effective permeability of 62.1 md at the average steam saturation, respectively. when $\gamma = 9.3$ psi, the curve is almost a horizontal line before $\Delta t = 1$ hour. The calculated β from the slope of this line would be almost zero or a very small value. When $\gamma = 1.06$ psi or 12.0 psi, we could not obtain straight lines. When $\gamma = 12.0$ psi, the curve is concave. The slopes before Δt = 1 hour are negative. The calculated β would be negative, which is not a reasonable phenomenon.

Figure 6.3 shows us that the early-time data are so sensitive to the values of γ that impractical β could be obtained in some cases. Before Δt = 1 hour, ln(Δt) is negative. When Δt is very small, - $\gamma/2$ ln(Δt) could be very large. If Δp is not very large, which is typical of steam falloff tests, the pressure function Δp - $\gamma/2\ln(\Delta t)$ could be governed by the logarithmic term. In this case, the pressure function could decrease as time increases, as happened when γ = 12.0 psi in Figure 6.3, which leads to impractical (negative) β estimation.

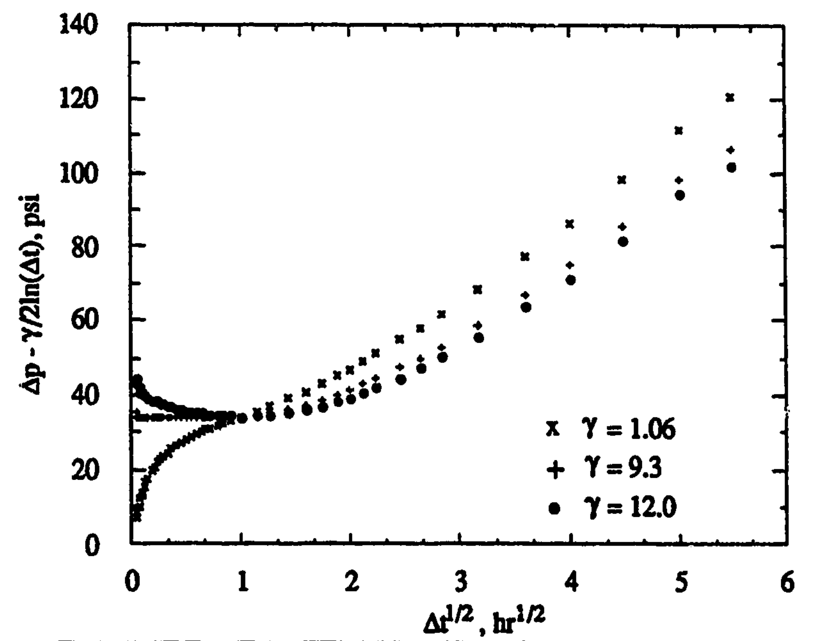

Fig. 6.3 - Plot of $\Delta p - \gamma/2\ln(\Delta t)$ vs. $\Delta t^{1/2}$ of falloff data from Run 1.

The plot of $\Delta p - 2\beta\gamma\delta^{1/2}\Delta t^{1/2}$ vs. Δt is shown in Figure 6.4. When generating this plot, the values of β, γ and δ must be known. Because β could not be obtained from the early-time well testing data, the value equal to 0.03227 estimated from Eq. 6.12 is used. γ of 9.3 psi and δ of 6106.2 hr^{-1} are obtained from Eqs. 6.13 and 6.14, respectively. Figure 6.4 shows that the magnitudes of the pressure function $\Delta p - 2\beta\gamma\delta^{1/2}\Delta t^{1/2}$ first increase, then decrease with time increasing, and soon become negative. Thus, the slopes are negative. If the negative slopes are used to calculate swept volumes, the volumes would be negative.

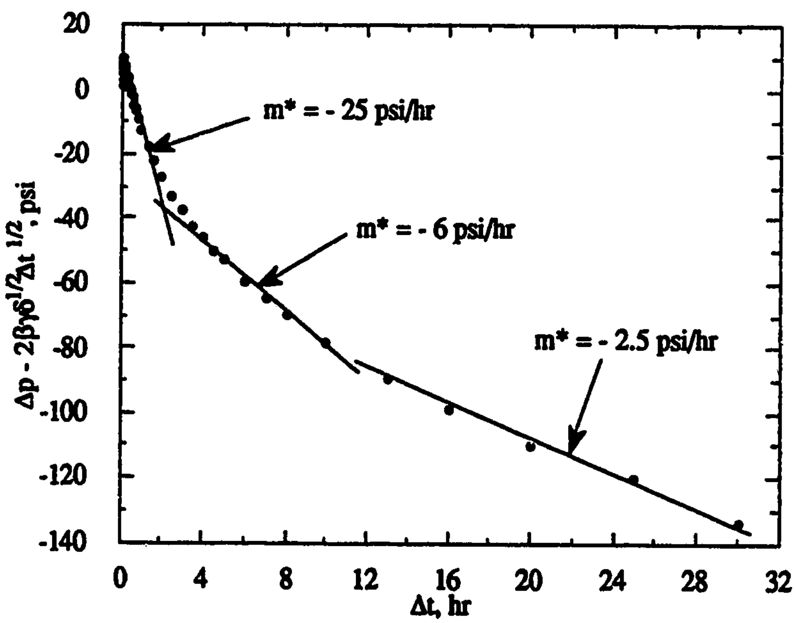

Fig. 6.4 - Plot of $\Delta p - 2\beta\gamma\delta^{1/2}\Delta t^{1/2}$ vs. Δt of falloff data from Run 1.

Example 3

Fig. 6.5 is the plot of $\Delta p - \gamma/2\ln(\Delta t)$ vs. $\Delta t^{1/2}$ of falloff data from Run 2, where γ = 9.88 psi obtained from Eq. 6.13 is used. In Fig. 6.5, the two straight lines are generated. The first straight line of the early-time data should be used to calculate β and s, whose slope is 0.92 psi/hr$^{1/2}$, $\Delta p^{(1)}$ is 41.6 psi. Using this slope and $\Delta p^{(1)}$, the calculated β and s from Eqs. 6.15 and 6.16 are 0.00133 and 0.53, respectively. However, the calculated β from Eq. 6.12 is 0.03, about 23 times *higher* than the β of 0.00133 estimated from the falloff testing approach. However, the opposite phenomenon happened in Example 1, in which the calculated β of 0.071 from Eq. 6.12 is about 70 times *lower* than that β of 0.5 estimated from the falloff testing approach.

The second straight line is drawn to show the importance to correctly identify flow regimes. Although the straight line is obtained from $\Delta t^{1/2}$ equal to 1.8 to 4.5 hr$^{1/2}$, the data during this period should not be used to calculate β and s.

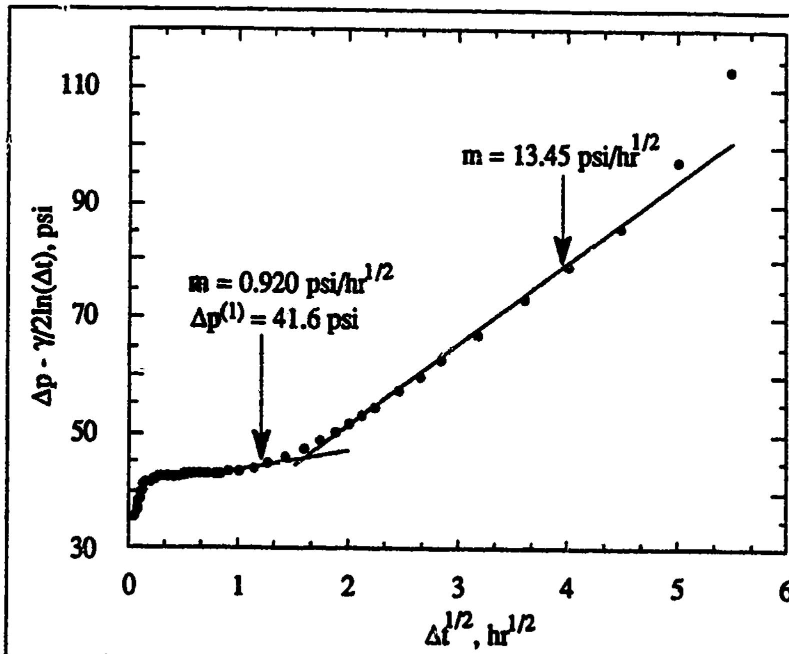

Fig. 6.5 - Plot of $\Delta p - \gamma/2\ln(\Delta t)$ vs. $\Delta t^{1/2}$ of falloff data from Run 2.

Figure 6.6 is the plot of $\Delta p - 2\beta\gamma\delta^{1/2}\Delta t^{1/2}$ vs. Δt for Run 2, in which β is taken to be 0.00133 estimated from the above falloff testing approach. If the slope of the straight line m^* of 4.0336 psi/hr is used, the calculated volume from Eq. 6.19 is 270,295 ft^3. The simulation volume of Run 2 is 217,960 ft^3. The ratio of the calculated volume to the simulation volume is 1.24. The ratio of the calculated volume from the conventional well testing method to the simulation volume is 1.11 (see Table 5.5). This example does not show that the *Stanislav et al.* approach improves the estimation of swept volumes.

Again, if the β value of 0.030 estimated from Eq. 6.12 is used to plot $\Delta p - 2\beta\gamma\delta^{1/2}\Delta t^{1/2}$ vs. Δt, instead of the β of 0.00133 estimated from the early-time well testing data, a negative swept volumes will result.

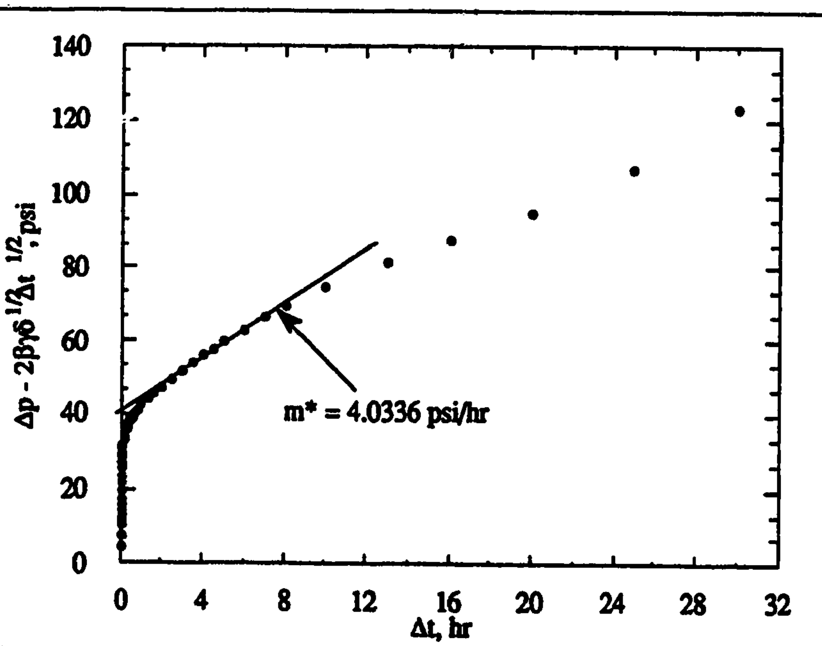

Fig. 6.6 - Plot of $\Delta p - 2\beta\gamma\delta^{1/2}\Delta t^{1/2}$ vs. Δt of falloff data from Run 2.

6.3 Further Discussion

In Examples 2 and 3, it was found that if the values of β calculated from Eq. 6.12 were used, the generated pressure function $\Delta p - 2\beta\gamma\delta^{1/2}\Delta t^{1/2}$ and the slope m^* were negative. Consequently, the estimated volume would be negative. This might be caused by the large value of the product $2\beta\gamma\delta^{1/2}\Delta t^{1/2}$. If the product $2\beta\gamma\delta^{1/2}\Delta t^{1/2}$ is large and Δp is small, both the pressure function and the slope m^* could be negative. The large product $2\beta\gamma\delta^{1/2}\Delta t^{1/2}$ may be caused by the overestimation of β. Because γ and δ are the two conventional definition terms, only β in the product is related with the steam condensation term G. The rate of condensation per unit volume, G, was developed by *Yortsos* (1984) for steam *injection* processes. Whether it could be used to calculate steam condensation effect during *falloff* tests is worthy of investigation. Furthermore, the results of Examples 1 and 3 showed us that the calculated β from Eq. 6.12 is much higher or lower than that estimated from well test data, depending on cases. Therefore, whether Eq. 6.12 could be used to calculate β is open to question.

The pressure function $\Delta p - 2\beta\gamma\delta^{1/2}\Delta t^{1/2}$ could be further investigated. If we assume γ = 10 psi, and δ =100 1/hr, which are typical values, β = 1.0, which is not high, and Δt = 4 hours, $2\beta\gamma\delta^{1/2}\Delta t^{1/2}$ will be 400 psi. Thus, Δp must be at least 400 psi at Δt = 4 hours to make the pressure function values positive. Generally, the pressure drop at the shut-in time of 4 hours could not reach as high as 400 psi in practical steam injection falloff tests.

To guarantee that a positive swept volume would be estimated, the slope $m^* = 2\pi\gamma\delta(r_w^2/A)$ must be greater than zero. From Eq. 6.11, the following condition must be satisfied:

$$\frac{d(\Delta p)}{d(\Delta t)} > \beta\gamma\delta^{1/2}\Delta t^{-1/2} \quad , \tag{6.20}$$

for late-time falloff data.

Similarly, to guarantee that a positive β would be estimated, from Eq. 10, the pressure function Δp - $\gamma/2\ln(\Delta t)$ must satisfy the following condition:

$$\frac{d(\Delta p)}{d(\Delta t)} > \frac{\gamma}{2(\Delta t)} \quad , \tag{6.21}$$

for early-time falloff data, which is not readily satisfied before $\Delta t = 1$ hour.

In practical steam falloff tests, it will be difficult for all the above conditions to be satisfied, because of the typical small pressure changes during the testing period.

6.4 The Modified *Stanislav et al.* Approach

The *Stanislav et al.* approach (1989) requires that the formation permeability be known to estimate the β coefficient of steam condensation, and the correct β must be estimated to obtain reasonable swept volumes. Generally, the formation permeability is not known before well tests. In some cases, β may not be obtained for the lack of information. Therefore, the *Stanislav et al.* approach needs to be modified.

6.4.1 The Modified *Stanislav et al.* Approach

It is assumed that the product $2\beta\gamma\delta^{1/2}$ can be correctly estimated from available information. The product may be named the steam condensation constant, represented by C_G:

$$C_G = 2\beta\gamma\delta^{1/2} \quad , \tag{6.22}$$

or

$$C_G = \frac{0.46(F_\rho - 1)k_h(T_s - T_i)}{\alpha^{1/2}L_v\rho_w\phi c_t h} \quad . \tag{6.23}$$

Although β, γ and δ in the definition 6.22 are related to k, the term G itself is not related to the formation permeability. Furthermore, the term G is not even related to the wellbore radius and formation flow rate. With the correct C_G obtained, the *Stanislav et al.* approach can be modified for practical uses.

For early-time falloff data analysis, rearrangement of Eq. 6.10 suggests that the plot of $\Delta p - C_G(\Delta t)^{1/2}$ vs. $\log(\Delta t)$ will yield a straight line with a slope

$$m' = \frac{162.6qB\mu}{kh} \quad . \tag{6.24}$$

Eq. 6.24 can be used to estimate flow capacity. For small $(\Delta t)^{1/2}$, $\Delta p - C_G(\Delta t)^{1/2}$ should be positive.

The skin factor can be obtained from:

$$s = 1.1513\left((\frac{\Delta p^{(1)}}{m'}) - \log(\frac{k}{\phi\mu c_t r_w^2}) + 3.23\right) \quad , \tag{6.25}$$

where $\Delta p^{(1)}$ was the value of pressure function $\Delta p - C_G(\Delta t)^{1/2}$ at the testing time of 1 hour on the straight line on a graph of $\Delta p - C_G(\Delta t)^{1/2}$ vs. $\log(\Delta t)$.

Once the flow capacity is obtained, β can be estimated from:

$$\beta = \frac{C_G}{2\gamma\delta^{1/2}} \quad . \tag{6.26}$$

With this modified approach, the condition described by the inequality 6.21 is not necessary.

For the pseudosteady state data, the plot of Δp - C_G $(\Delta t)^{1/2}$ vs. Δt should yield a straight line with a slope

$$m^* = \frac{(5.615)qB}{(24)V\phi c_t} \quad . \qquad (6.27)$$

Eq. 6.27 can be solved for the swept volume directly, which is the same as the *Stanislav et al.* approach (1989).

Actually, even if C_G could not be estimated from available information, several guesses of C_G may be tried until the linear plots of Δp - C_G $(\Delta t)^{1/2}$ vs. log(Δt) for early-time falloff data and Δp - C_G $(\Delta t)^{1/2}$ vs. Δt for late-time falloff data are achieved. The fact that $C_G > 0$ and C_G must satisfy the following condition from Eq. 6.20 will help to guess C_G values:

$$C_G < (2)\frac{d\,(\Delta p)}{d\,(\Delta t)}(\Delta t)^{1/2} \quad . \qquad (6.28)$$

6.4.2 Example of Application

As discussed in Example 1 of Section 6.2, the data of this example are not typical of thermal well testing data, because the data showed a semilog straight line within the whole range of testing period and a Cartesian straight line for a long time. Because β was not obtained using the *Stanislav et al.* approach in Example 2 of Section 6.2, we cannot compare the results from the modified approach with those from the *Stanislav et al.* approach. Therefore, the pressure falloff data of Example 3 are analyzed to illustrate the application of the modified *Stanislav et al.* approach. The calculated minimum of the term

$2\frac{d(\Delta p)}{d(\Delta t)}\Delta t^{1/2}$ is 12.6. According to the inequality 6.28, the steam condensation constant C_G should be less than 12.6. C_G is guessed to be equal to 10, 5, 2.5, 1.0 and 0.5. For the individual C_G, the semilog derivative data of the pressure function $\Delta p - C_G \Delta t^{1/2}$ are shown in Figure 6.7. Figure 6.7 is used to decide which C_G can be chosen, so that the linear plots can be achieved. From Figure 6.7, when C_G is reduced to 1.0 or 0.5, the semilog derivative data approximately show a constant for the early-time falloff data and a unit slope line for the late-time falloff data. That means when C_G is less than 1.0, the linear plots on a semilog graph and a Cartesian graph can be achieved and the flow regimes can be identified. Thus, C_G equal to 1.0 is chosen in this example. The corresponding semilog graph and Cartesian graph are shown in Figures 6.8 and 6.9, respectively. Using the slopes of the two graphs, the calculated results are shown in Table 6.1. For comparison, the results from the conventional well testing approach and the *Stanislav et al.* approach are also shown. Table 6.1 shows that the results from the modified approach are close to those from the *Stanislav et al.* approach. However, for the *Stanislav et al.* approach, the permeability must be known before the application of the approach. The modified approach can now be used to estimate permeability.

When C_G equals zero, the modified approach becomes the conventional well testing approach. The advantage of the modified approach over the conventional approach is that it can consider steam condensation effect.

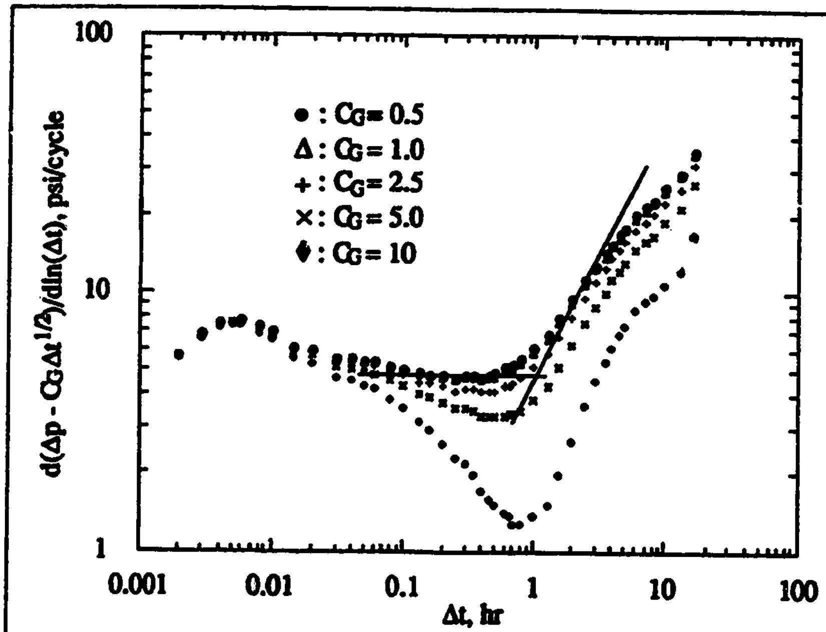

Fig. 6.7 - Semilog pressure function derivatives for Run 2.

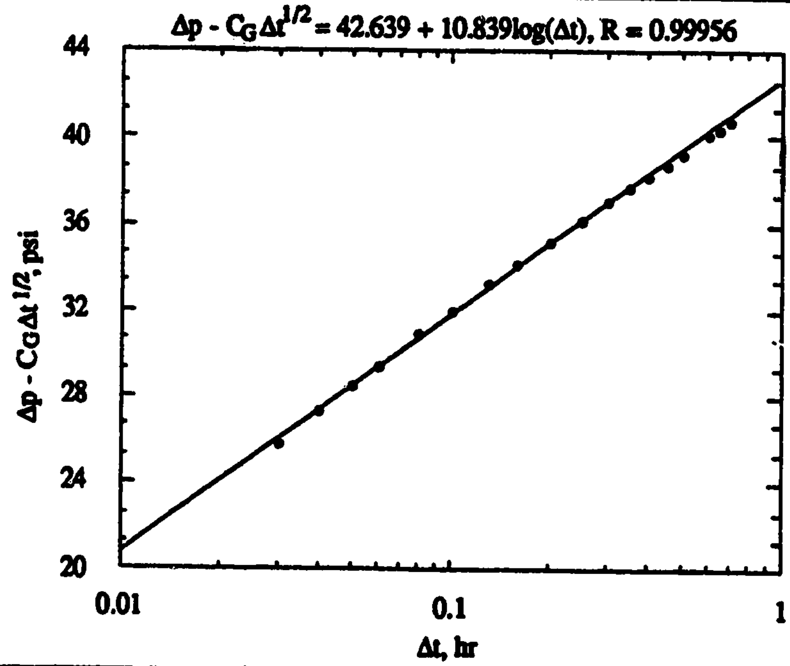

Fig. 6.8 - Semilog graph of $\Delta p - C_G\Delta t^{1/2}$ vs. Δt for Run 2.

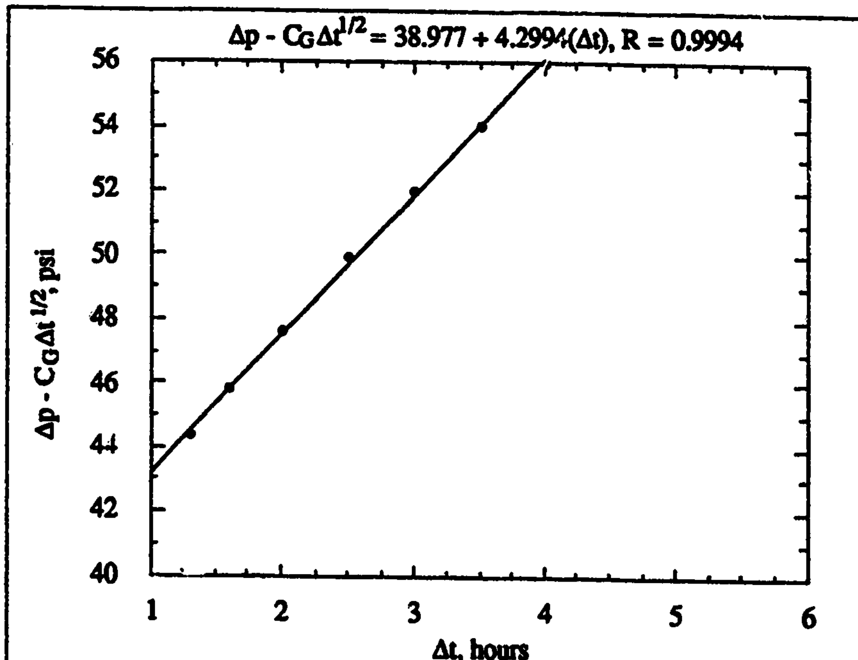

Fig. 6.9 - Cartesian graph of $\Delta p - C_G \Delta t^{1/2}$ vs. Δt (Run 2).

TABLE 6.1 - COMPARISON OF RESULTS FROM THREE WELL TESTING APPROACHES

Well Testing Approaches	k_e at $\overline{S_g}$ md	k_{ec} md	s	V_s ft^3	V_{sc} ft^3	β
Conventional	52.6	81.1	0.45	217960	241658	No
Stanislav *et al.*		No	0.53		270295	0.00133
The Modified		85.1	0.54		253585	0.00148

CHAPTER 7

CONCLUSIONS AND RECOMMENDATIONS

The main focus in this study has been on the estimation of effective permeability and swept volume from steam injection falloff testing data in non-dipping and dipping reservoirs. Thermal well testing with inclusion of steam condensation effect has been also discussed.

7.1 Conclusions

Based on our simulation study, the following conclusions may be drawn regarding the conventional approach of thermal well test analysis:

1. The estimated swept volume from falloff tests represents the volume of steam zone, and is equal to the swept volume behind the steam front to engineering accuracy.

2. The estimated permeability from falloff tests would not reflect the effective steam permeability at the volume-weighted average steam saturation behind the zero steam saturation front. Based on our results, the former is about 30% to 40% higher than the latter. The estimated permeability from well tests may reflect the effective permeability of a high steam saturation zone around the injection well.

3. The estimated skin factor compares favorably with the input data of zero.

4. The estimation of flow capacity and swept volumes depends on the vertical positions where pressure data are measured.

5. Because of the relatively small pressure changes common for steam pressure falloff testing, the pressure analysis technique should suffice from practical viewpoints, and the real gas analysis is unnecessary.

6. The formation dip affects the shapes of swept zones, but it does not affect the validity of estimation of flow capacity and swept volume from thermal well testing.

7. The irregular shapes of swept zones and permeability anisotropy do not have a significant effect on the estimation of flow capacity and swept volume.

From the discussion about thermal well testing with an inclusion of steam condensation effect, we conclude:

1. The applicability of the *Stanislav et al.* approach is limited by its application conditions in practical well tests. The modified approach proposed in this study can expand the applicability by removing these conditions.

7.2 Recommendations

Further investigation in thermal well testing should address:

1. the effect of steam saturation gradients (or mobility gradients) on the estimation of flow capacity and swept volume,

2. the effects of the vertical and areal positions where pressure data are measured on thermal well testing interpretation, and

3. the total compressibility for multiphase flow during steam injection process.

Further studies in the thermal well testing with an inclusion of steam-condensation effect should address:

1. the calculation of steam-condensation term β, especially during *falloff* tests, and

2. The magnitude of steam-condensation effect on thermal well testing interpretation.

REFERENCES

Abad, B.P.: "Unconventional Steamflood in a Layered-Dipping Reservoir: A Theoretical and Field Case Study, Temblor Formation, West Coalinga, Fresno County, California," paper SPE 11693 presented at the California Reg. Mtg. of SPE of AIME, Ventura, CA (March 23-25, 1983).

Abad, B.P. and Hensley, C.A.: "The Effect of Stratification, Fractures, and Dip on Steam Sweep Efficiency and Heat Requirements of Steamflood Operations," paper SPE 12748 presented at the California Reg. Mtg. of SPE of AIME, Long Beach, CA (April 11-13, 1984).

Agarwal, R.G.: "A New Method to Account for Producing Time Effects When Drawdown Type Curves Are Used to Analyze Pressure Buildup and Other Test Data," paper SPE 9289 presented at the 55th Annual Mtg. of SPE of AIME, Dallas, TX (Sept. 21-24, 1980).

Ambastha, A.K.: "Differentiation Algorithm," Selected Publications for Pet. E668, University of Alberta (1991).

Ambastha, A.K. and Kumar, M.: "Pressure Falloff Analysis for Steam Injection Wells in a Low-Permeability Reservoir with Steam-Induced Vertical Fractures," paper SPE 19788 presented at the 64th Annual Mtg. of SPE of AIME, San Antonio, TX (Oct. 8-11, 1989).

Ambastha, A.K. and Ramey H.J. Jr.: "Thermal Recovery Well Test Design and Interpretation," *SPE Formation Evaluation* (June 1989) 173-80.

Amyx, J.W., Bass, D.M., Jr., Whiting, R.L.: "Petroleum Reservoir Engineering," McGraw-Hill Book Company, New York, Toronto, London (1960) Ch. 4.

Atkinson, D.S., Clayton, C.A., Baldwin, J.O., and Smith, R.C.: "The Design of a Modern Steamflood in a Thick, Dipping, Heavy Oil Reservoir," paper SPE 18808 presented at the California Reg. Mtg. of SPE of AIME, Bakersfield, CA (April 5-7, 1989).

Aziz, K., Ramesh, A.B. and Woo, P.T.: "Fourth SPE Comparative Solution Project: Comparison of Steam Injection Simulators," *J. Pet. Tech.* (Dec. 1987) 1576-84.

Barua, J. and Horne, R.N.: "Computerized Analysis of Thermal Recovery Well Test Data," *SPE Formation Evaluation* (Dec. 1987) 560-66.

Bixel, H.C. and van Poollen, H. K.: "Pressure Drawdown and Buildup in the Presence of Radial Discontinuities," *Soc. Pet. Eng. J.* (Sept. 1967) 301-09.

Bourdet, D., Ayoub, J.A., and Pirard, Y.M.: "Use of Pressure Derivative in Well Test Interpretation," *SPE Formation Evaluation* (June 1989) 293-302.

Bourdet, D., Whittle, T.M., Douglas, A.A., and Pirard, Y.M.: "A New Set of Type Curves Simplifies Well Test Analysis," *World Oil* (May 1983) 95-106.

Computer Modelling Group (CMG): "*Data Entry Manual for ISCOM: In Situ Combustion and Steam Reservoir Simulator,*" Version 4.0, Calgary, AB (July 27, 1987).

Coats, K.H.: "A Fully Implicit Steamflood Model," paper SPE 6105 presented at the 51th Annual Mtg. of SPE of AIME, New Orleans, LA (Oct. 3-6, 1976).

Earlougher, R.C., Jr.: "Advances in Well Test Analysis," Monograph Volume 5, Society of Petroleum Engineers of AIME, Dallas (1977).

Eggenschwiler, M., Ramey, H.J., Jr., Satman, A., and Cinco-ley, H.:"Interpretation of Injection Well Pressure Transient Data in Thermal Oil Recovery," paper SPE 8908 presented at the California Reg. Mtg. of SPE of AIME, Los Angeles, CA (April 9-11, 1980).

Farouq Ali, S.M. and Meldau, R.F.: "Thermal Recovery Engineering," Textbook for the course Pet. E 568, University of Alberta (April 1990).

Fassihi, M.R.: "Evaluation of an Analytic Technique for Estimating Swept Volume from Thermal Pressure Falloff Tests in Heterogeneous Systems," *SPE Formation*

Evaluation (June 1988) 449-58.

Grant, M.A. and Sorey, M.L.: "The Compressibility and Hydraulic Diffusivity of a Water-Steam Flow," *Water Resources Research* Vol. 15, No. 3 (June 1979) 684-86.

Hazebroek, P., Rainbow, H., and Matthews, C.S.: "Pressure Fall-Off in Water Injection Wells," *Trans.*, AIME (1958) 213, 250-60.

Hong, K.C.: "Steamflood Strategies for a Steeply Dipping Reservoir," *SPE Reservoir Engineering* (May 1988) 431-39.

Hong, K.C.: "Effect of Gas and Edge Water on Oil Recovery by Steamflooding in a Steeply Dipping Reservoir," paper SPE 20021 presented at the 60th California Reg. Mtg. of SPE of AIME, Ventura, CA (April 4-6,1990).

Hong, K.C.: "Optimum Well Location for Steamflooding Steeply Dipping Reservoirs," paper SPE 21771 presented at the Western Reg. Mtg. of SPE of AIME, Long Beach, CA (March 20-22, 1991).

Horner, D.R.: "Pressure Builup in Wells," *Proc.*, Third World Pet. Cong., The Hague (1951), Sec. 2, 503-23; *Reprint Series No. 9 - Pressure Analysis Methods*, Society of Petroleum Engineers of AIME, Dallas (1967) 25-43.

Issaka, M.B.: "*Horizontal Well Testing Under Thermal and Non-Thermal Situations*," M.Sc. Thesis, University of Alberta, Edmonton, AB (Nov. 1991).

Issaka, M.B. and Ambastha, A.K.: "Thermal Well Testing for a Horizontal Well," paper CIM 92-24 presented at the Annual Mtg. of CIM, Calgary, AB (June 7-10, 1992).

Kazemi, H.: "Locating a Burning Front by Pressure Transient Measurements," *J. Pet. Tech.* (Feb. 1966) 227-32.

Kazemi, H., Merrill, L.S., and Jargon, J.R.: "Problems in Interpretation of Pressure Falloff Tests in Reservoirs With and Without Fluid Banks," *J. Pet. Tech.* (Sept. 1972) 1147-56.

Merrill, L.S., Jr., Kazemi, H., and Gogarty, W.B.: "Pressure Falloff Analysis in Reservoirs With Fluid Banks," *J. Pet. Tech.* (July 1974) 809-18; *Trans.*, AIME, **257**.

Messner, G.L. and Williams, R.L.: "Application of Pressure Transient Analysis in Steam Injection Wells," paper SPE 10781 presented at the California Reg. Mtg. of SPE of AIME, San Francisco, CA (March 24-26, 1982a).

Messner, G.L. and Williams, R.L.: "Further Investigation of Pressure Transient Testing in Steamflood Projects," paper SPE 11087 presented at the 57th Annual Mtg. of SPE of AIME, New Orleans, LA (Sept. 26-29, 1982b).

Miller, C.C., Dyes, A.B. and Hutchinson, C.A., Jr.: "The Estimation of Permeability and Reservoir Pressure from Bottom-Hole Buildup Characteristics," *Trans.*, AIME (1950) **189**, 91-104.

Moughamian, J.M., Woo, P.T., Dakessian, B.A., and Fitzgerald, J.G.: "Simulation and Design of Steam Drive in a Vertical Reservoir," *J. Pet. Tech.* (July 1982) 1546-54.

Onyekonwu, M.O., Ramey, H.J., Jr., Brigham, W.E., and Jenkins, R.: "Interpretation of Simulated Falloff Tests," paper SPE 12746 presented at the California Reg. Mtg. of SPE of AIME, Long Beach, CA (April 11-13, 1984).

Peaceman, P.W.: "Interpretation of Well-block Pressures in Numerical Reservoir Simulation with Nonsquare Grid Blocks and Anisotropic Permeability," *Soc. Pet. Eng. J.* (June 1983) 531-43.

Perry, R.H. and Green, D.: *Perry's Chemical Engineers' Handbook,* sixth edition, McGraw-Hill Book Co. Inc., New York City (1984) 3: 238-39.

Ramey, H.J., Jr. and Cobb, W.M.: "A General Pressure Buildup Theory for a Well in a Closed Drainage Area," *J. Pet. Tech.* (Dec. 1971) 1493-1505.

Redlich, O. and Kwong, J.N.S.: "ON THERMODYNAMICS OF SOLUTIONS. V An Equation of State. Fugacities of Gaseous Solutions," *Chemical Reviews* **44**, (1949) 233-44.

Rehkopf, B.L.: "Metson Attic Steam Drive," paper SPE 5855 presented at the 46th Annual California Reg. Mtg. of SPE of AIME, Long Beach, CA (April 8-9, 1976).

Rubin, B. and Buchanan, W.L.: "A General Purpose Thermal Model," *Soc. Pet. Eng. J.* (April 1985) 202-14.

Stanislav, J.F., Easwaran, C.V., and Kokal, S.L.: "Interpretation of thermal Well Falloff Testing," *SPE Formation Evaluation* (June 1989) 181-86 (see also paper SPE 16747 presented at the 62nd Annual Meeting of SPE of AIME in Dallas, TX (Sept. 27-30, 1987).

Stokes, D.D., Brew, J.R., Whitten, D.G., and Wooden, L.W.: "Steam Drive as a Supplemental Recovery Process in an Intermediate-Viscosity Reservoir, Mount Poso Field, California," *J. Pet. Tech.* (Jan. 1978) 125-31.

Tang, R.W.-K.: "*Transient Pressure Analysis in a Composite Reservoir*," SUPRI-A Tech. Report 31, DOE Repot No. DOE/ET/12056-31 (Aug. 1982).

Tortike, W.S. and Farouq Ali, S.M.: "Saturated-Steam-Property Functional Correlations for Fully Implicit Thermal Reservoir Simulation," *SPE Reservoir Engineering* (Nov. 1989) 471-74.

van Poollen, H.K.: "Radius-of-Drainage and Stabilization-time Equations," *Oil & Gas J.* (Sept. 14, 1964) 138-46.

van Poollen, H.K.: "Transient Tests Find Fire Front in an In-situ Combustion Project," *Oil & Gas J.* (Feb. 1, 1965) 78-80.

Walsh, J.W., Jr., Ramey, H.J., Jr., and Brigham, W.E.: "Thermal Injection Well Falloff Testing," paper SPE 10227 presented at the 56th Annual Mtg. of SPE of AIME, San Antonia, TX (Oct. 5-7, 1981).

Yortsos, Y.C.: "Distribution of Fluid Phases Within the Steam Zone in Steam-Injection Processes," *Soc. Pet. Eng. J.* (Aug. 1984) 458-66.

Ziegler, V.M.: "Injection-Well Testing in a Light-Oil Steamflood, Buena Vusta Hills Field, California," *SPE Production Engineering* (November 1990) 394-402.

APPENDIX A

DERIVATION OF FORMULA IN REAL GAS ANALYSIS

Estimation of k and s

If steam is treated as a liquid, k and s is calculated as follows:

$$k_{ec} = \frac{162.6(q_s)_{sc} B_s \mu_s}{m_s h} \quad , \qquad \text{(A-1)}$$

$$s = 1.1513\left((\frac{p_{wfs} - p_{1hr}}{m_s}) - \log(\frac{k_{ec}}{\phi \mu_s c_t r_w^2}) + 3.23 \right) \quad . \qquad \text{(A-2)}$$

From

$$p\,V = z\,n\,R\,T = z\frac{W}{M}R\,T \quad , \qquad \text{(A-3)}$$

we have

$$B_s = \frac{z\,T\,p_{sc}}{p\,T_{sc}} \quad , \qquad \text{(A-4)}$$

and

$$(\vartheta_s)_{sc} = \frac{V_{sc}}{W} = \frac{z_{sc}\,R\,T_{sc}}{p_{sc}\,M} \quad . \qquad \text{(A-5)}$$

We know

$$(q_s)_{sc} = (q_w f_s)_{sc}\,(\rho_w)_{sc}\,(\vartheta_s)_{sc} \quad . \qquad \text{(A-6)}$$

$$k_{ec} = \frac{162.6\,(q_w f_s)_{sc}\,(\rho_w)_{sc}\,z_{sc}\,z\,R\,T\,\mu_s}{p\,m_s\,h\,M} \quad . \tag{A-7}$$

Since $z_{sc} = 1.0$, $(\rho_w)_{sc} = 62.4$ lb/ft^3 at $T_{sc} = 520$ ^{o}R and $p_{sc} = 14.7$ psia, $R = 10.732$ psi·ft^3·/(lb mole·^{o}R), $M = 18.02$ lb/(lb mole), Eq. A-7 becomes

$$k_{ec} = \frac{6042.7\,(q_w f_s)_{sc}\;\,z\,T\,\mu_s}{p\,m_s\,h} \quad . \tag{A-8}$$

Note that

$$2\,p\,m_s = m_s' \quad . \tag{A-9}$$

If T is taken as $\overline{T}$, z and μ_s are evaluated at $\overline{p}$, $\overline{T}$, Eq. A-8 will become

$$k_{ec} = \frac{12085.4\,(q_w f_s)_{sc}\;\,\overline{z}\,\overline{T}\,\overline{\mu}_s}{m_s' h} \quad . \tag{A-10}$$

Because of Eq. A-9, Eq. A-2 can be written as

$$s = 1.1513\left((\frac{p_{wfs}^2 - p_{1hr}^2}{m_s'}) - \log(\frac{k_{ec}}{\phi\,\overline{\mu}_s c_t r_w^2}) + 3.23 \right) \quad . \tag{A-11}$$

Eqs. (A-10) and (A-11) are the calculation formula of k and s for the pressure squared method.

For the pseudo-pressure function method, note that

Similarly, we have the calculation formulae for the pseudopressure function method as follows:

$$k_{ec} = \frac{12085.4\,(q_w f_s)_{sc}\,\bar{T}}{m_s'' h} \quad , \tag{A-13}$$

$$s = 1.1513\left((\frac{\psi_{wfs} - \psi_{1hr}}{m_s''}) - \log(\frac{k_{ec}}{\phi\,\bar{\mu}_s c_t r_w^2}) + 3.23 \right) \quad . \tag{A-14}$$

Estimation of Swept Volumes V_{sc}

In the pressure analysis method, the swept volume V_{sc} is calculated from

$$V_{sc} = \frac{(5.615)(q_s)_{sc} B_s}{(24) m_c\, \phi\, c_t} \quad . \tag{A-15}$$

Substitute $(q_s)_{sc}$ and B_s expressions into Eq. A-15, Eq. (A-15) becomes

$$V_{sc} = \frac{5.615\,(q_w f_s)_{sc}\,(\rho_w)_{sc}\, z_{sc}\, z\, R\, T}{24\, p\, m_c\, \phi\, c_t\, M} \quad . \tag{A-16}$$

If all the constants are evaluated, Eq. A-16 will become

$$V_{sc} = \frac{8.6946\,(q_w f_s)_{sc}\, z\, T}{p\, m_c\, \phi\, c_t} \quad . \tag{A-17}$$

Note that

and if T is taken as $\overline{T}$, z is evaluated at $\overline{p}$, $\overline{T}$, Eq. A-17 will become

$$V_{sc} = \frac{17.389\,(q_w f_s)_{sc}\,\overline{z}\,\overline{T}}{\phi\, c_t\, m_c'} \quad . \tag{A-19}$$

Eq. (A-19) is the calculation formula of swept volume for the pressure squared method.

For the pseudopressure function method,

$$\frac{2p}{\mu_s\, z} m_c = m_c'' \quad . \tag{A-20}$$

Thus, the calculation formula of swept volume for the pseudopressure function method is

$$V_{sc} = \frac{17.389\,(q_w f_s)_{sc}\,\overline{T}}{\phi\, \overline{\mu}_s c_t\, m_c''} \quad . \tag{A-21}$$

APPENDIX B

PROGRAM FOR THE

CALCULATION OF PSEUDOPRESSURE FUNCTION

```
C     PROGRAM NAME: PSEUDOP
C
C     THIS PROGRAM IS TO CALCULATE PSEUDOPRESSURE FUNCTION
C     FOR THE THERMAL WELL TESTING.
C
C     VARIABLE LIST
C     P     = PRESSURE, PSIA
C     T     = TIME, HOUR
C     PP    = PSEUDOPRESSURE, PSIA2/CP
C     NDATA = NUMBER OF DATA POINTS ON A T VS. P ARRAY
C     Z     = Z FACTOR
C     VISG  = VISCOSITY
C     DPP1  = FORMER PSEUDOPRESSURE
C     DPP2  = INCREMENTAL PSEUDOPRESSURE
C     PDATA  ----  PRESSURE INPUT DATA FILE
C     PPDATA ----  PSEUDOPRESSURE OUTPUT DATA FILE
C
      IMPLICIT REAL*8 (A-H,O-Z)
      PARAMETER(NUM = 100)
      DIMENSION T(0:NUM), P(0:NUM), PP(0:NUM)
      OPEN(UNIT=7, FILE='PDATA', STATUS='OLD')
      OPEN(UNIT=8, FILE='PPDATA',STATUS='OLD')
C     READ PRESSURE VS. TIME DATA 'PDATA'
      READ(7,*) NDATA
      DO 10 I=1,NDATA
```

```
C     CALCULATE PSEUDOPRESSURE
      P(0) = 0.0
      PP(0)= 0.0
      DPP1 = 0.0
      DO 100 I = 1,NDATA
      CALL ZFACT(P(I), Z)
C     THE RELATIONSHIP OF VISCOSITY VS. P IS OBTAINED FROM
C     SIMULATION.
      VISG = 0.00199*(P(I)-680.86)/(1543.2-680.86)+0.017705
      DPP2 = 2.0*P(I)/(Z*VISG)
      PP(I) = (DPP1+DPP2)/2.0*(P(I)-P(I-1))+PP(I-1)
      DPP1 = DPP2
  100 CONTINUE
      WRITE(8,110) NDATA
  110 FORMAT(2X, I5)
      DO 200 I = 1, NDATA
      WRITE(8,210) T(I), PP(I)
  200 CONTINUE
  210 FORMAT(2X, F15.6, 2X, F15.6)
      STOP
      END
C
C
      SUBROUTINE ZFACT(P1,Z)
C
C     SUBROUTINE NAME: ZFACT(P1,Z)
C     THIS SUBROUTINE IS TO CALCULATE Z FACTOR FROM REDLICH-
C     KWONG EOS USING NEWTON'S METHOD (THE TECHNIQUE
C     OF SUCCESSIVE APPROXIMATIONS OF REAL ROOTS OF A EQUATION).
C     THE INPUT DATA REQUIRED ARE: P, PC, TC. TEMPERATURE IS
C     CALCULATED FROM THE SATURATION PRESSURE USING
C     TORTIKE AND FAROUQ ALI FORMULA.
C
C     VARIABLE LIST
C     P   = PRESSURE, PSIA
C     PC  = CRITICAL PRESSURE, PSIA
```

```
C     T    = TEMPERATURE, oR
C     TC = CRITICAL TEMPERATURE, oR
C     NPT  = NUMBER OF PRESSURE AND TEMPERATURE ARRAY
C     A0, B0 = END POINTS OF THE VARIABLE
C
      IMPLICIT REAL*8 (A-H,O-Z)
C     DEFINE THE FUNCTION AND THE DERIVATIVES
      F(X)=X**3.0-X**2.0+C*X-D
      F1(X)=3.0*X**2.0-2.0*X+C
      F2(X)=6.0*X-2.0
C     INPUT DATA
      PC = 3198.0
      TC = 1165.14
      A0 = 0.5
      B0 = 1.2
C     CALCULATE TEMPERATURE FROM SATURATION PRESSURE
      TEM = ALOG(P)
      T = 561.435 + 33.8866 * TEM + 2.18893 * (TEM)** 2.0 +
     #0.0808998*(TEM)**3.0 + 0.034203 * (TEM)**4.0
C     CALCULATE THE COFFICIENTS OF EOS
      A=0.42748*(P/PC)/((T/TC)**2.5)
      B=0.08664*(P/PC)/(T/TC)
      C=A-B**2.0-B
      D=A*B
      TEM=F(A0)*F(B0)
      IF(TEM.GT.0.0)THEN
      WRITE(6,*)'WRONG END POINT VALUES'
      GO TO 99
      ENDIF
      TEM=(A0+B0)/2.0
      IF(F2(TEM).LT.0.0) Z0=A0
      IF(F2(TEM).GT.0.0) Z0=B0
      TEM1=ABS(F1(Z0)**2.0)
      TEM2=ABS(F2(Z0)*F(Z0)/2.0)
      IF(TEM1.LT.TEM2)THEN
      WRITE(6,*)'WRONG Z0 VALUE'
```

```
      GO TO 99
      ENDIF
C     CALCULATE Z FACTOR USING NEWTON ITERATION FORMULA
      XN=Z0
      DO 20 I=1,100
      XN1=XN-F(XN)/F1(XN)
      TEM=ABS(XN1-XN)
      IF(TEM.LT.0.00001)THEN
      GO TO 30
      ELSE
      XN=XN1
      ENDIF
 20   CONTINUE
 30   Z=XN1
 99   RETURN
      END
```

APPENDIX C

AN EXAMPLE OF

INPUT AND OUTPUT DATA FOR APPENDIX B (RUN 1)

INPUT DATA

File Name: PDATA
The first row: Number of data points.
The first column: Shut-in time, hr.
The second column: Pressure, psia.

47	
0.001	1098.9
0.002	1096.7
0.003	1095.1
0.005	1092.9
0.006	1092.0
0.008	1090.6
0.001	1089.5
0.015	1087.6
0.020	1086.3
0.030	1084.4
0.040	1083.1
0.050	1082.0
0.060	1081.2
0.080	1079.9
0.100	1078.8
0.130	1077.6
0.160	1076.7
0.200	1075.7
0.250	1074.6
0.300	1073.8
0.350	1073.1
0.400	1072.4
0.450	1071.9
0.500	1071.4
0.600	1070.5
0.650	1070.1

OUTPUT DATA

File Name: PPDATA
The first row: Number of data points.
The first column: Shut-in time, hr.
The second column: Pseudopressure: psia2/cp

47	
0.001	81308732.280646
0.002	80983520.039150
0.003	80747439.459287
0.005	80423429.899358
0.006	80291081.146978
0.008	80085436.776914
0.010	79924056.708244
0.015	79645718.887820
0.020	79455576.080480
0.030	79178111.720133
0.040	78988566.395352
0.050	78828371.412601
0.060	78711975.072133
0.080	78523026.934743
0.100	78363337.170974
0.130	78189328.157732
0.160	78058956.965155
0.200	77914236.346158
0.250	77755209.305350
0.300	77639662.253267
0.350	77538633.852907
0.400	77437675.696692
0.450	77365605.730646
0.500	77293571.596884
0.600	77164000.443826
0.650	77106450.523729

0.700	1069.7
0.800	1069.0
1.000	1067.8
1.300	1066.2
1.600	1064.7
2.000	1062.8
2.500	1060.6
3.000	1058.5
3.500	1056.4
4.000	1054.4
4.500	1052.4
5.000	1050.4
6.000	1046.6
7.000	1043.0
8.000	1039.5
10.00	1032.7
13.00	1023.1
16.00	1014.0
20.00	1002.4
25.00	988.5
30.00	979.9

0.700	77048923.530002
0.800	76948306.452935
1.000	76775983.351928
1.300	76546540.064392
1.600	76331769.936220
2.000	76060190.206479
2.500	75746374.973706
3.000	75447470.097097
3.500	75149196.019549
4.000	74865711.745885
4.500	74582799.273205
5.000	74300458.430233
6.000	73765584.986336
7.000	73260764.685429
8.000	72771740.324749
10.00	71826629.667581
13.00	70503570.396289
16.00	69261527.779198
20.00	67695322.647311
25.00	65843715.410948
30.00	64711820.623210

APPENDIX D

FIGURES FOR ANALYSIS OF THE SIMULATED THERMAL WELL TESTING DATA

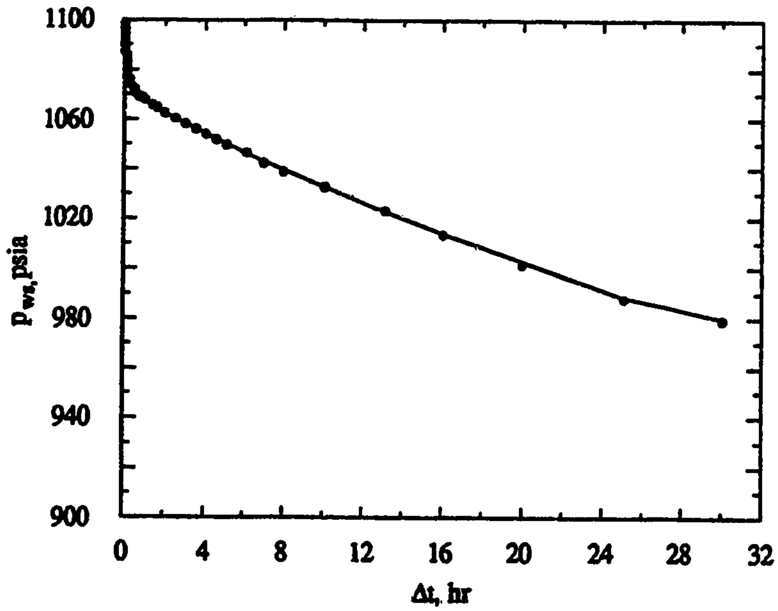

Fig. D.1 - Pressure falloff data for Run 1.

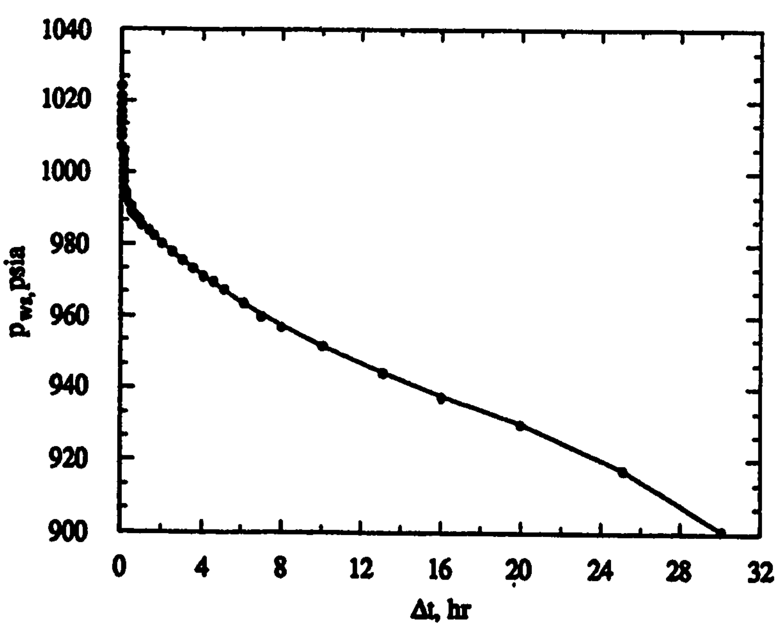

Fig. D.2 - Pressure falloff data for Run 2.

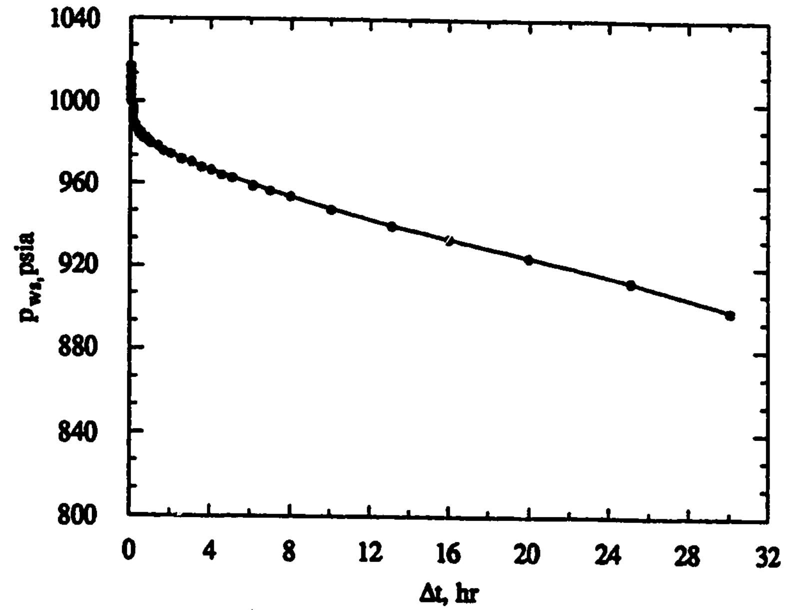

Fig. D.3 - Pressure falloff data for Run 3 (K=1).

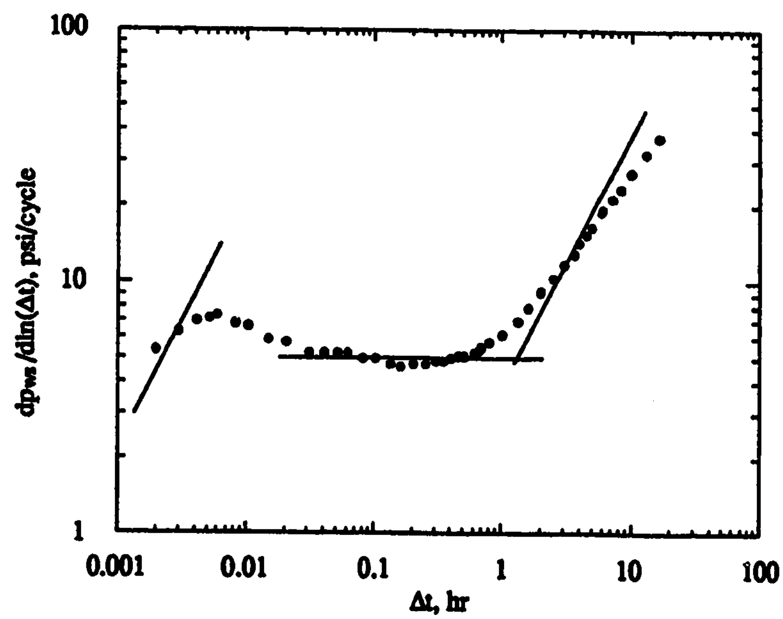

Fig. D.4 - Semilog pressure derivatives for Run 3 (K=1).

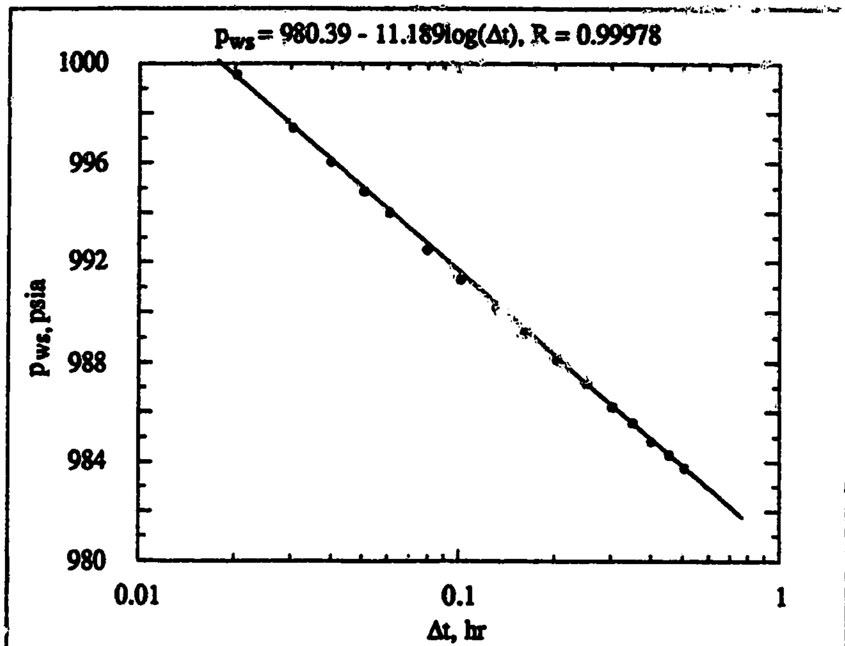

Fig. D.5 - Semilog straight line for Run 3 (K=1).

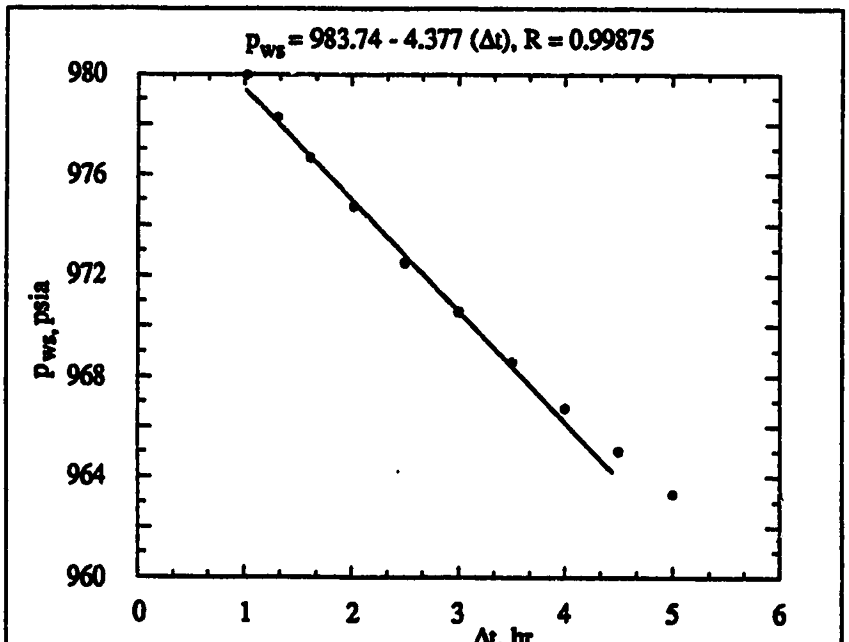

Fig. D.6 - Cartesian straight line for Run 3 (K=1).

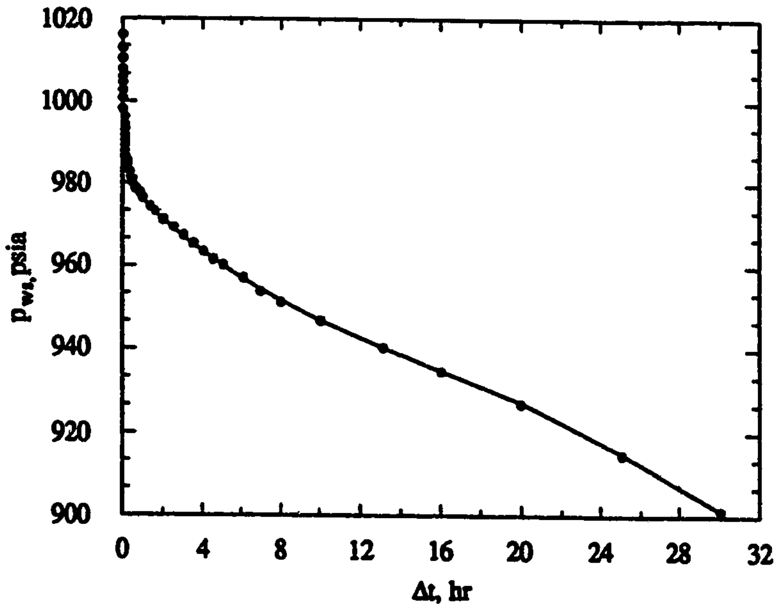

Fig. D.7 - Pressure falloff data for Run 3 (K=2).

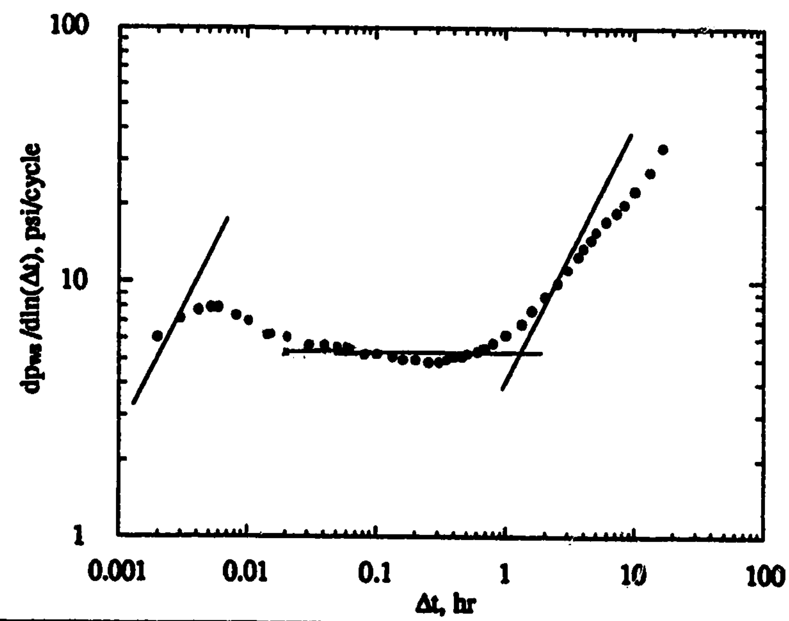

Fig. D.8 - Semilog pressure derivatives for Run 3 (K=2).

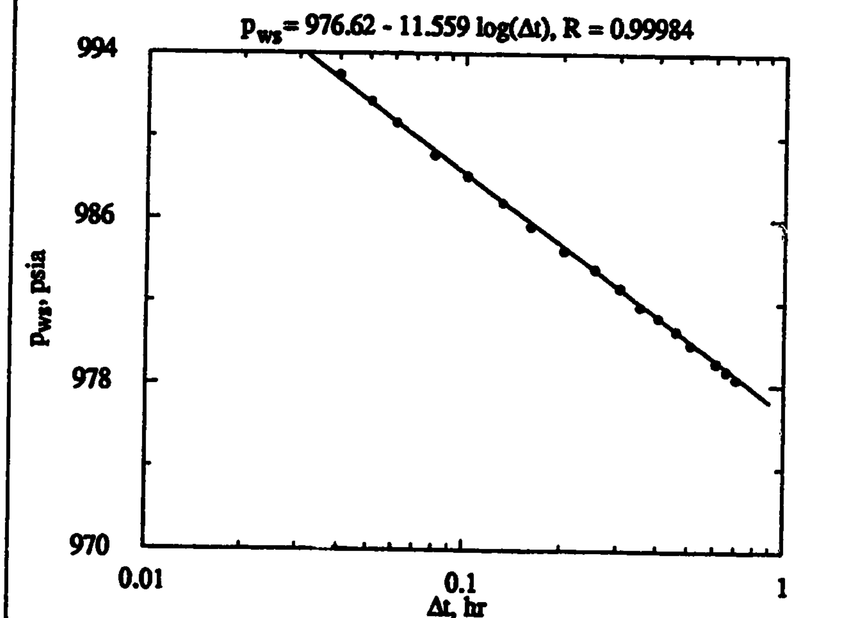

Fig. D.9 - Semilog straight line for Run 3 (K=2).

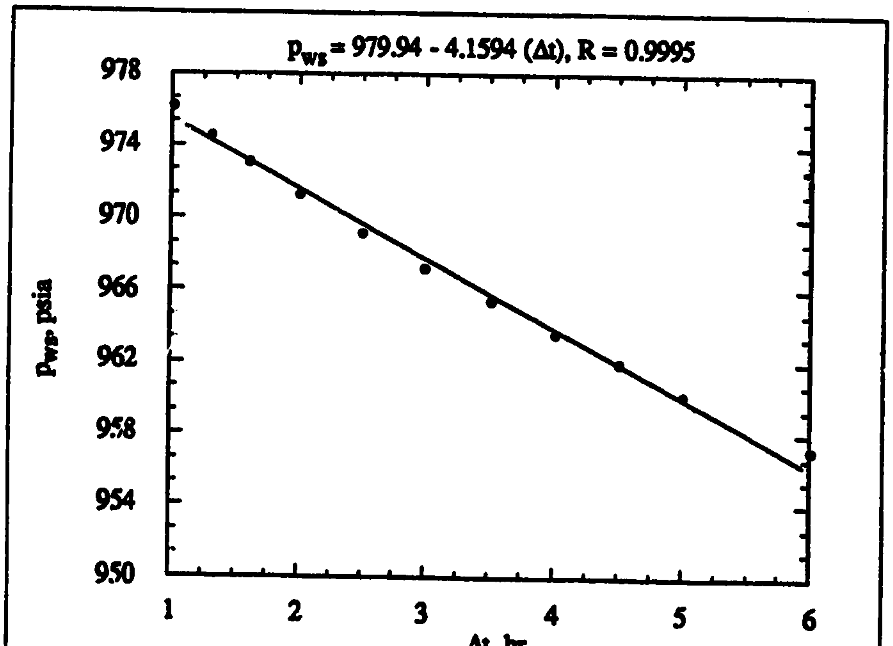

Fig. D.10 - Cartesian straight line for Run 3 (K=2).

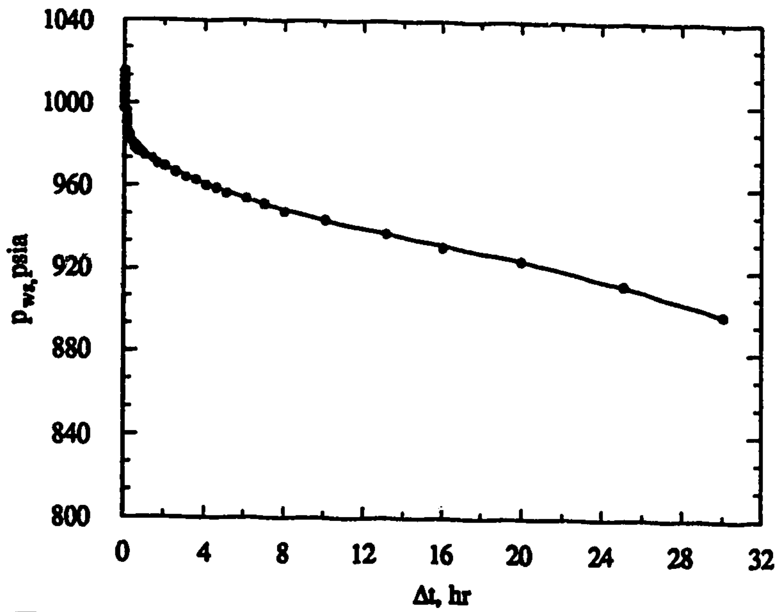

Fig. D.11 - Pressure falloff data for Run 3 (K=3).

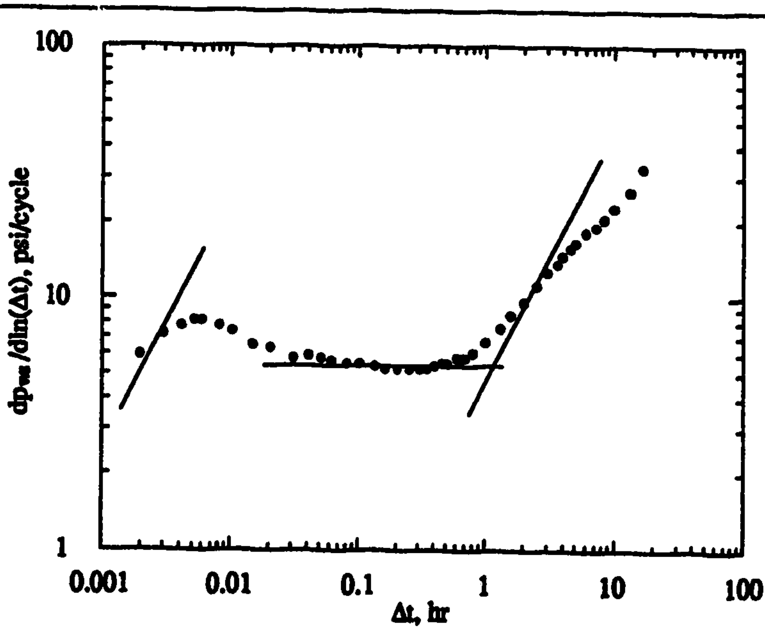

Fig. D.12 - Semilog pressure derivatives for Run 3 (K=3).

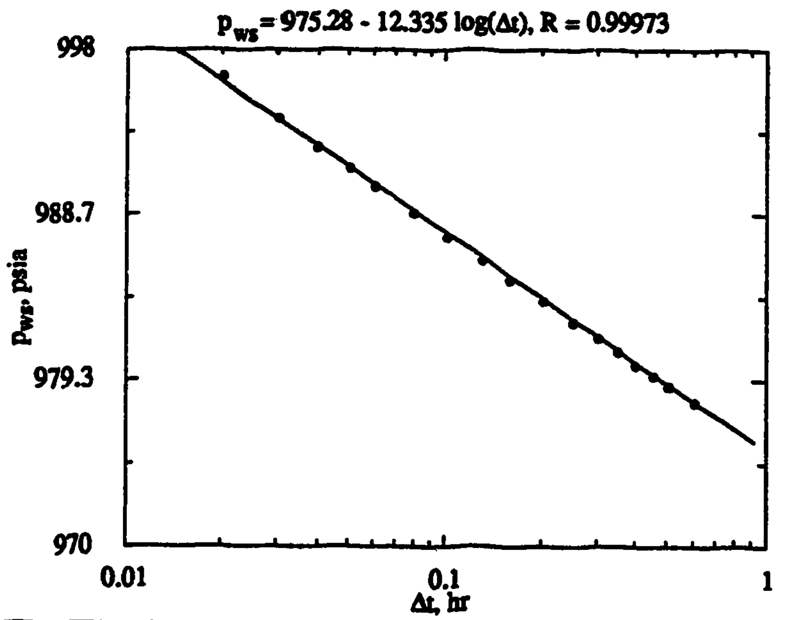

Fig. D.13 - Semilog straight line for Run 3 (K=3).

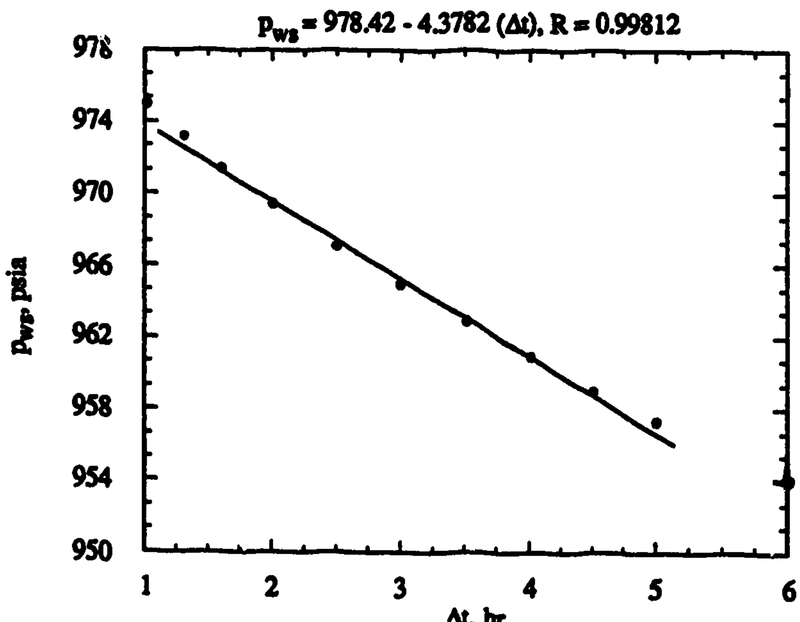

Fig. D.14 - Cartesian straight line for Run 3 (K=3).

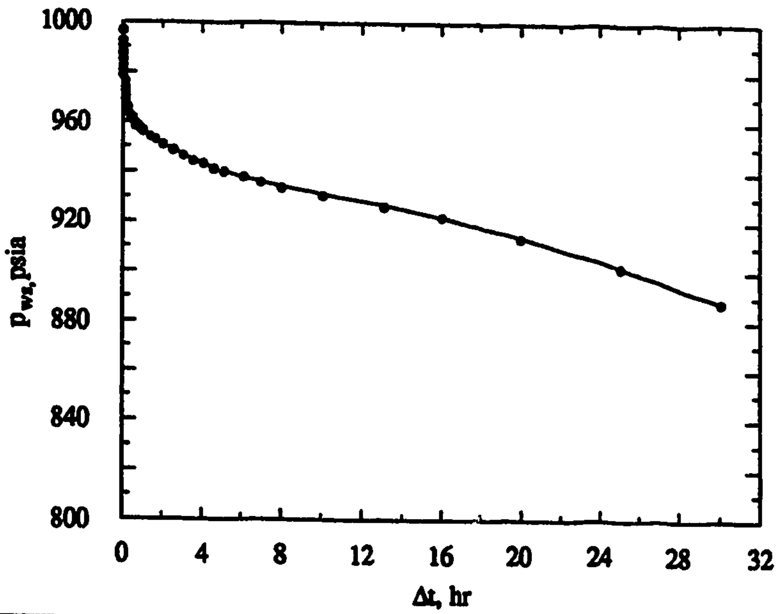

Fig. D.15 - Pressure falloff data for Run 4.

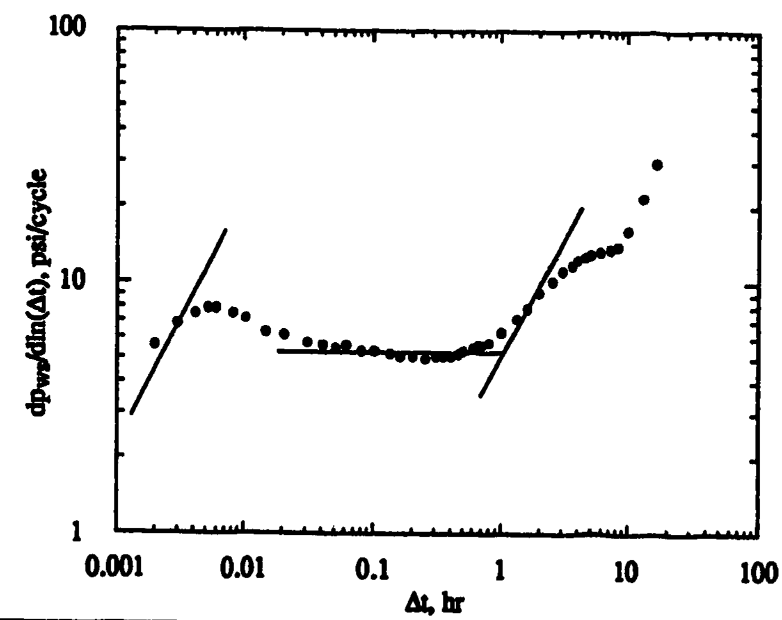

Fig. D.16 - Semilog pressure derivative data for Run 4.

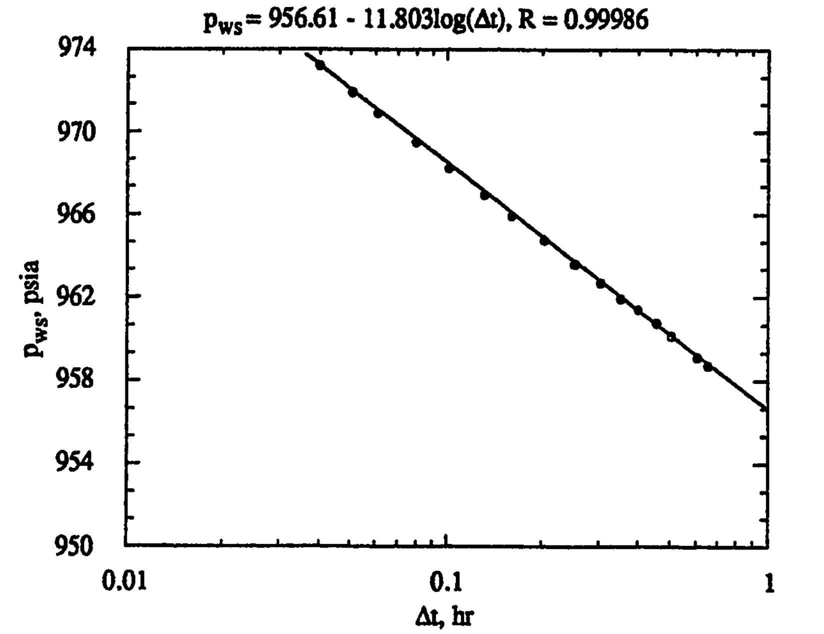

Fig. D.17 - Semilog straight line for Run 4.

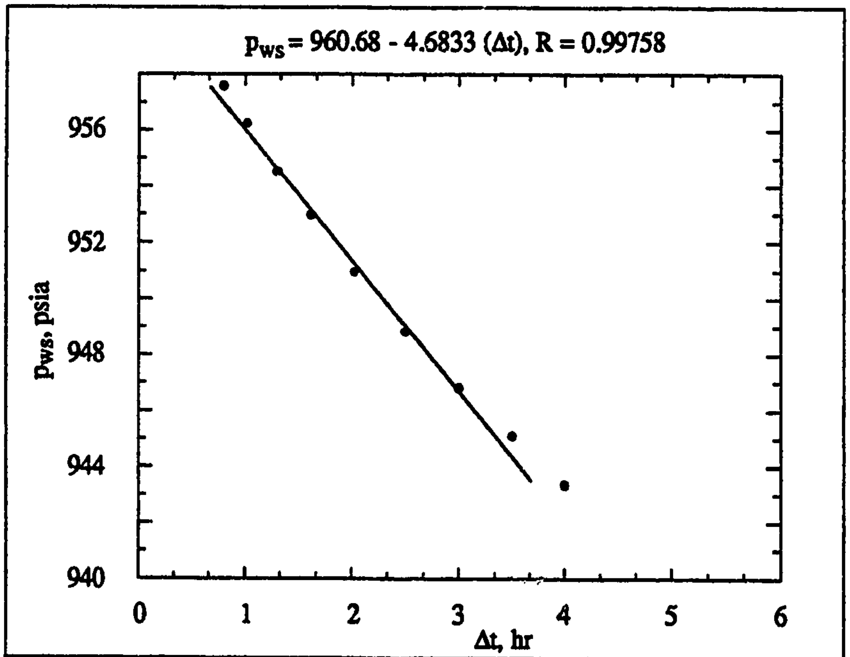

Fig. D.18 - Cartesian straight line for Run 4.

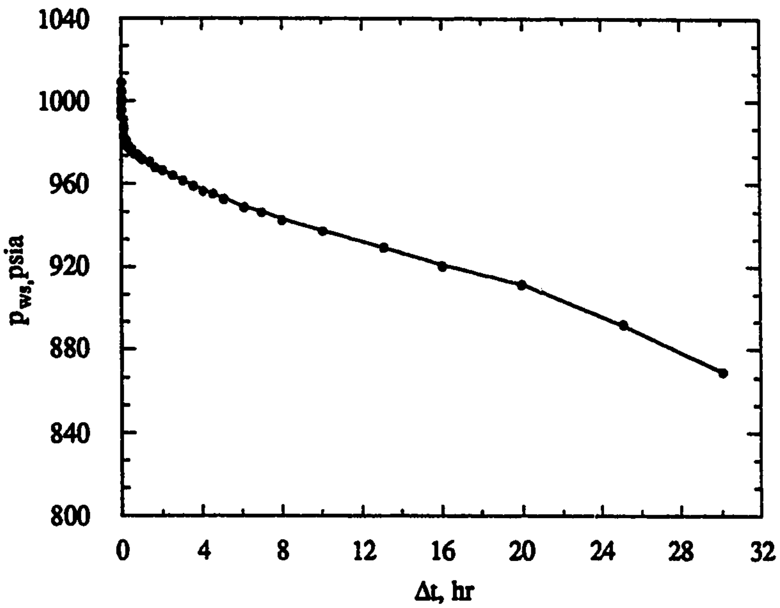

Fig. D.19 - Pressure falloff data for Run 5 (K=1).

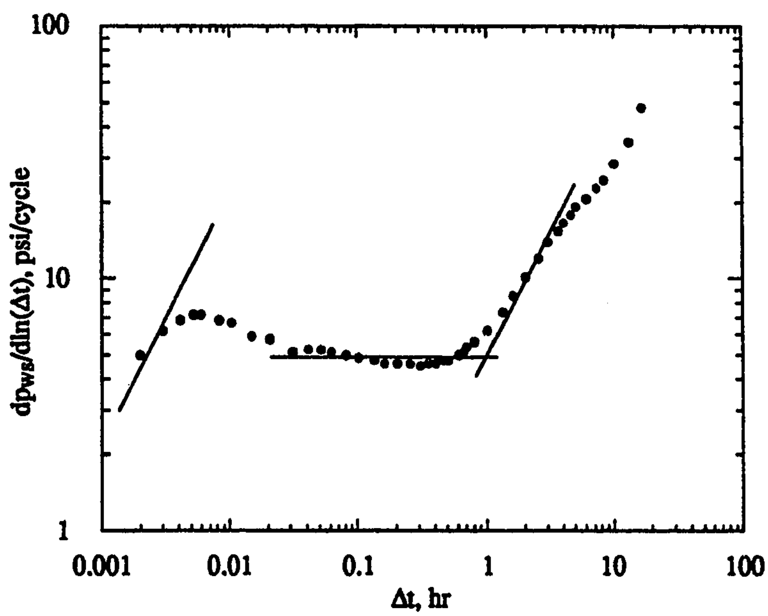

Fig. D.20 - Semilog pressure derivatives for Run 5 (K=1).

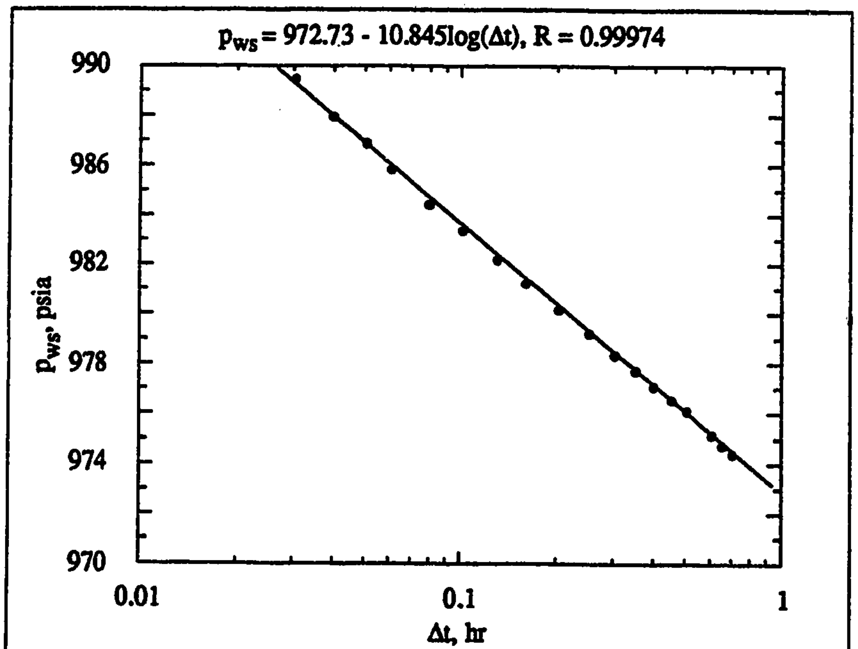

Fig. D.21 - Semilog straight line for Run 5 (K=1).

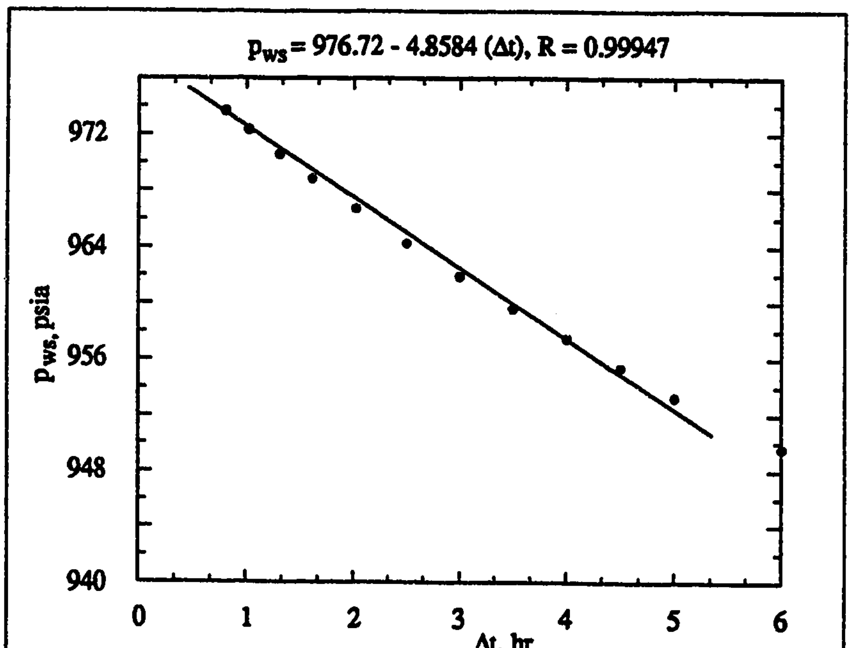

Fig. D.22 - Cartesian straight line for Run 5 (K=1).

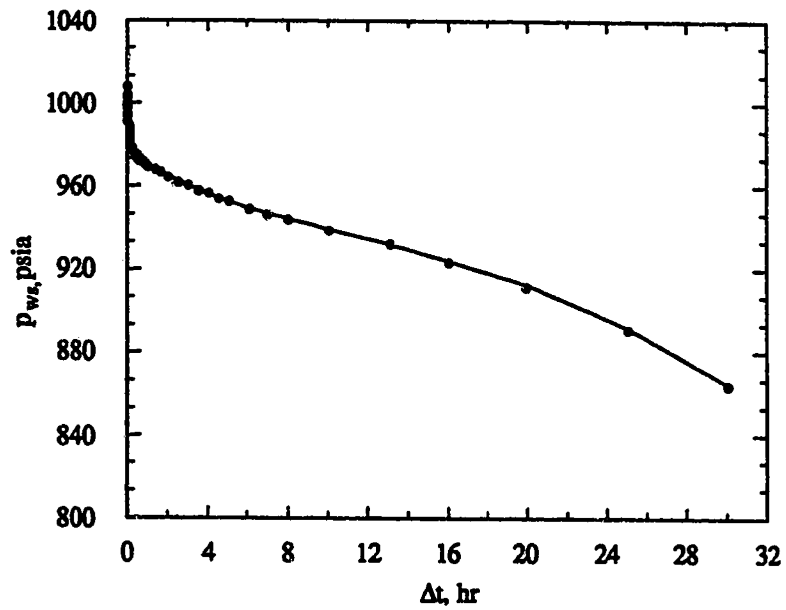

Fig. D.23 - Pressure falloff data for Run 5 (K=2).

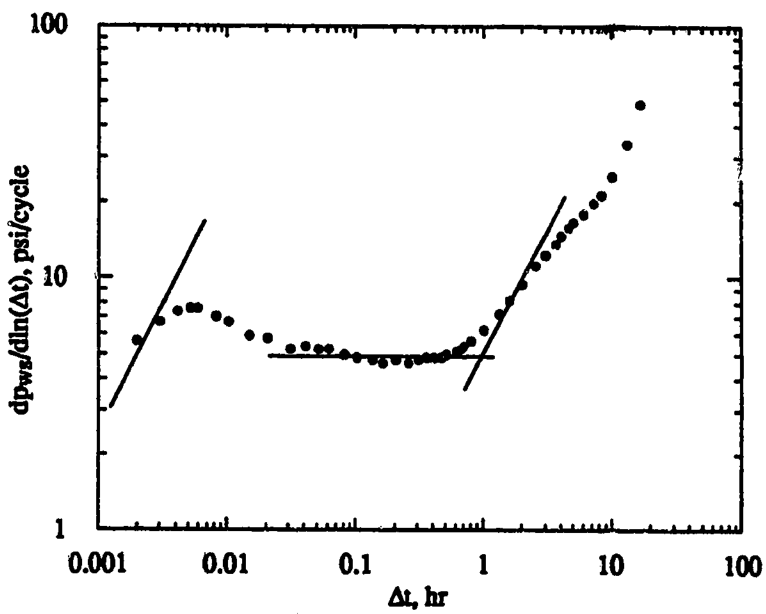

Fig. D.24 - Semilog pressure derivatives for Run 5 (K=2).

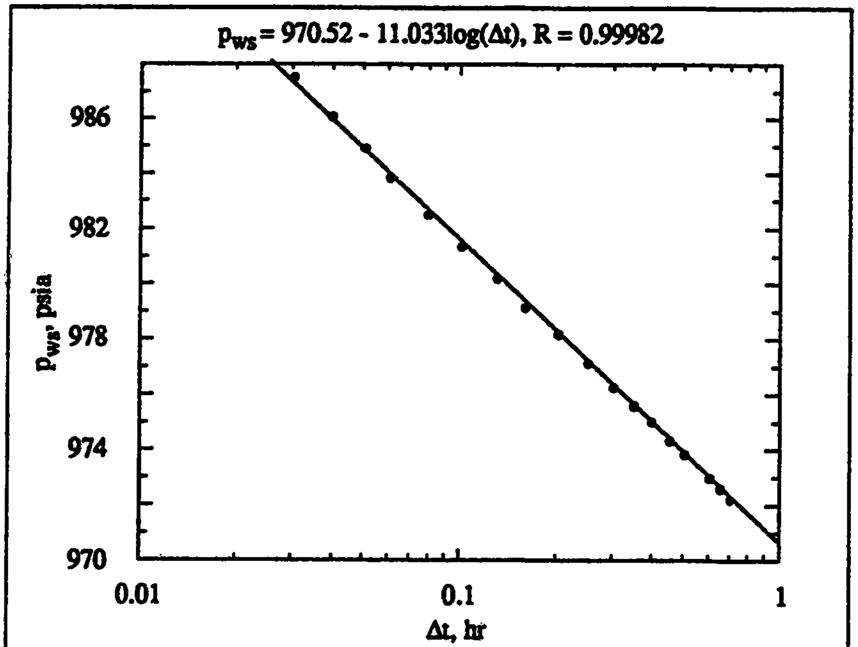

Fig. D.25 - Semilog straight line for Run 5 (K=2).

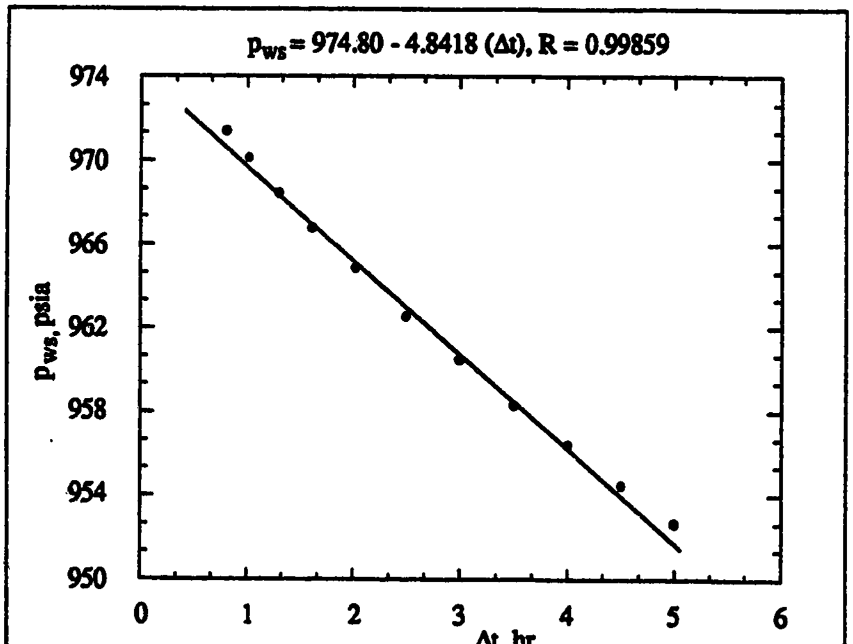

Fig. D.26 - Cartesian straight line for Run 5 (K=2).

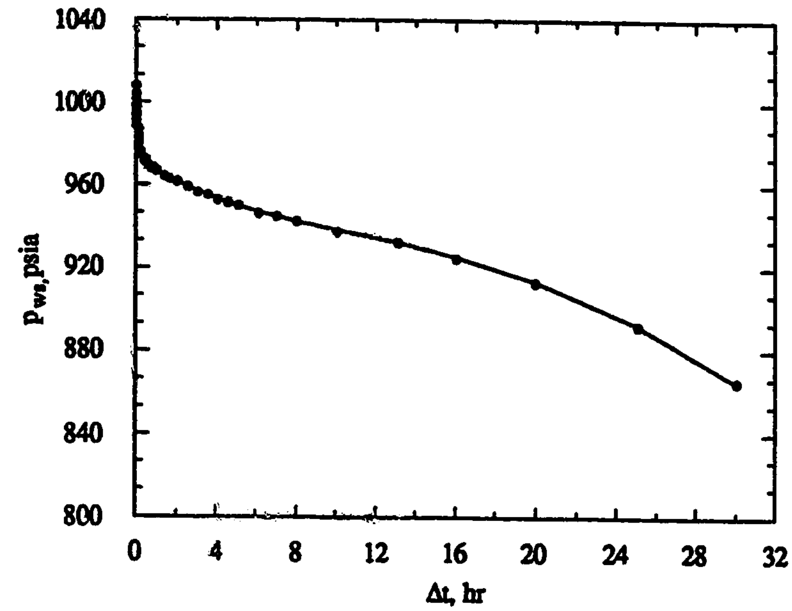

Fig. D.27 - Pressure falloff data for Run 5 (K=3).

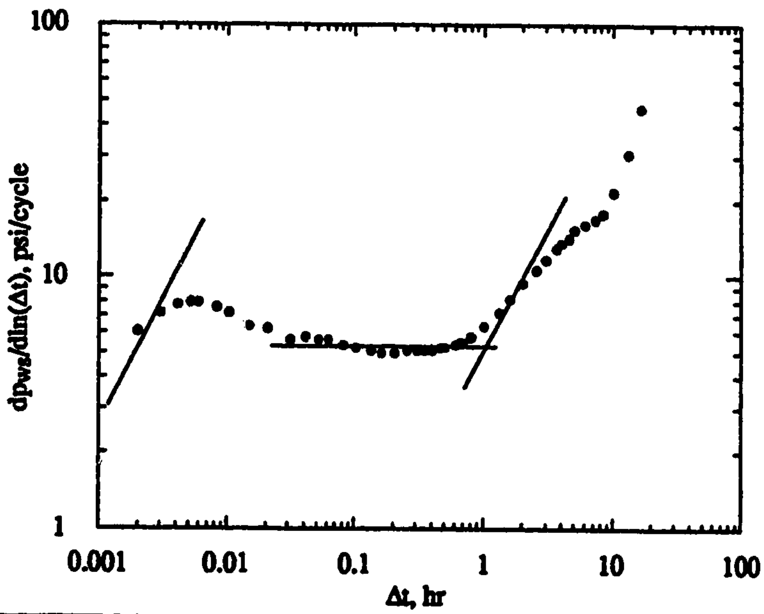

Fig. D.28 - Semilog pressure derivatives for Run 5 (K=3).

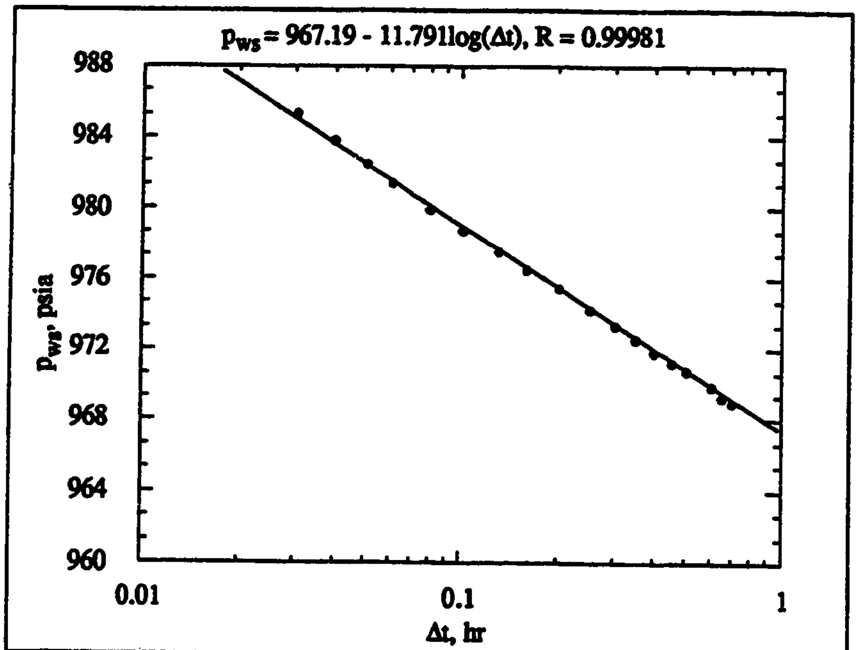

Fig. D.29 - Semilog straight line for Run 5 (K=3).

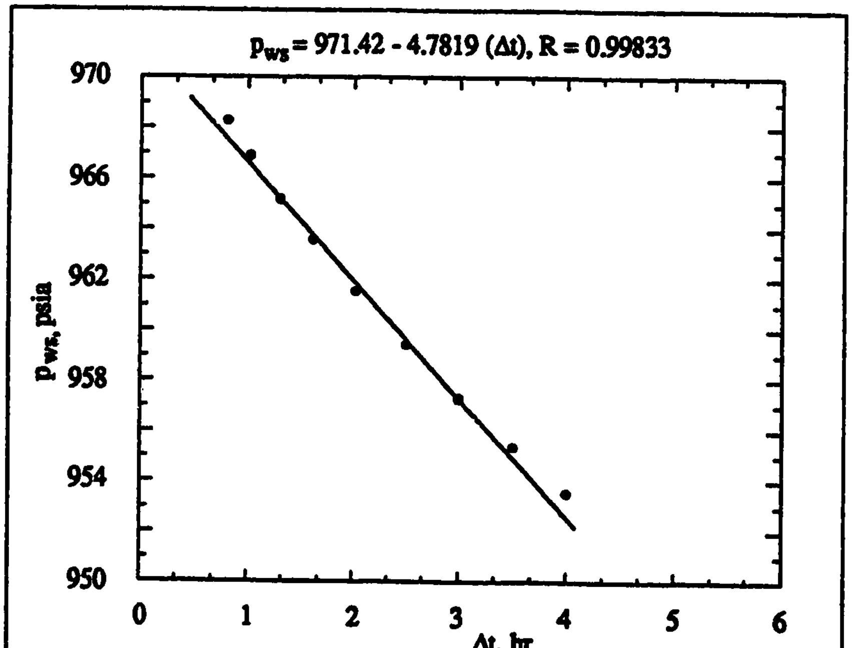

Fig. D.30 - Cartesian straight line for Run 5 (K=3).

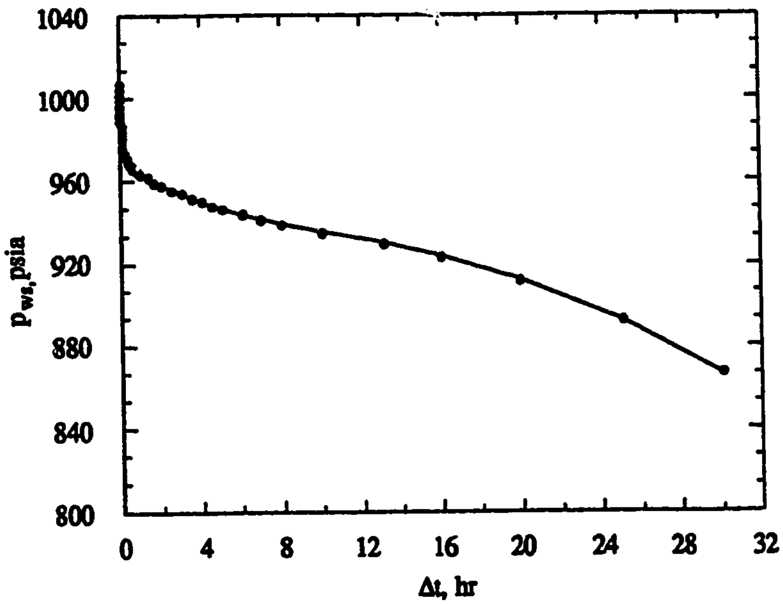

Fig. D.31 - Pressure falloff data for Run 5 (K=4).

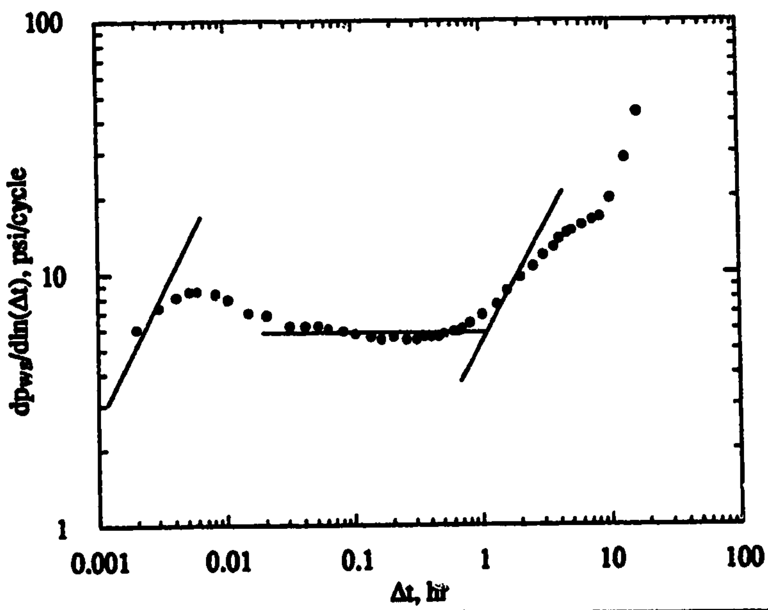

Fig. D.32 - Semilog pressure derivatives for Run 5 (K=4).

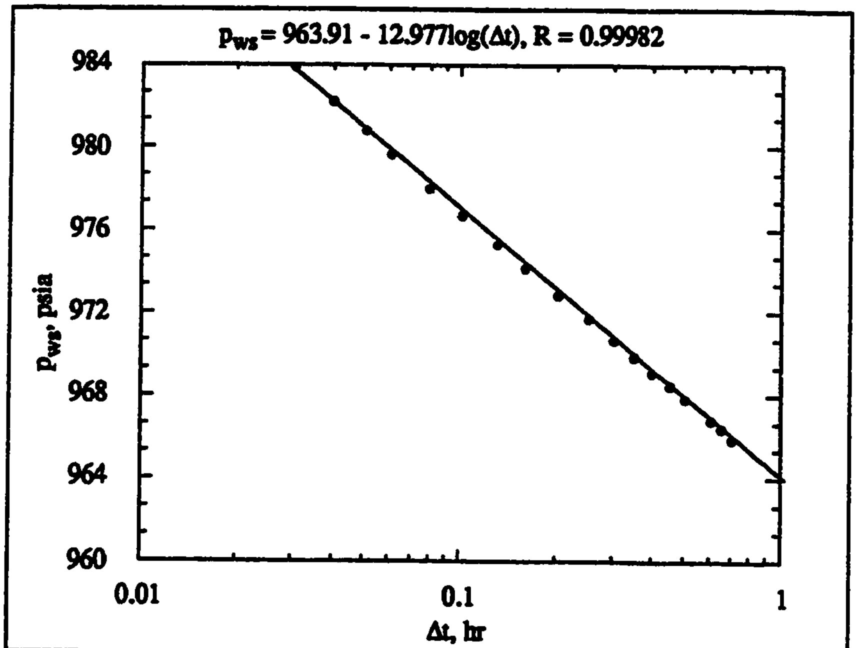

Fig. D.33 - Semilog straight line for Run 5 (K=4).

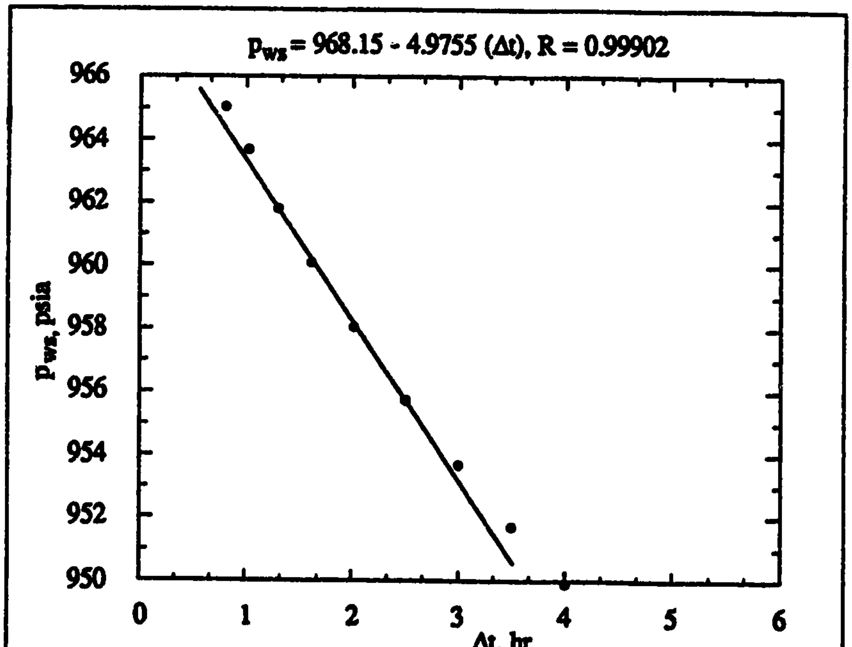

Fig. D.34 - Cartesian straight line for Run 5 (K=4).

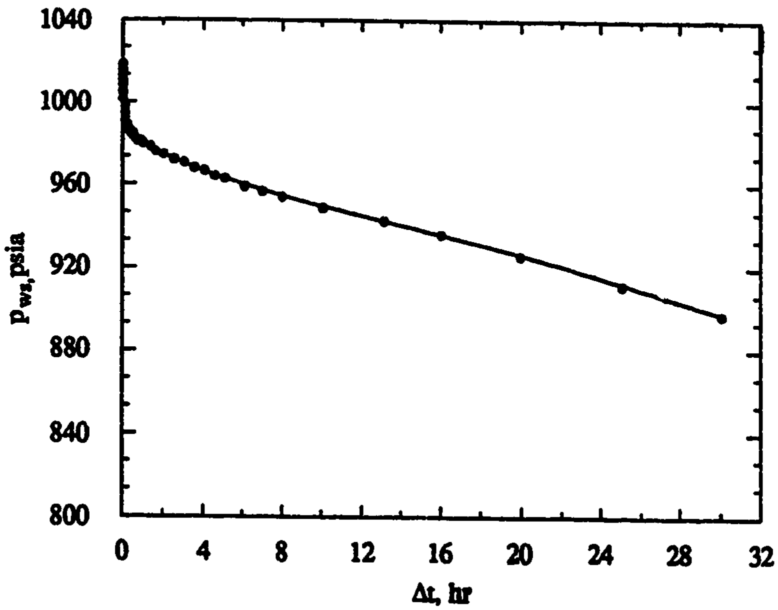

Fig. D.35 - Pressure falloff data for Run 6.

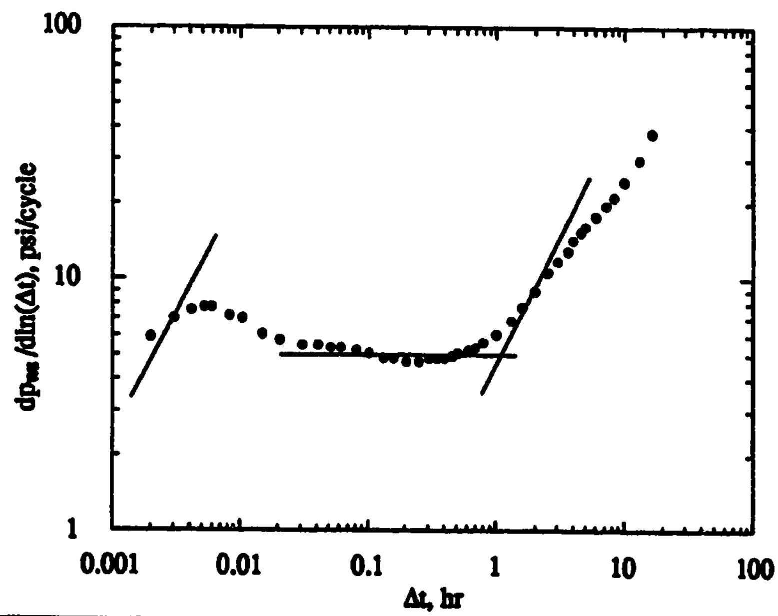

Fig. D.36 - Semilog pressure derivative data for Run 6.

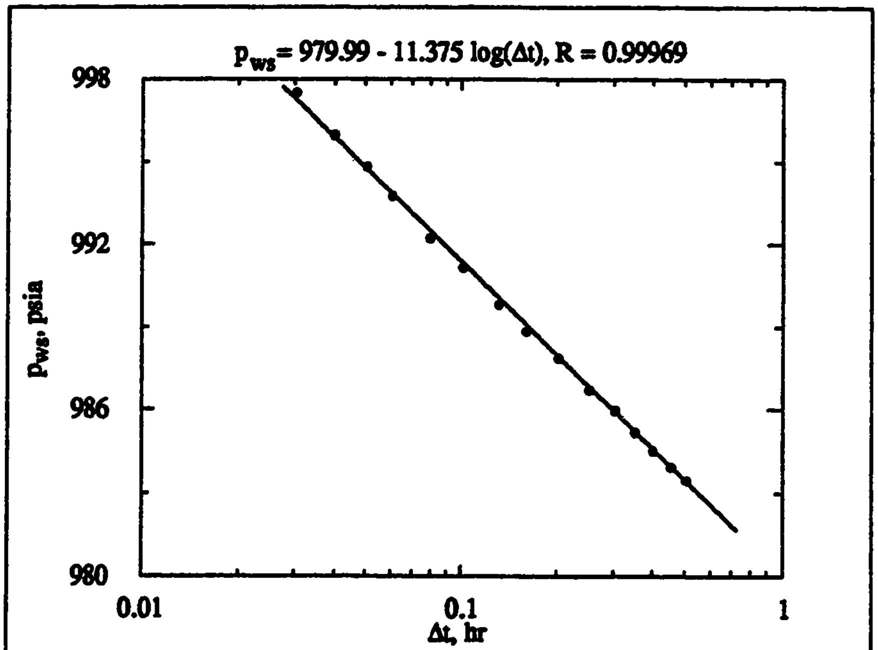

Fig. D.37 - Semilog straight line for Run 6.

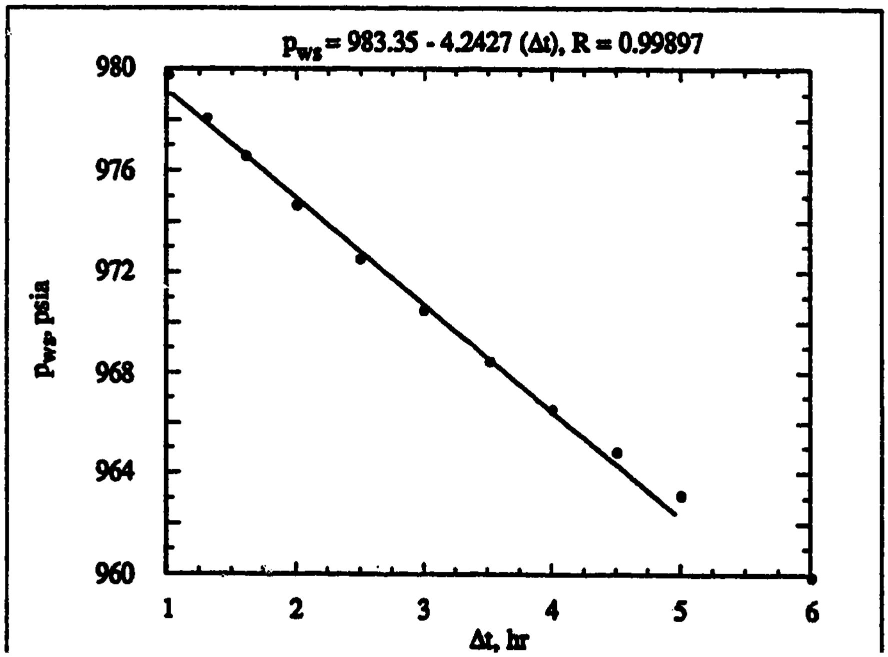

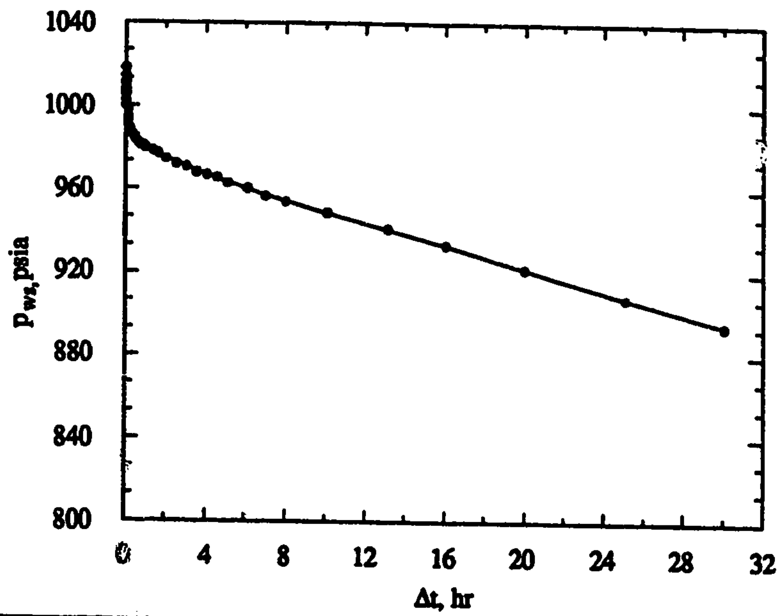

Fig. D.39 - Pressure falloff data for Run 7.

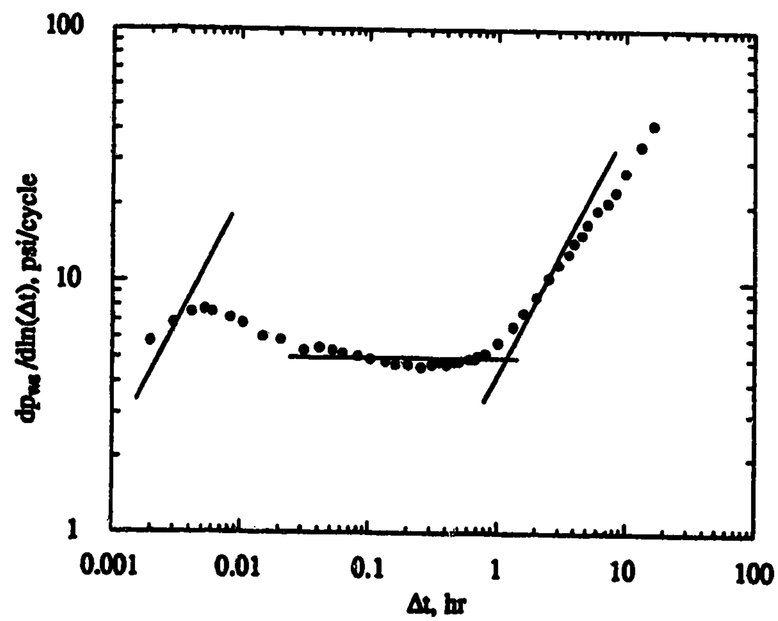

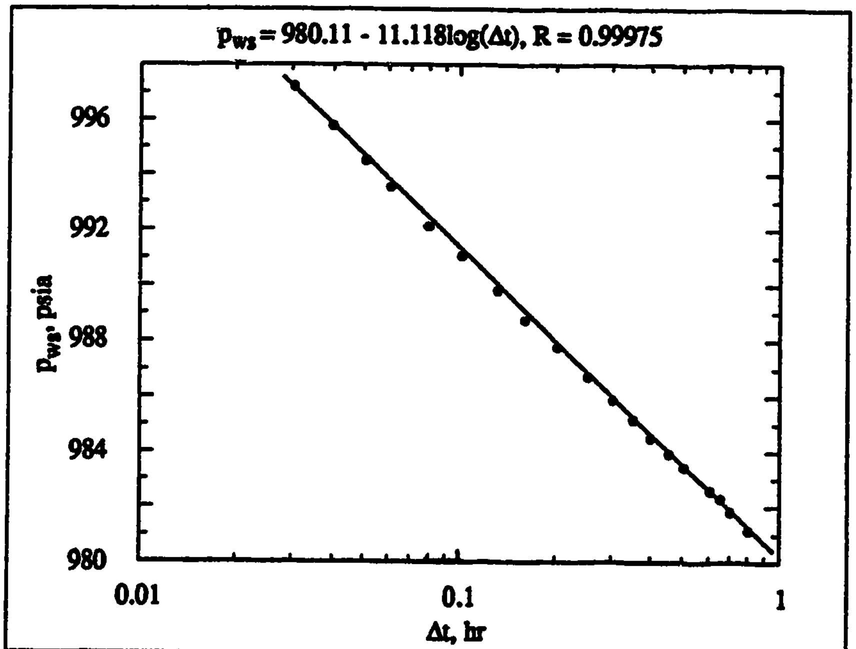

Fig. D.41 - Semilog straight line for Run 7.

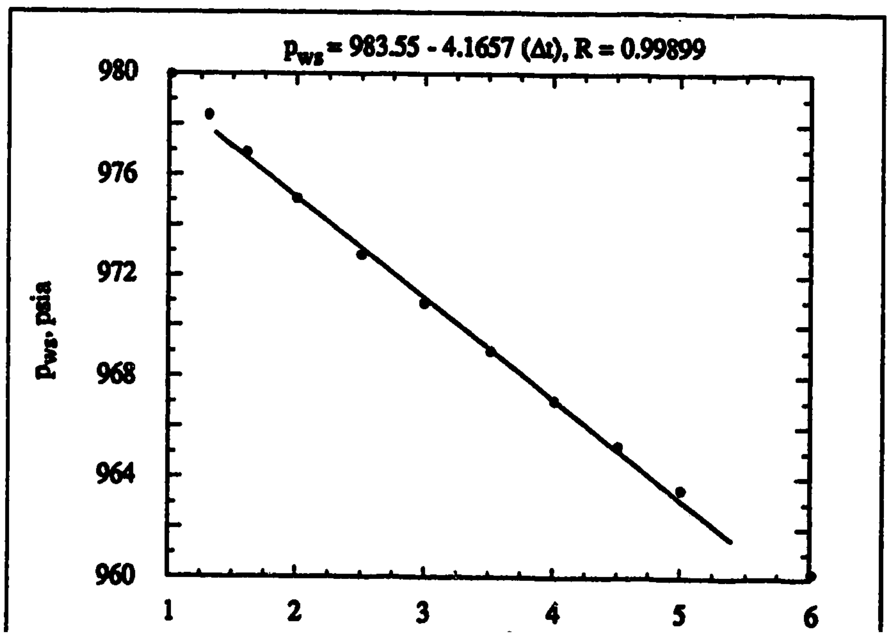

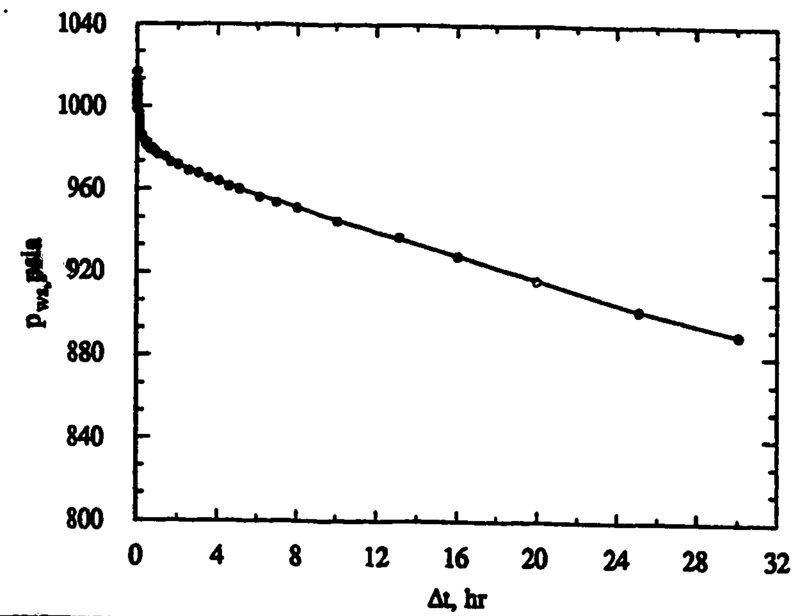

Fig. D.43 - Pressure falloff data for Run 8.

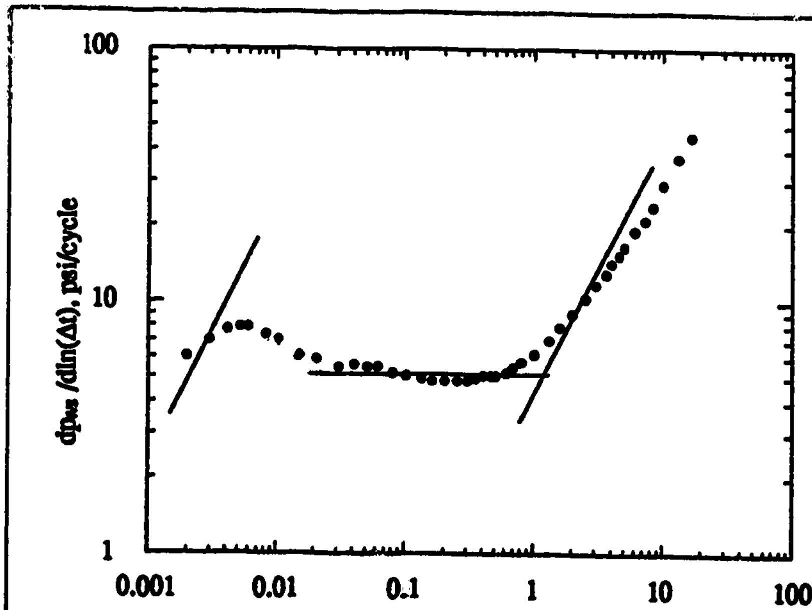

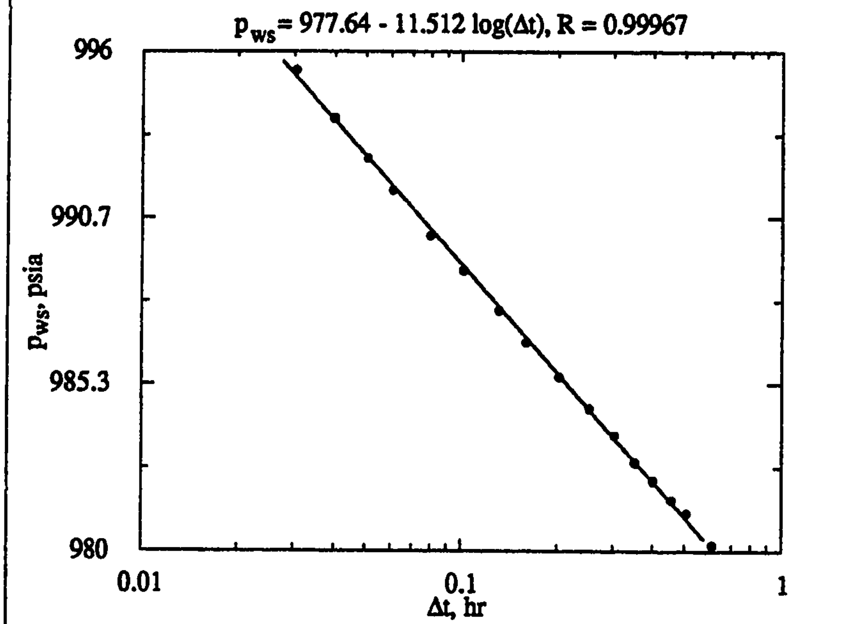

Fig. D.45 - Semilog straight line for Run 8.

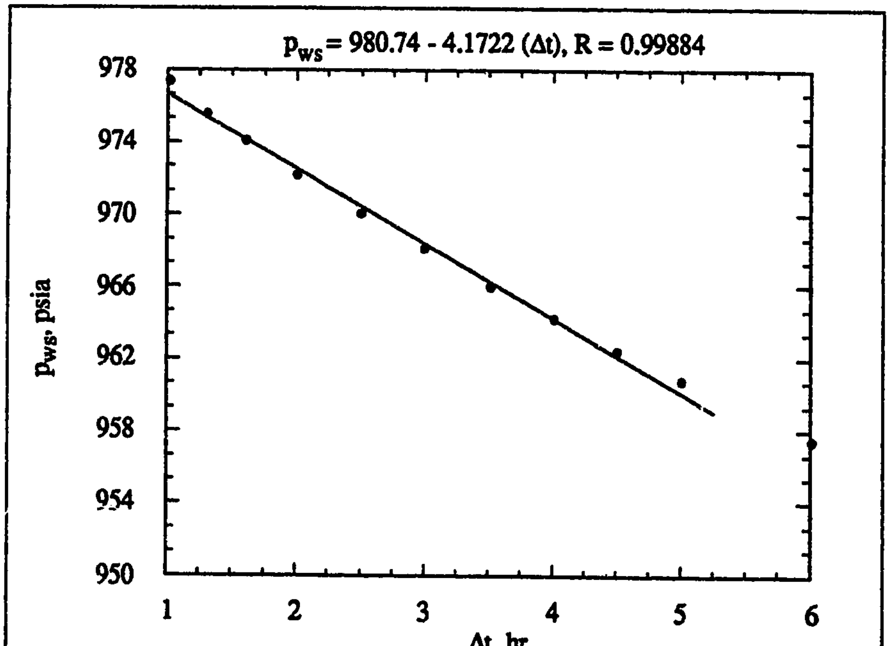

Fig. D.46 - Cartesian straight line for Run 8.

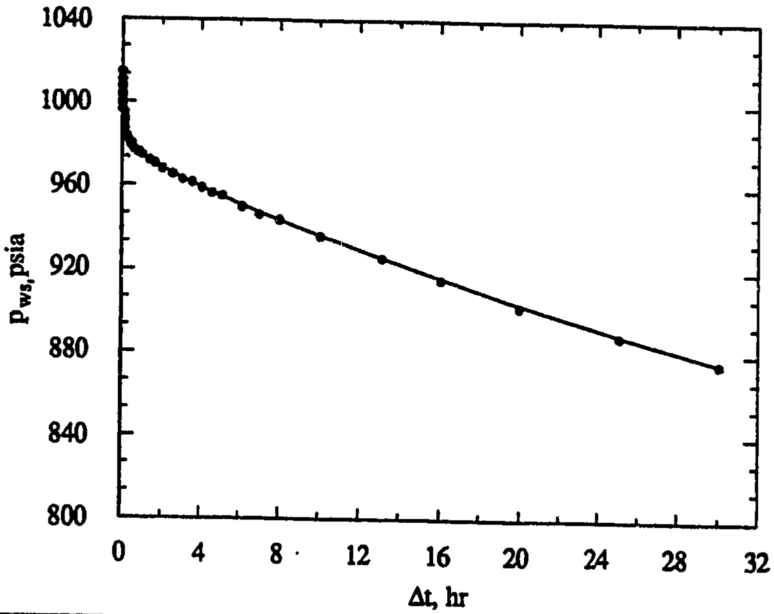

Fig. D.47 - Pressure falloff data for Run 9.

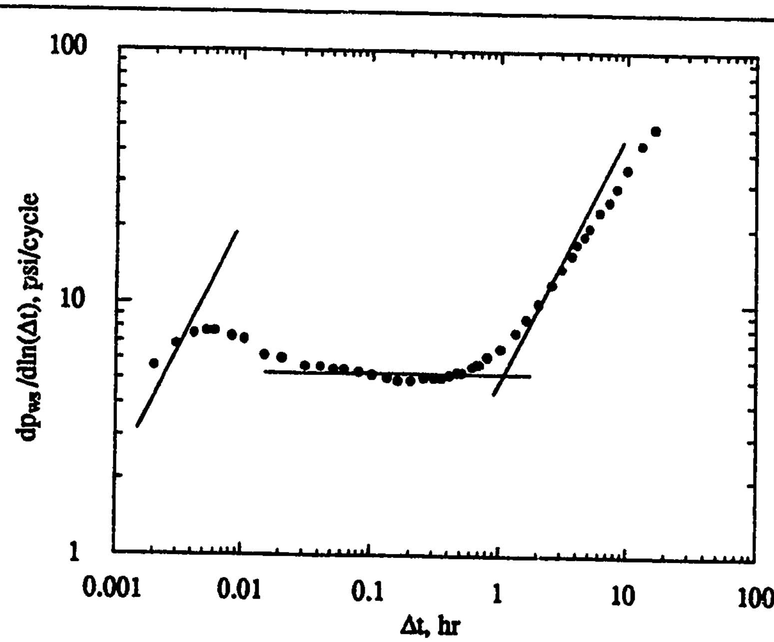

Fig. D.48 - Semilog pressure derivative data for Run 9.

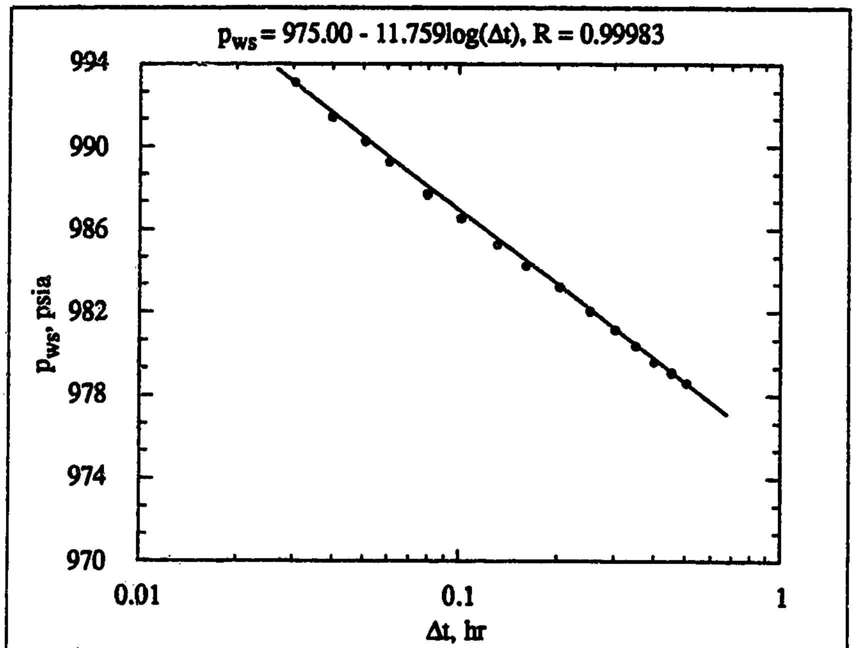

Fig. D.49 - Semilog straight line for Run 9.

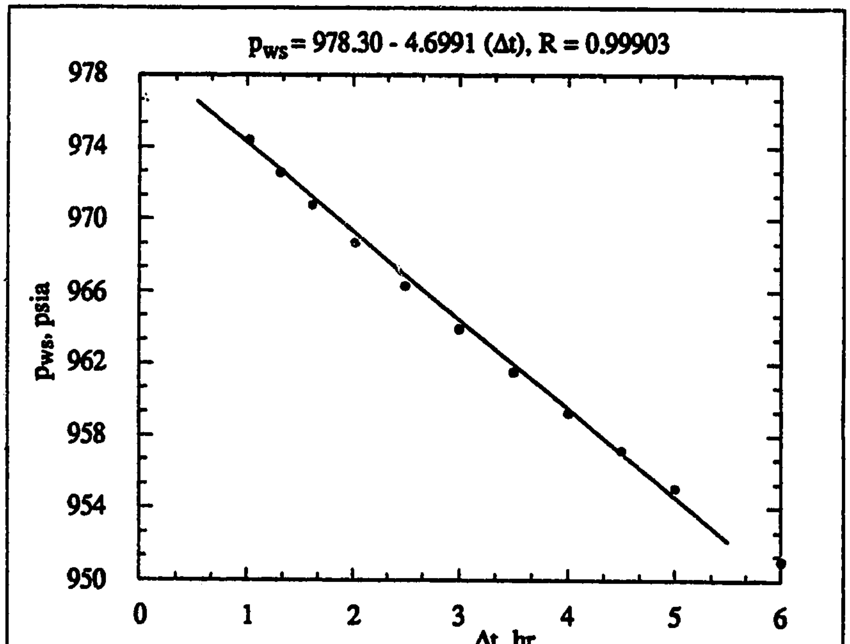

Fig. D.50 - Cartesian straight line for Run 9.

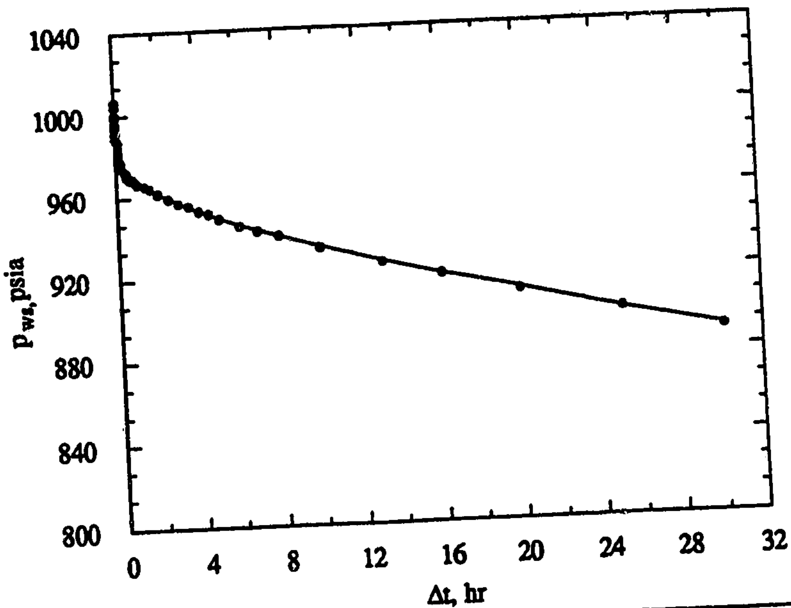

Fig. D.51 - Pressure falloff data for Run 10.

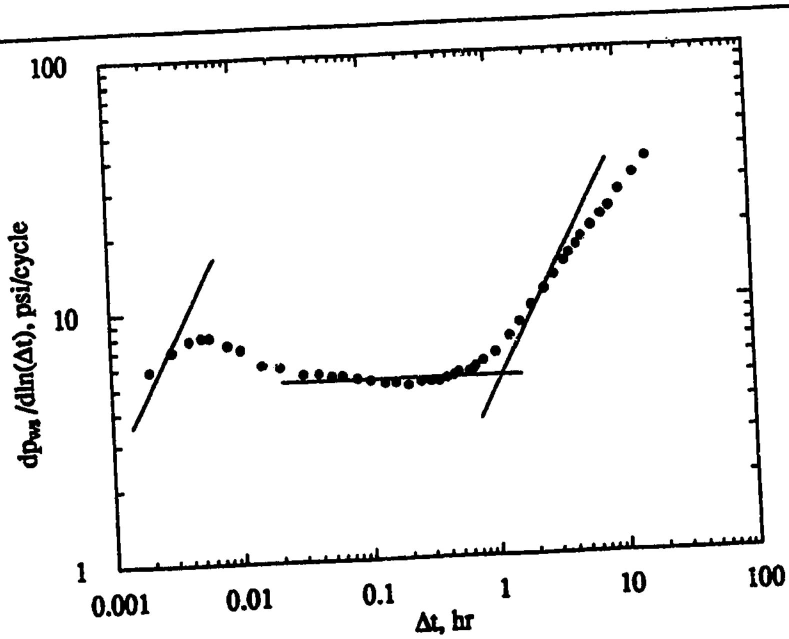

Fig. D.52 - Semilog derivative data for Run 10.

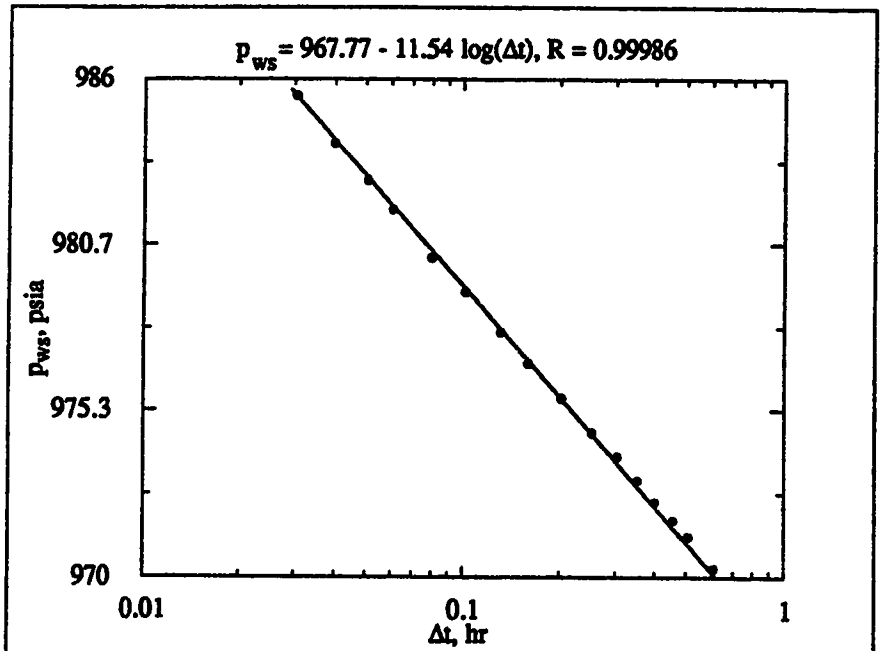

Fig. D.53 - Semilog straight line for Run 10.

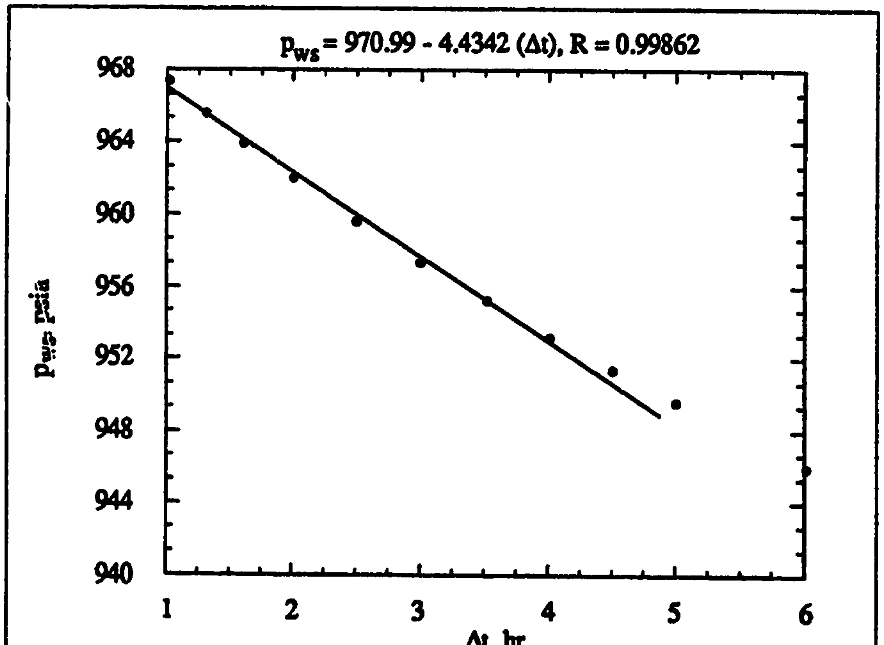

Fig. D.54 - Cartesian straight line for Run 10.

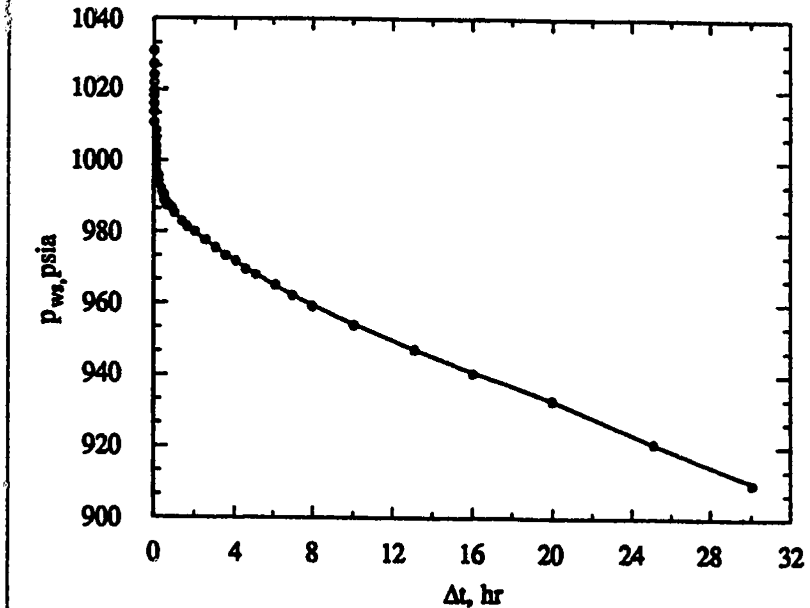

Fig. D.55 - Pressure falloff data for Run 11.

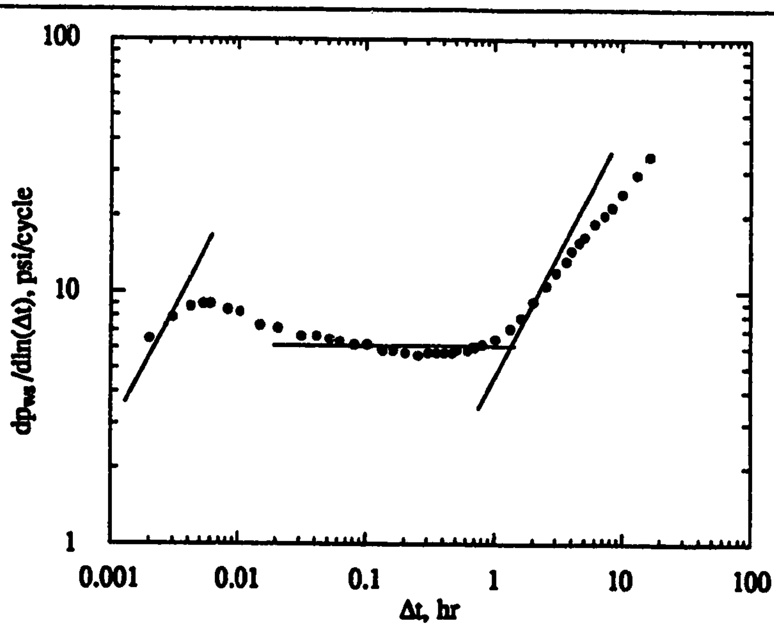

Fig. D.56 - Semilog derivative data for Run 11.

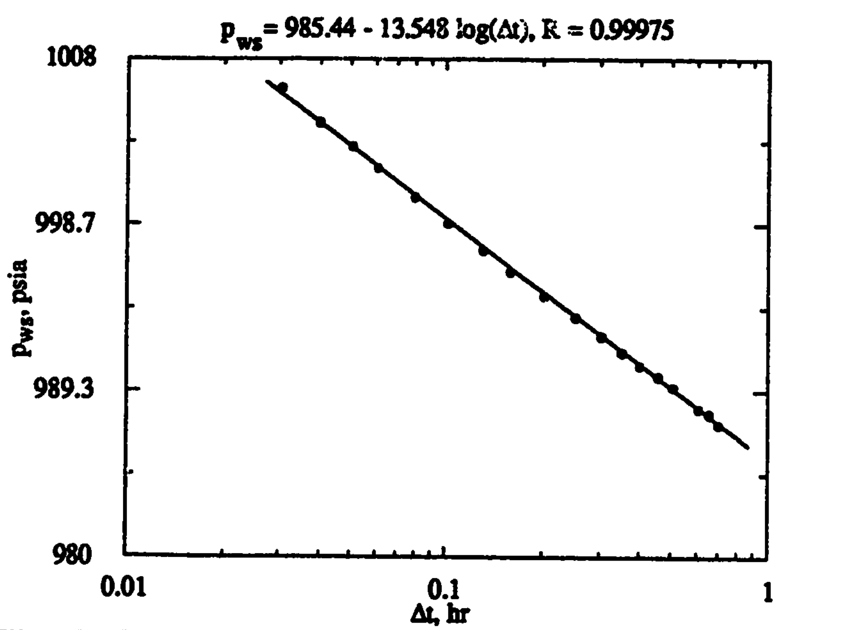

Fig. D.57 - Semilog straight line for Run 11.

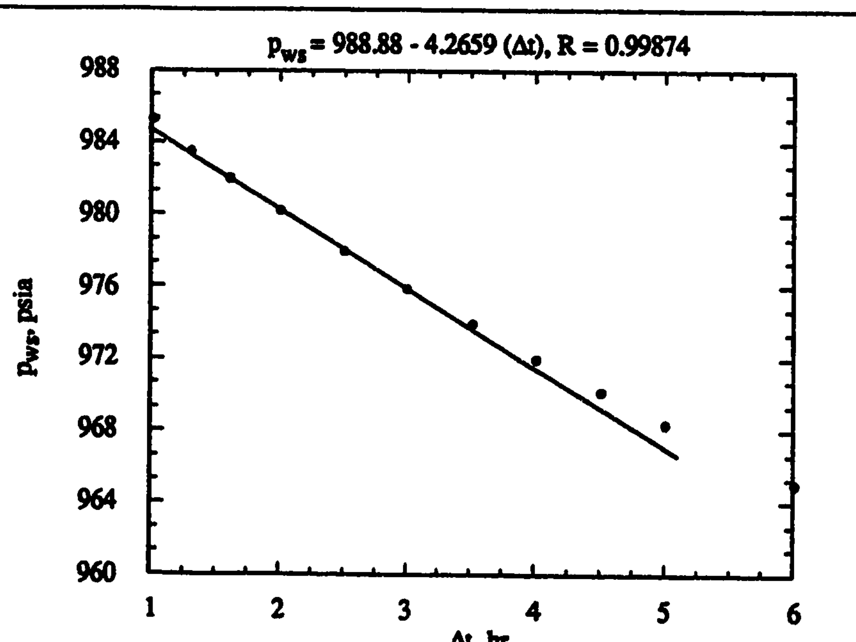

Fig. D.58 - Cartesian straight line for Run 11.

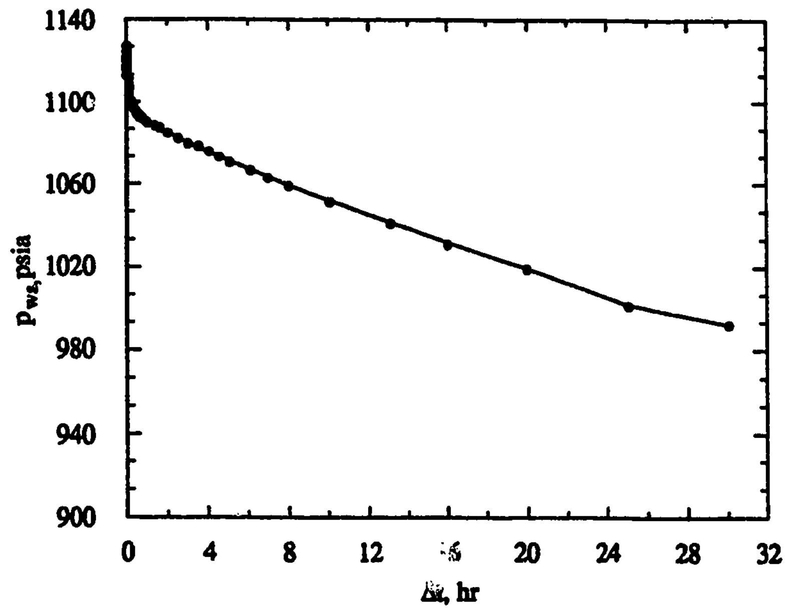

Fig. D.59 - Pressure falloff data for Run 1*.

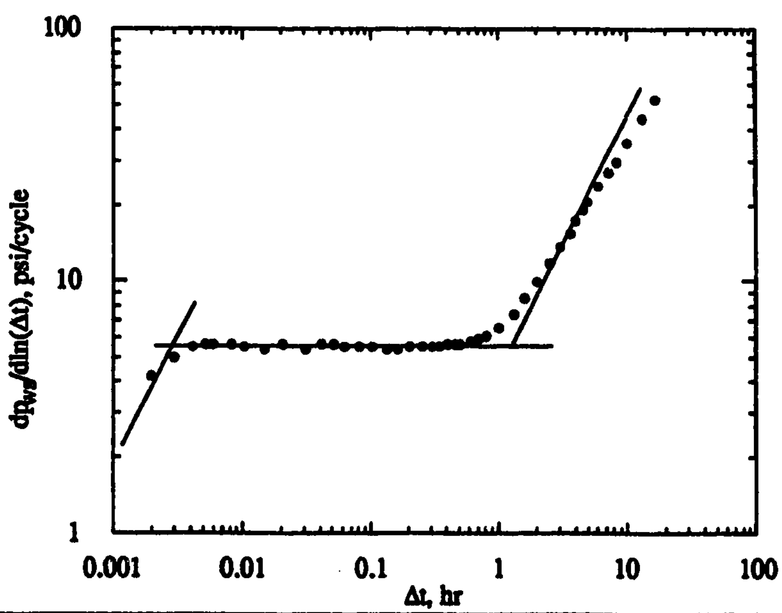

Fig. D.60 - Semilog pressure derivative data for Run 1*.

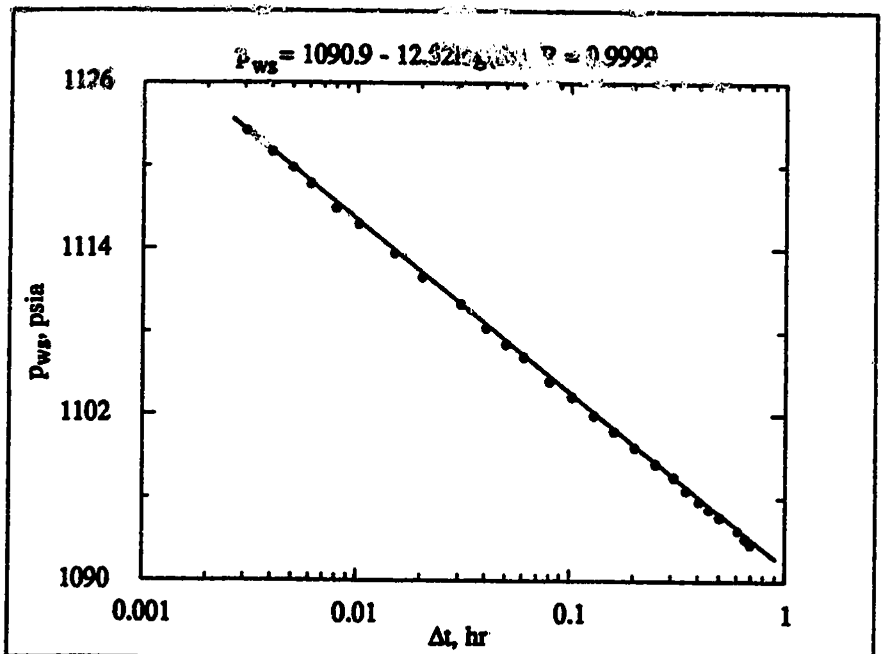

Fig. D.61 - Semilog straight line for Run 1*.

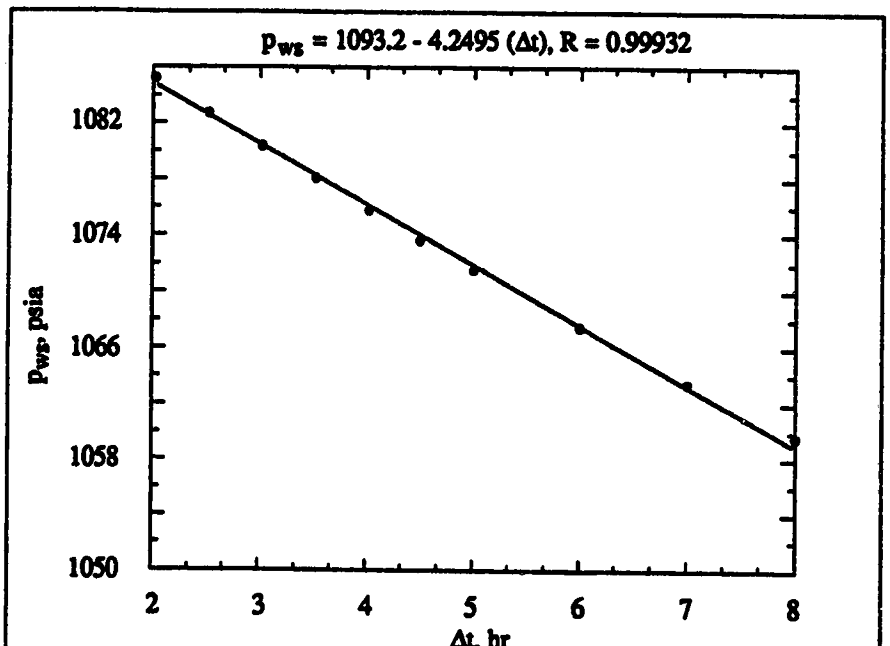

Fig. D.62 - Cartesian straight line for Run 1*.

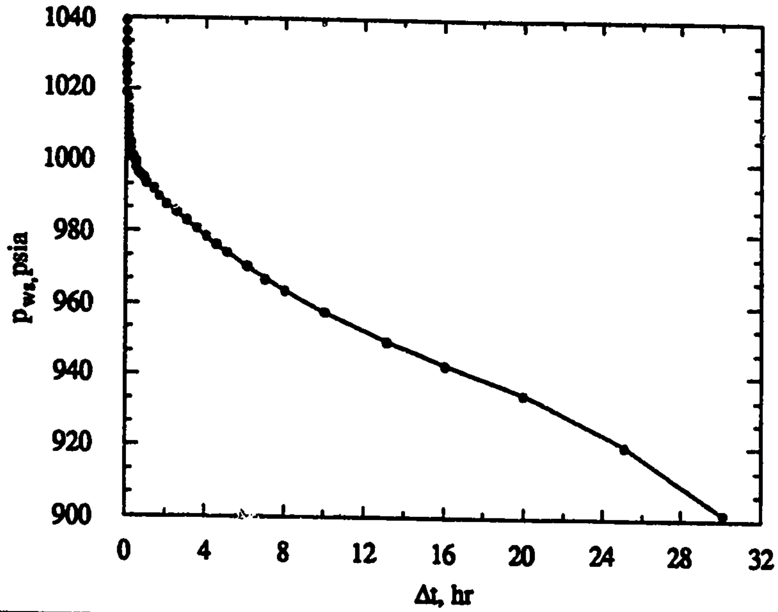

Fig. D.63 - Pressure falloff data for Run 2*.

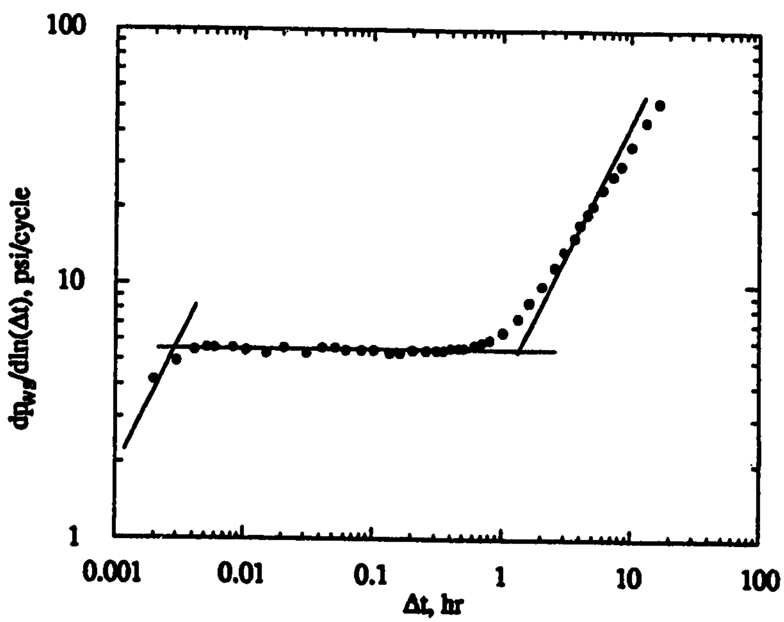

Fig. D.64 - Semilog pressure derivative data for Run 2*.

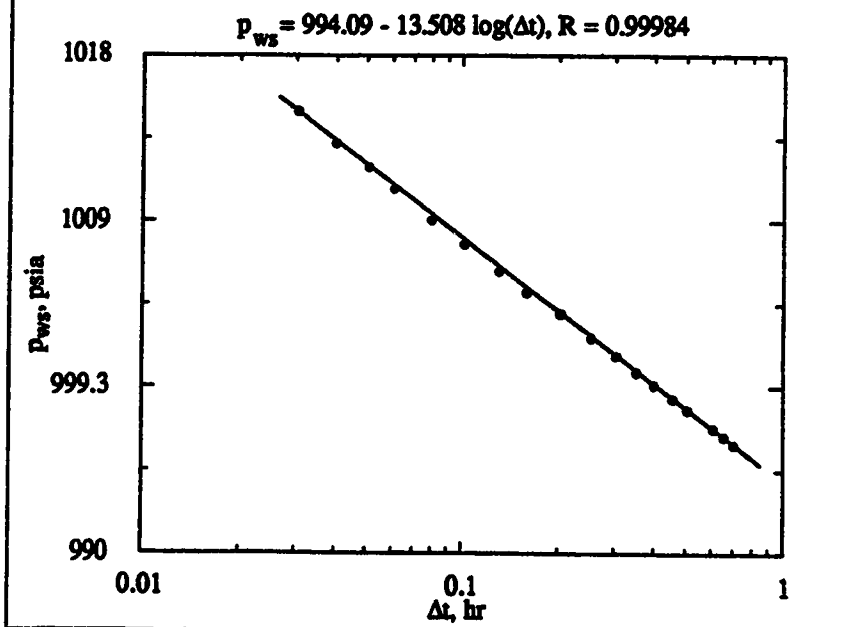

Fig. D.65 - Semilog straight line for Run 2*.

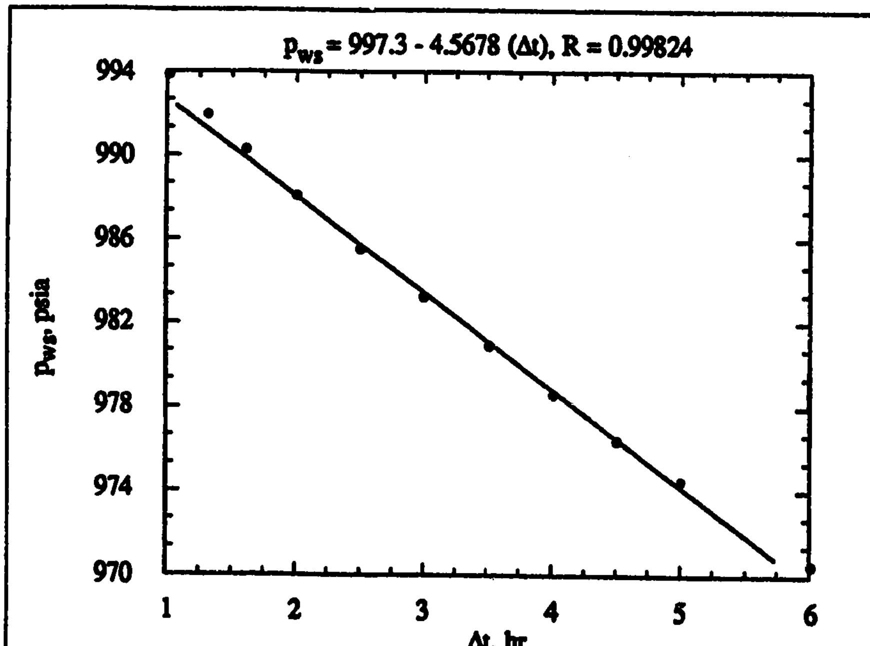

Fig. D.66 - Cartesian straight line for Run 2*.

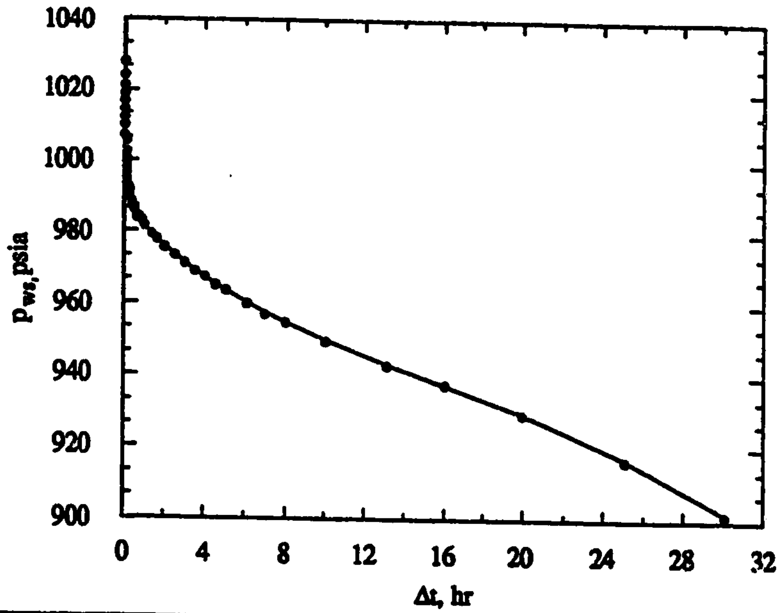

Fig. D.67 - Pressure falloff data for Run 3*.

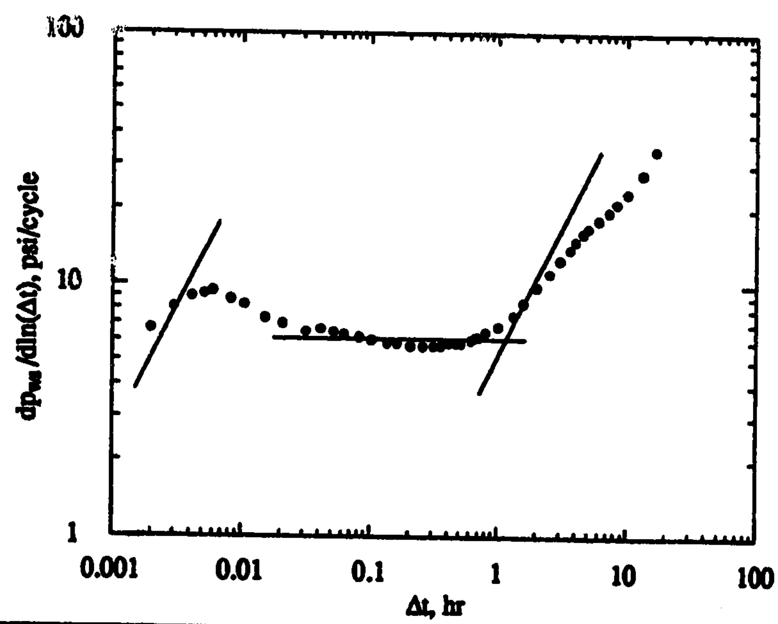

Fig. D.68 - Semilog derivative data for Run 3*.

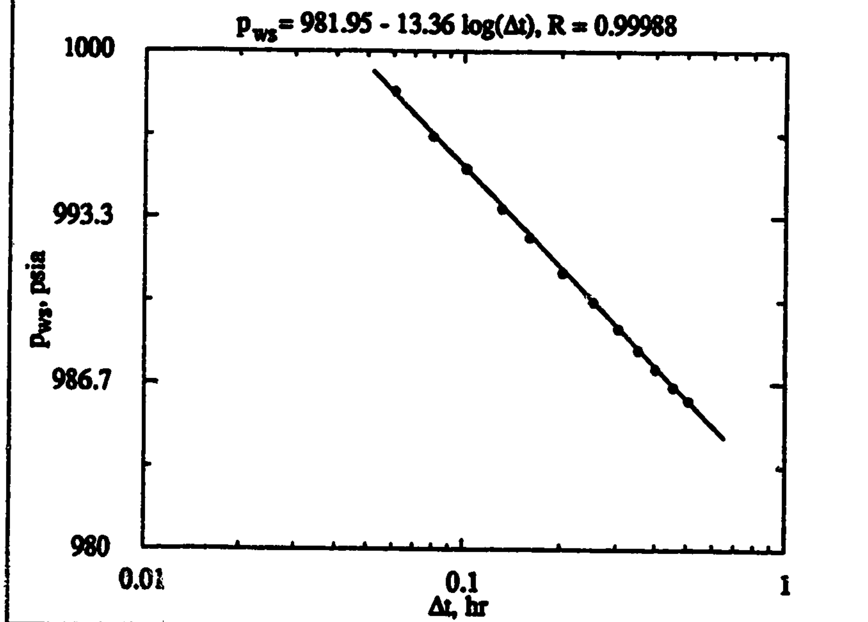

Fig. D.69 - Semilog straight line for Run 3*.

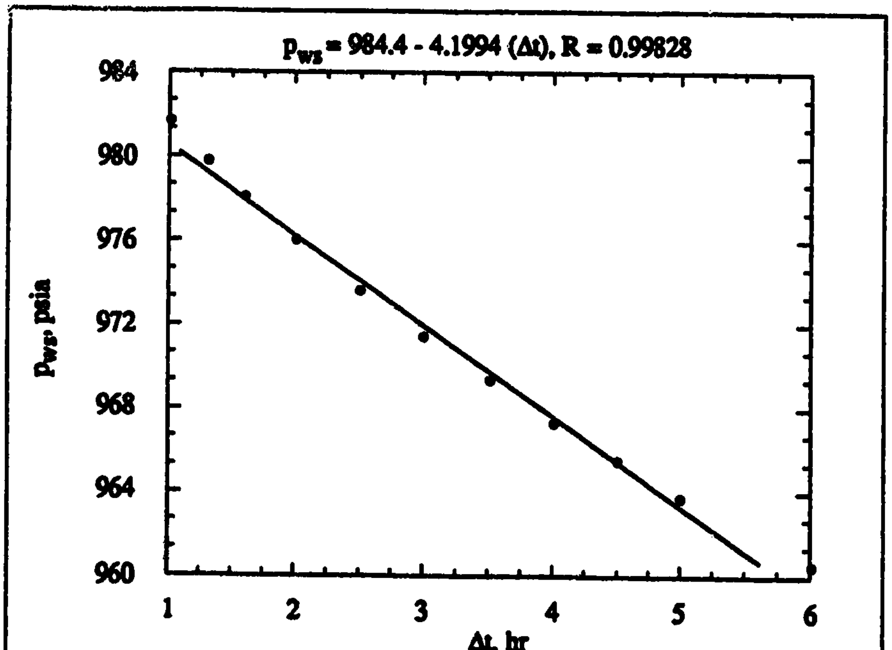

Fig. D.70 - Cartesian straight line for Run 3*.

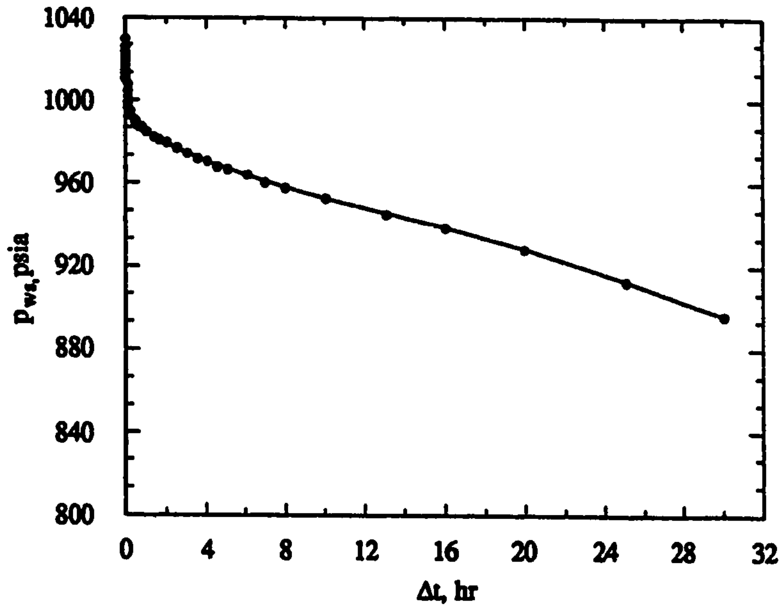

Fig. D.71 - Pressure falloff data for Run 6*.

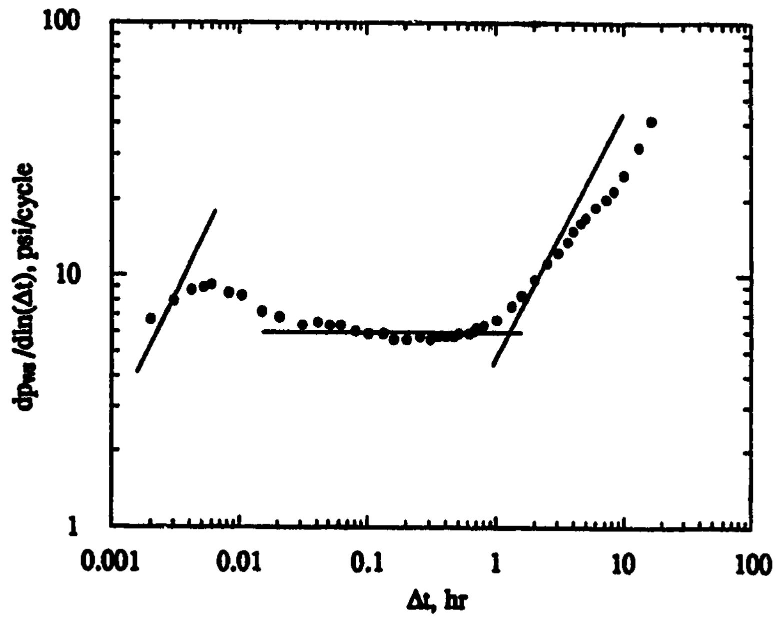

Fig. D.72 - Semilog derivative data for Run 6*.

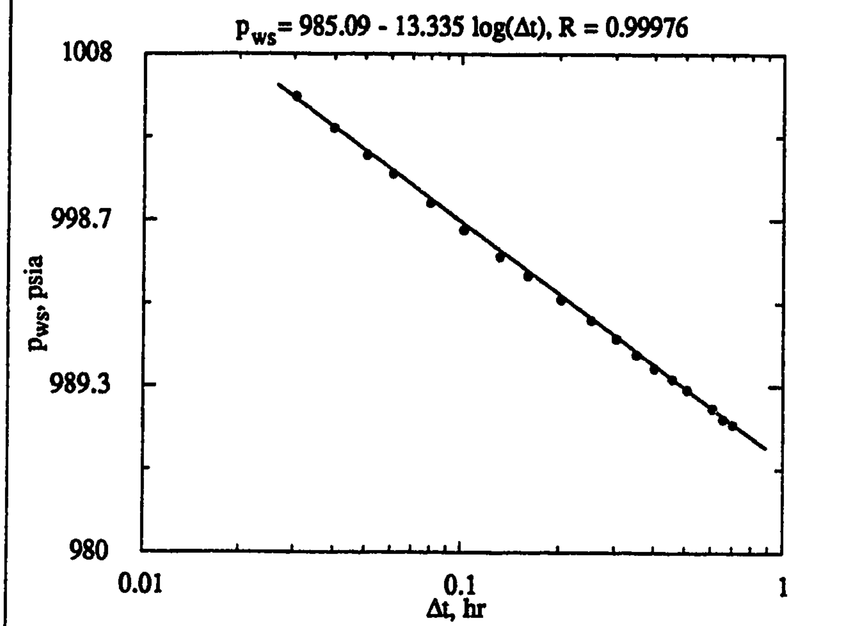

Fig. D.73 - Semilog straight line for Run 6*.

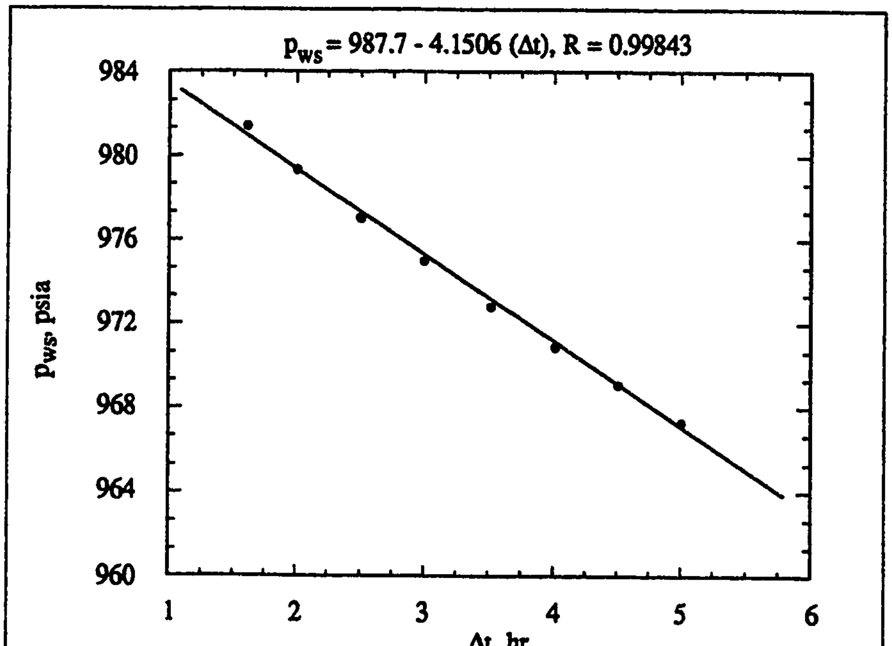

Fig. D.74 - Cartesian straight line for Run 6*.

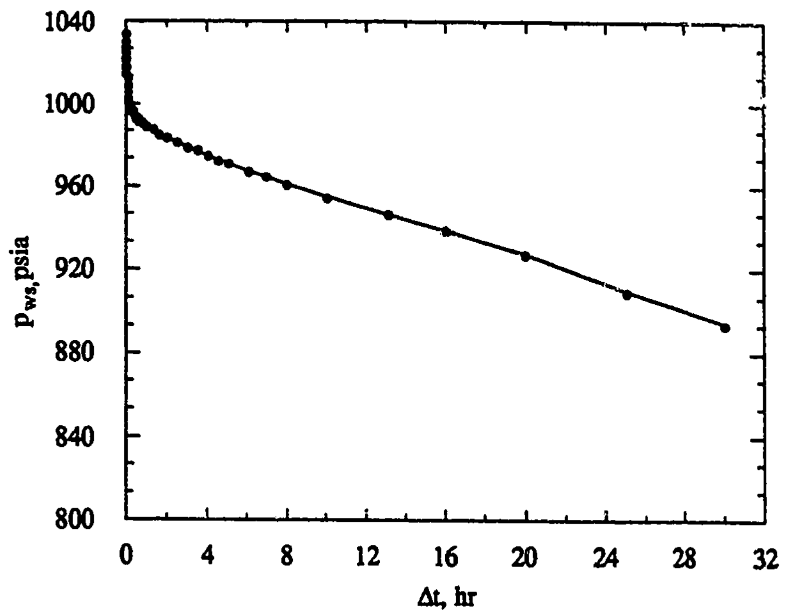

Fig. D.75 - Pressure falloff data for Run 7*.

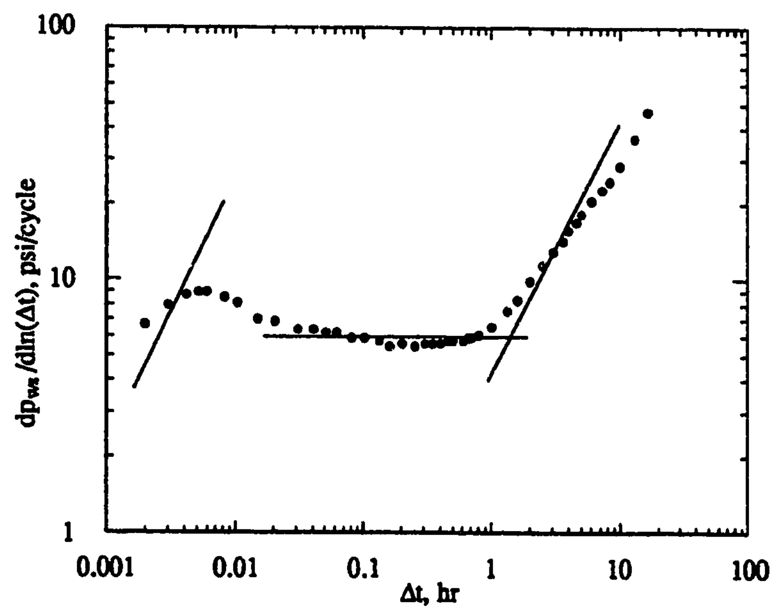

Fig. D.76 - Semilog derivative data for Run 7*.

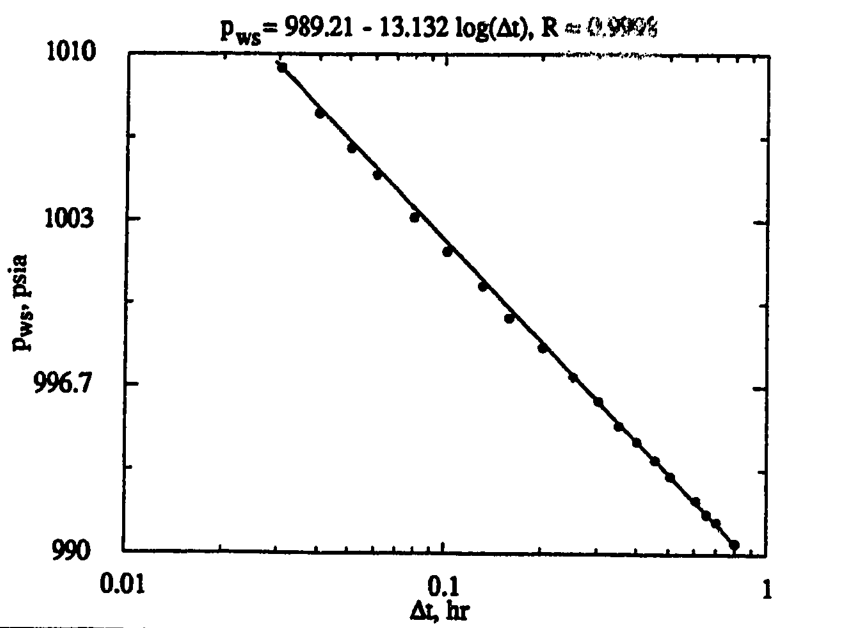

Fig. D.77 - Semilog straight line for Run 7*.

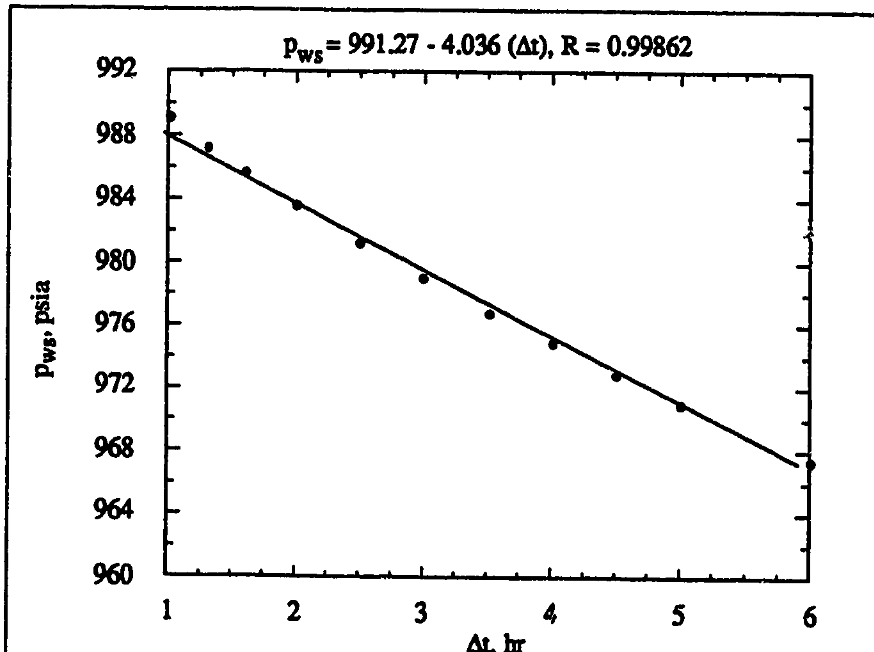

Fig. D.78 - Cartesian straight line for Run 7*.

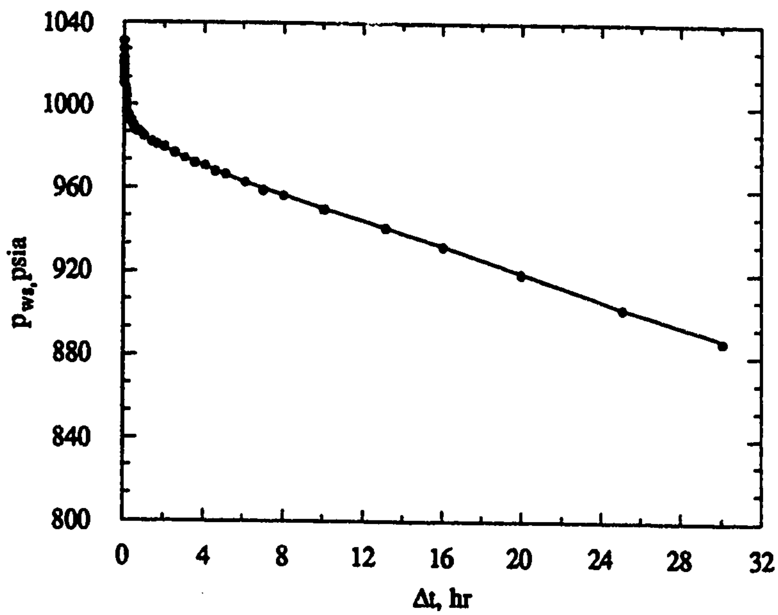

Fig. D.79 - Pressure falloff data for Run 8*.

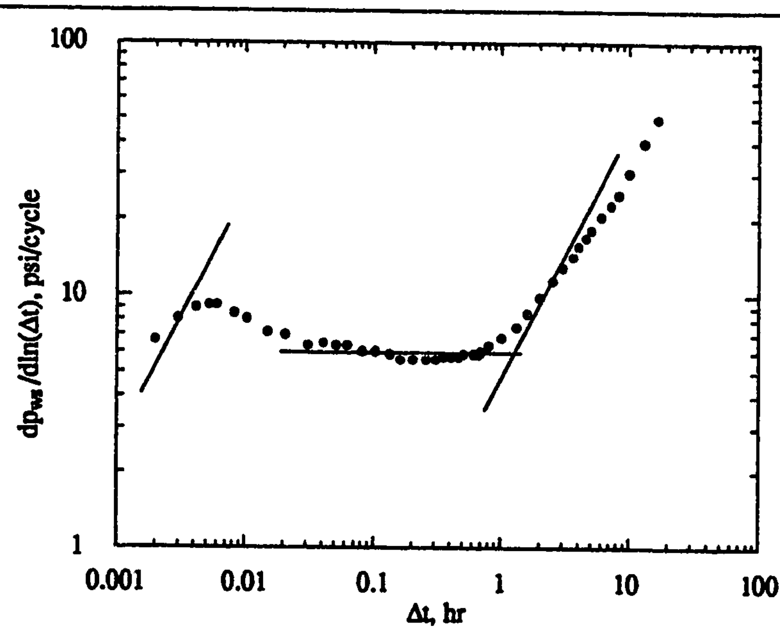

Fig. D.80 - Semilog derivative data for Run 8*.

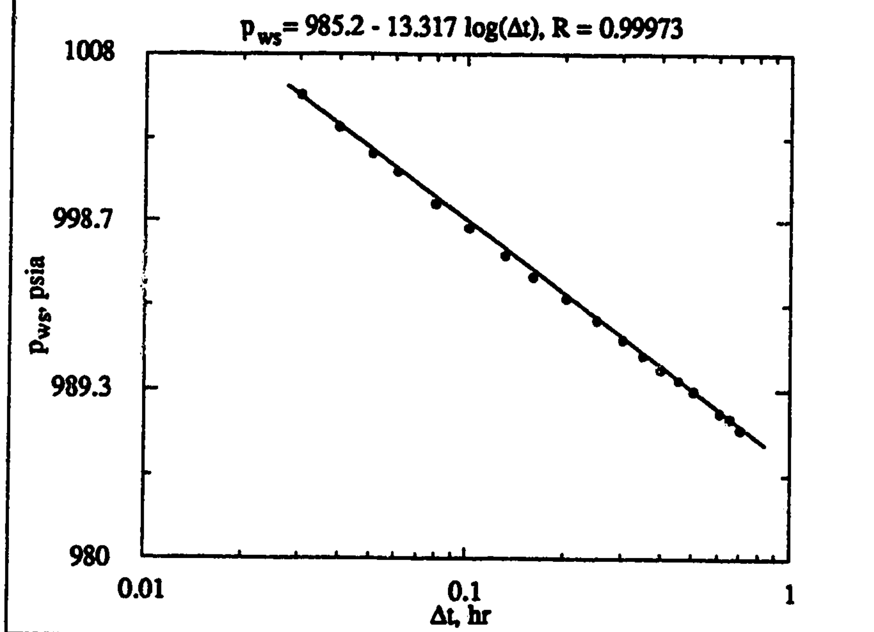

Fig. D.81 - Semilog straight line for Run 8*.

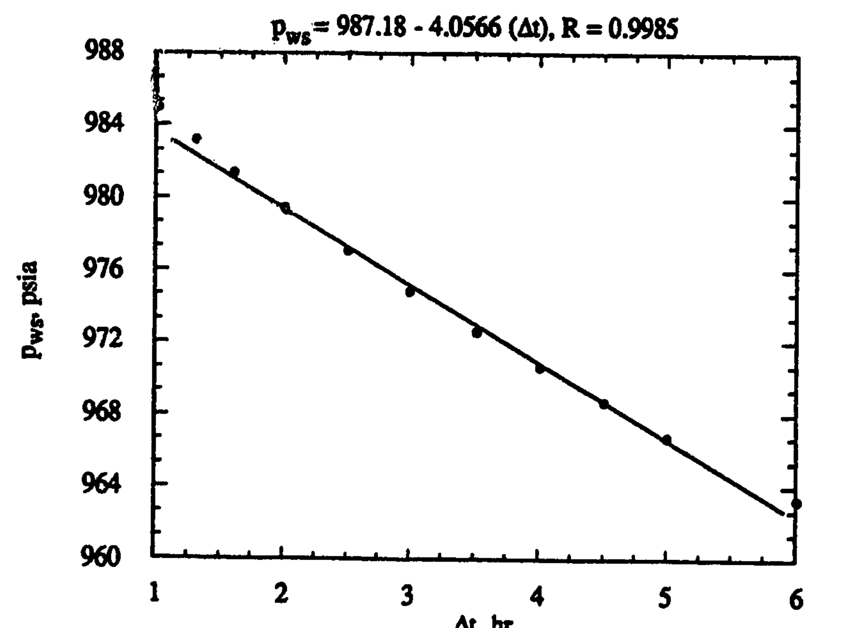

Fig. D.82 - Cartesian straight line for Run 8*.

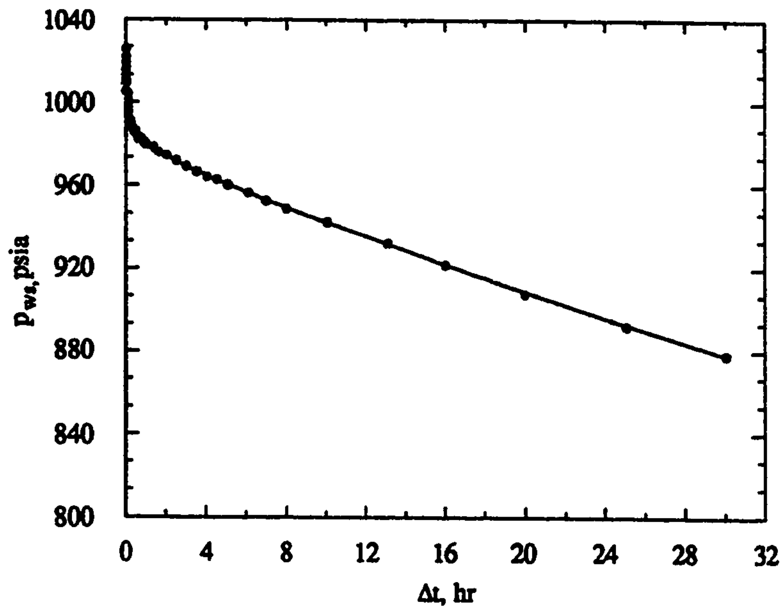

Fig. D.83 - Pressure falloff data for Run 9*.

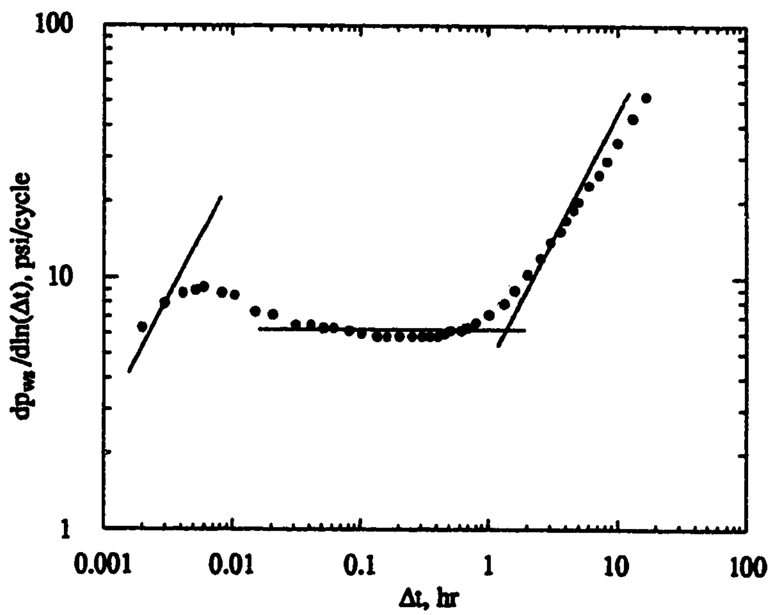

Fig. D.84 - Semilog derivative data for Run 9*.

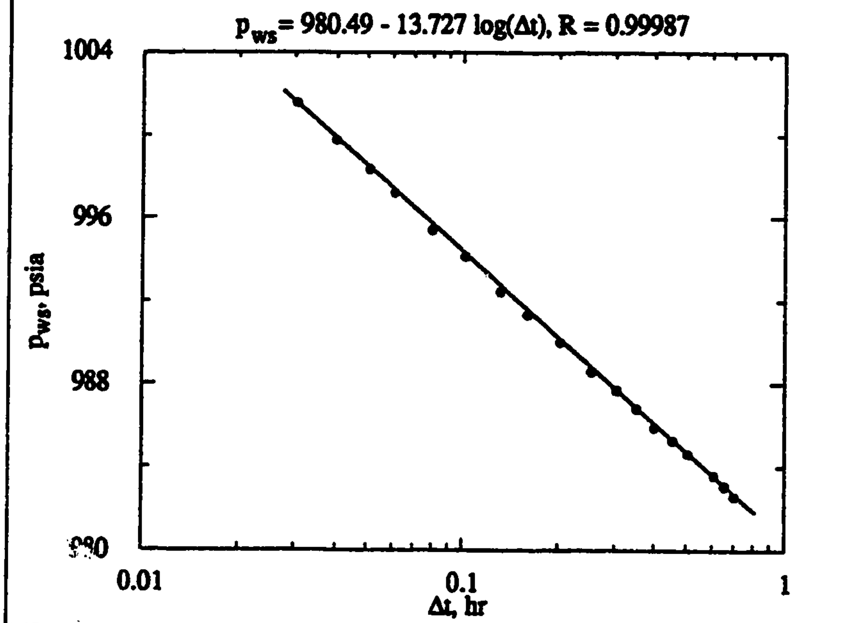

Fig. D.85 - Semilog straight line for Run 9*.

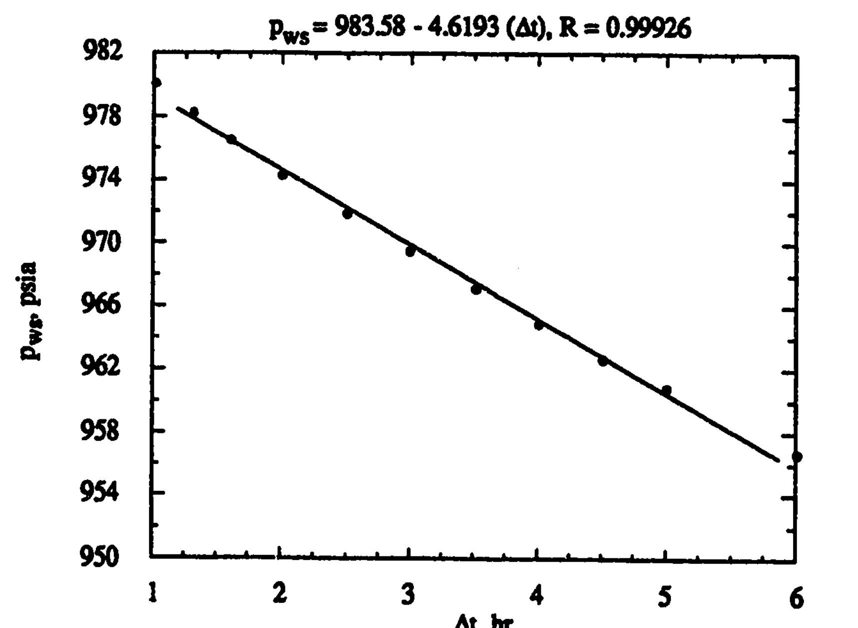

Fig. D.86 - Cartesian straight line for Run 9*.